Master's thesis

NTNU
Norwegian University of Science and Technology
Faculty of Engineering
Department of Civil and Environmental Engineering

David Viejo Mariño

Review of rock stability models, slope stability and rockfall assessment for a section of Vestpynten-Bjorndalen (Svalbard)

Master's thesis in Cold Climate Engineering

Supervisor: Arne Aalberg (UNIS), Knut Vilhelm Hoyland (NTNU) & Ida Lykke Fabricius (DTU)

September 2020

NTNU
Norwegian University of Science and Technology

UNIS
The University Centre in Svalbard

DTU

David Viejo Mariño

Review of rock stability models, slope stability and rockfall assessment for a section of Vestpynten-Bjorndalen (Svalbard)

Master's thesis in Cold Climate Engineering
Supervisor: Arne Aalberg (UNIS), Knut Vilhelm Hoyland (NTNU) & Ida Lykke Fabricius (DTU)
September 2020

Norwegian University of Science and Technology
Faculty of Engineering
Department of Civil and Environmental Engineering

NTNU
Norwegian University of
Science and Technology

Acknowledgments

I want to thank all my supervisors and reviewers for their feedback which helped into making this thesis better.

Arne Aalberg my main supervisor for all the help, the projects and trips we did together my stay in Svalbard and my thesis would not have been the same.

Nataly Marchenko for her time and help to obtain the most important digital terrain model and 3D shapes of the rocks, could not have done it without you.

Amir M Kaynia and Steve Gibbons from NGI for their help with seismic data

Jean-Dominique from RocPro 3D and the RAMMS team for providing me with licenses for their software

Last but not least all the friends I did up here and moments spent together being them in the wild, at Nybyen or Sjøskrenten. Because sleeping outside at 21° in the arctic is uncommon, a mirror will never be just a mirror and well… just SEND IT.

Abstract

Geotechnical hazards represent a threat to communities around the world. The area between Vestpynten and Bjørndalen in the artic archipelago of Svalbard presents several geotechnical hazards that had produced recent incidents related with avalanches, debris flow and rockfalls. This area is used by the local population with leisure purposes. Due to that and the risk associated, a risk assessment report was commissioned by the local authorities.

The focus of this project is to describe the different methods used to analyse the behaviour of rockfalls on a slope and its stability taking into account different environmental conditions both present and future. To later apply those to a concrete section of the Vestpynten- Bjørndalen and analyse its stability and the consequence of a rockfall event.

To perform that the section geology was studied to obtain data on the rock characteristics, fractures, strike and dip values and a digital terrain model of the area was produced with a laser scanner. Dangerous rock outcrops were selected and modelled in 2D and their stability analysed employing the SSR method.

Subsequently rockfalls on the same area were simulated to obtain their trajectories, velocity and energy. Two different programs with different approaches to the simulation were employed for this purpose.

The results show a stable slope for present and regular conditions meanwhile different degrees of instability are achieved for future conditions and seismic events.

Regarding rockfalls, under different scenarios the trajectories represent a real threat to the cabins present in the area.

Table of contents

Table of figures

1. Introduction

1.1. The Svalbard archipelago

Svalbard or Spitsbergen is an archipelago located in the arctic region between 74° to 81° N and 10° to 35° E whose sovereignty relies on the kingdom of Norway, see Figure 1

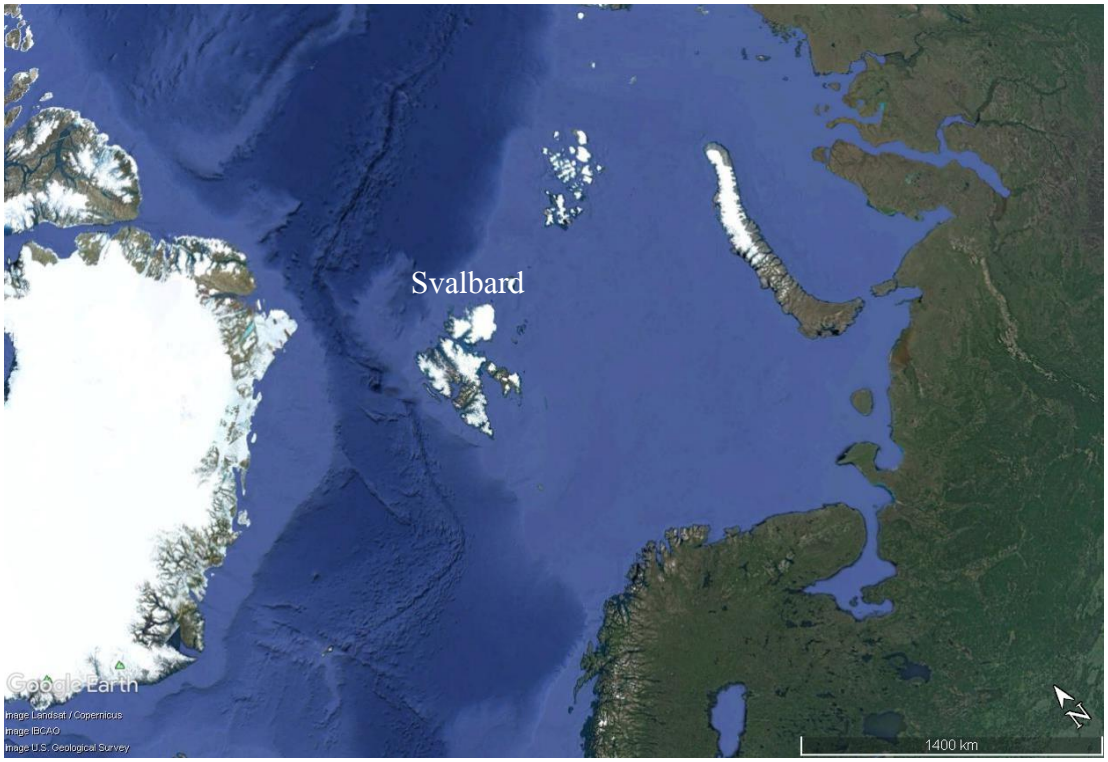

Figure 1 General location of the Svalbard archipelago in the arctic region

Svalbard presents three main settlements as shown in Figure 2, Longyearbyen the biggest one and point of entrance to the island with a population around 2500, Barentsburg a Russian settlement with around 600 inhabitants and Ny-Alesund a research town.

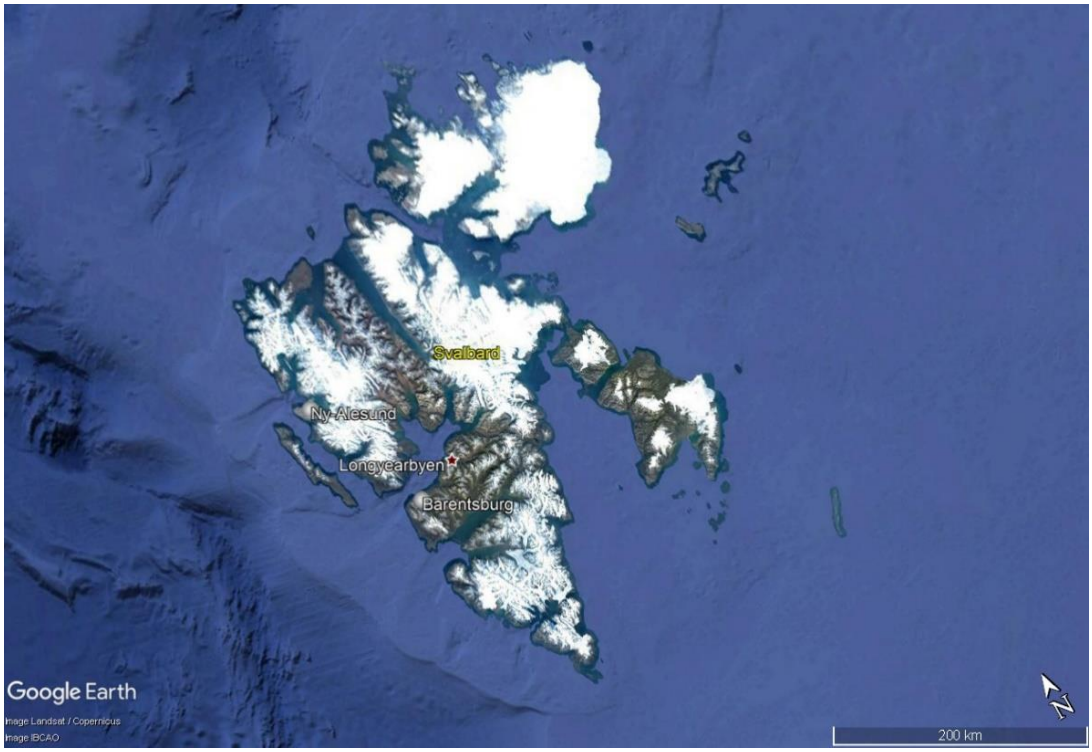

Figure 2 The Svalbard archipelago (Google Earth)

Due to its location, the archipelago's weather is of arctic nature which is a type of extreme weather characterised by extremely low temperatures, high winds, and periods of complete darkness or daylight (polar night and midnight sun respectively). At the same time on a more global scale its situation means that it is under the influence of the polar amplification effect which accelerates and increases the global warming mechanisms.

Figure 3 shows historical and future predictions for the temperature in Longyearbyen based on different CO_2 emission scenarios, extracted from (Norsk Klimaservicesenter, Meteorologisk institutt, 2019)

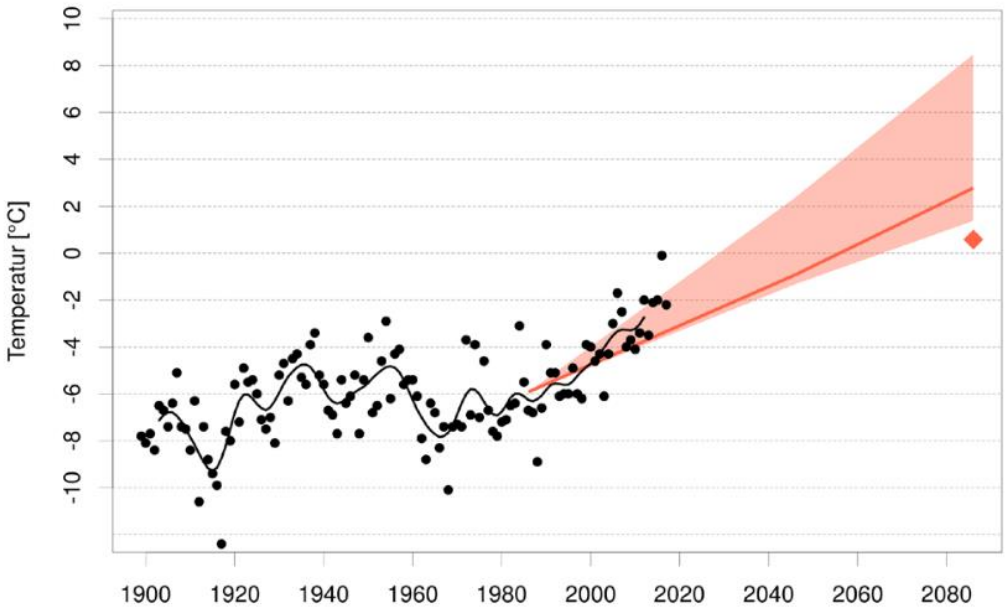

Figure 3 Average annual temperature for Svalbard airport. Dot is single year and black curve is smoothed variation on a ten-year scale based on observations from 1900 to 2017. The red section shows predictions for future climate scenarios shown with red line (median) and diamond (fine-scale model) shaded area shows interval between high and low emissions scenario from (Norsk Klimaservicesenter, Meteorologisk institutt, 2019)

This project takes place around the Longyearbyen area precisely at a section between Vestpynten and Bjørndalen, along the road that connects Longyearbyen with Bjørndalen, see Figure 4.

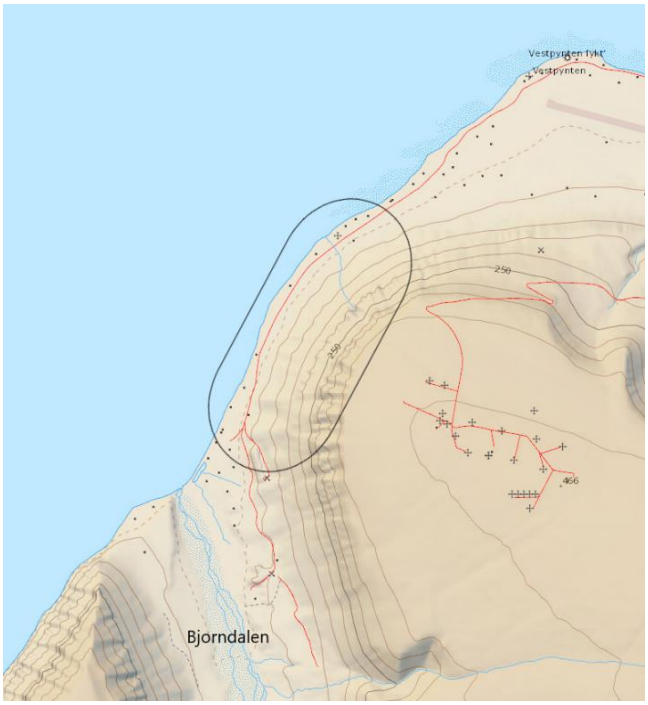

Figure 4 Location of with the project has taken place from TopoSvalbard modified by (Viejo)

This area presents steep hillsides, rock outcrops and cliffs seen in Figure 5 which represent a geotechnical hazard.

Figure 5 Aspect of the top of the slope around the study zone (Viejo)

The slope angle on the study zone presents a minimum value of 25 º with a max value of 90 º for the cliff areas and a mean of 65º. For the type of geology in the area, sandstone and shales, slope angles higher than 45º present a probable release area.

At the same time it shows clear sings of mass movements along the years like boulders, debris fans and channels from landslides / debris flow, see Figure 6. This type of deposits had been identified and mapped by the NGU (Norges Geologiske Undersøkelse/Norwegian Geological Survey) in (Rubensdotter, 2015) and the extract corresponding to the study area is shown in

Figure 6 On the left a boulder found on the area (Viejo), on the right a landslide/debris flow channel (Multiconsult, 2017)

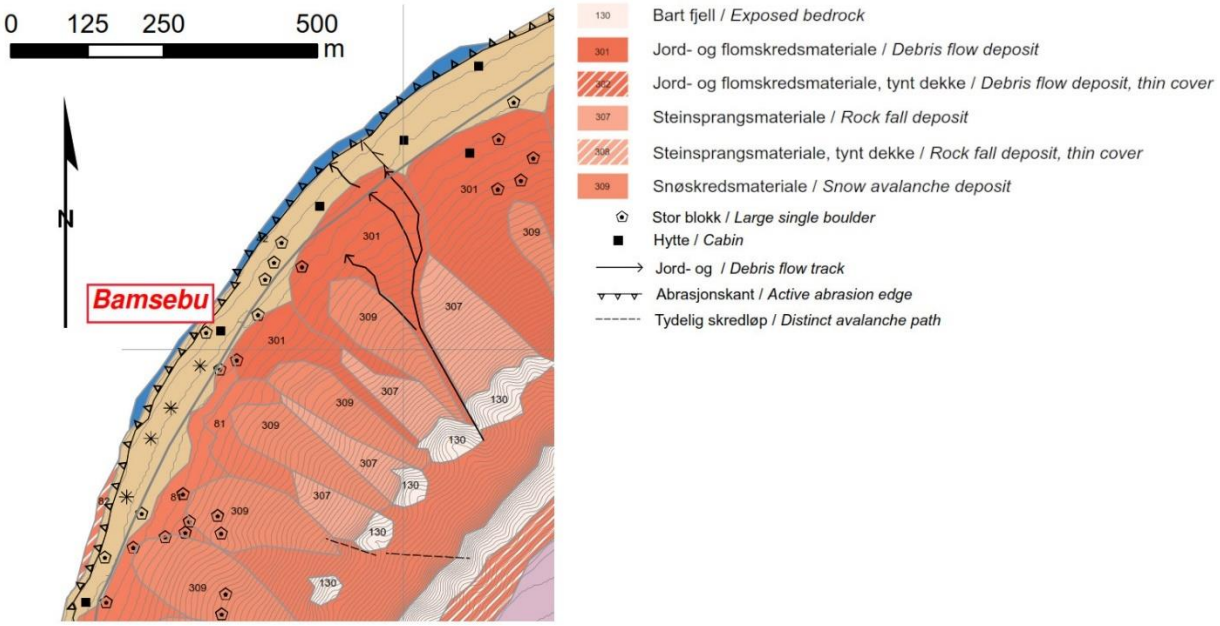

Figure 7 Extract from (Rubensdotter, 2015) about the type of surface materials and their origin on the study area of the project

1.2. Previous study

All this section of the coastline is used by the local residents as a leisure place with a lot of cabins present, which, due to the hazards located on the area promoted, the local authorities were interested on its assessment

A study was carried out on behalf of Longyearbyen Lokalstyre by the company Multiconsult (Multiconsult, 2017)

That report covered all of the gravitational processes, but only its findings for rockfalls covering the Vestpynten to Bjørndalen part of the report (the area that is equivalent to the one in this study) are summarized here:

- The entire stretch up to the entrance towards Bjørndalen is characterized by the danger of rockfall. Exposed rock shows a large degree of cracking, see Figure 8 extracted from (Multiconsult, 2017)

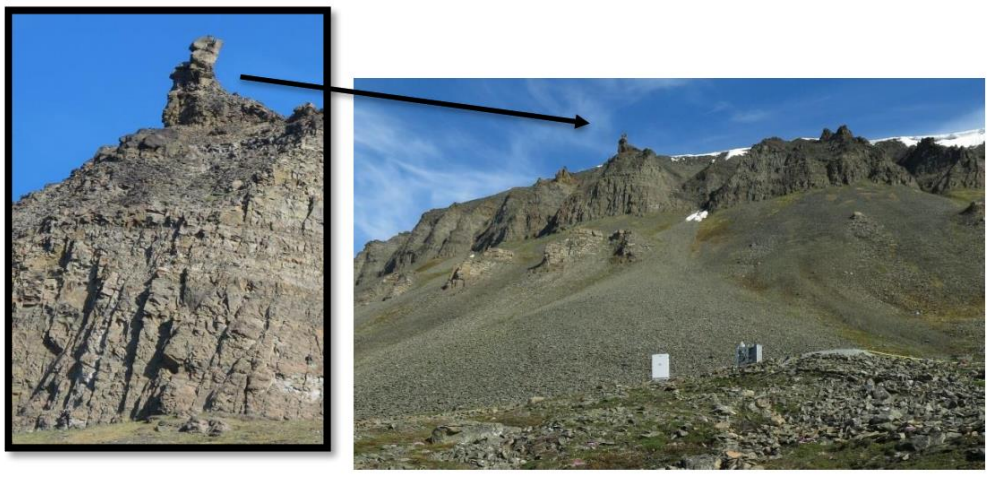

Figure 8 Photo showing the degree of cracking extracted from (Multiconsult, 2017)

- In some areas there have been landslides with outlet across the road and down to the shore
- Figure 9 shows the risk map developed by Multiconsult in the (Multiconsult, 2017) report, red shows 1/100 year, orange 1/1000 and yellow 1/5000 type of events areas of influence

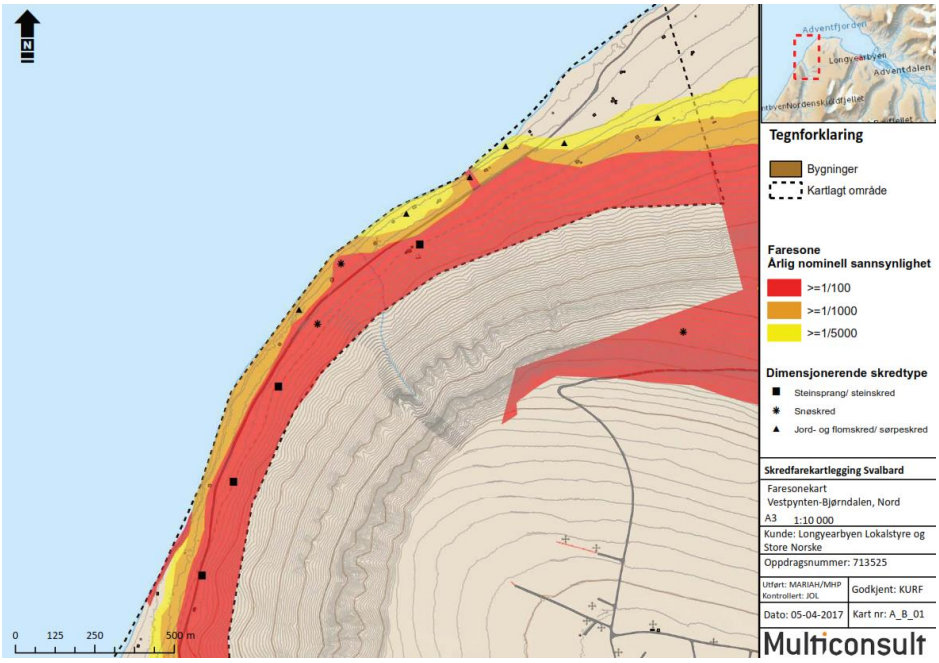

Figure 9 Risk map from (Multiconsult, 2017) for the area of interest

- Figure 10 Shows the results of the simulations conducted by Multiconsult regarding avalanches and rockfalls

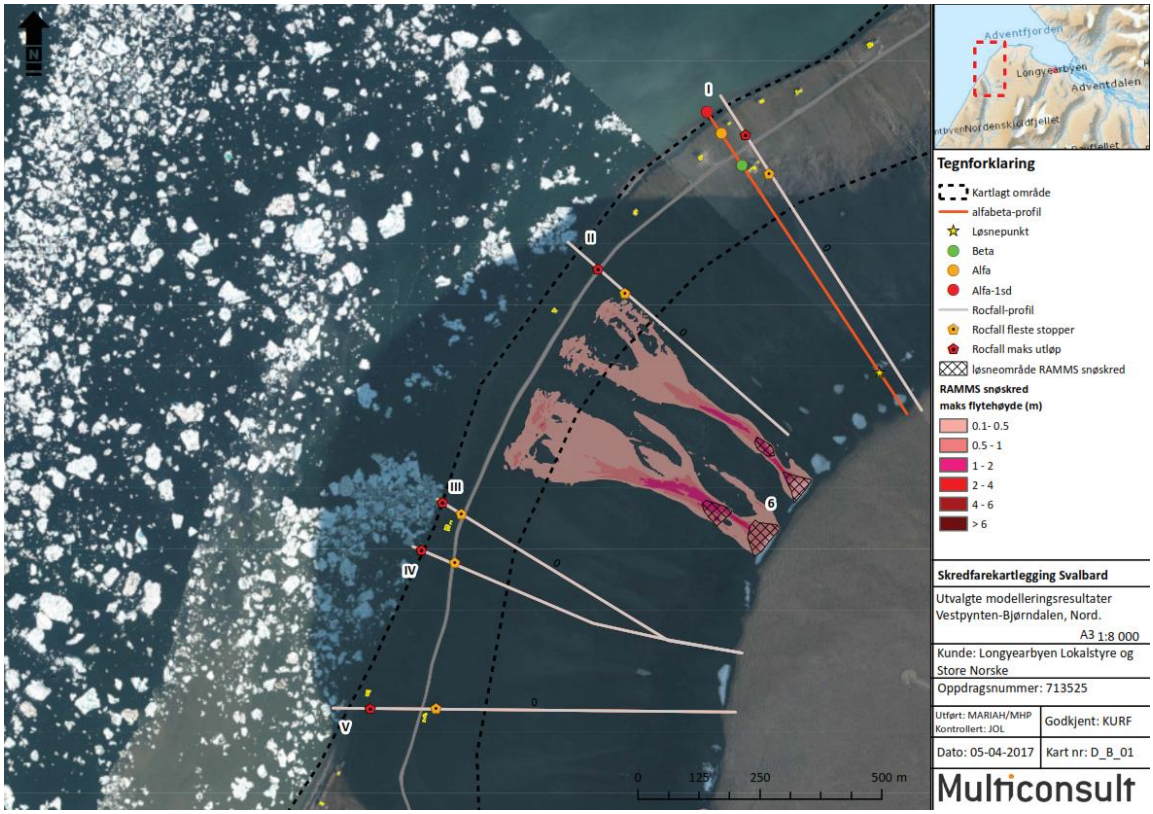

Figure 10 Map showing the results of rockfall and avalanche events with runout areas for the avalanche in shadows of pink and stopping points for rockfalls in orange with red signalling maximum extent (Multiconsult, 2017)

From the results of (Multiconsult, 2017) it can be seen that the area presents real risk for the owners of the properties built in place. Despite this the events can be categorized under low probability, as the risk map shows that most of the cabins lay into the 1/1000 years type of event classification.

The report explains future scenarios with warmer conditions and their consequences on the different processes that were assessed on it but is not clear if the obtained risk maps show this condition on the assigned risk value.

1.3. Objective

This master thesis project aims to provide an analysis of the section between Vestpynten and Bjørndalen not only from the rockfall risk point of view but also incorporating an analysis of the stability of that area. While knowing the previous study done in the area and its results.

This will be done by running computer simulations with actual environmental conditions and future warmer environments which could increment the frequency, severity of such events, diminish some and empower others or alter the behaviour of them.

1.4. Rock mass classification systems and strength criteria

When working with rock masses or blocks it is necessary to stablish its mechanical properties which will determine how risk assessment is done and infrastructures built.

This section introduces the main rock mass classification systems and how their parameters are used on the different strength criteria. There are three main classifications used right now, Rock Mass Rating (RMR) from Bieniawski (1973,1976, 1989), Barton's Q (Barton, Lien, Lunde (1974)) and a modification of the RMR called GSI developed by Hoeck and Brown (1988)

1.4.1. Rock Mass Rating (RMR) Bieniawski (19733, 1976, 1989)

The RMR is comprised of six parameters:

1) Compression strength: obtained from tables or from samples tested in a lab
2) RQD: Rock Quality Designation, a measure of the hardness of a rock mass which is inferred from the integrity of a core run when extracted from the borehole. The value is obtained with the following expression:

$$RQD = \frac{\sum core\ fragments \geq 10cm}{length\ of\ the\ core\ run} * 100$$

If no core runs are available RQD can be obtained from rock outcrops with the expression:

$$RQD = 110 - 2.5J_v$$

Where J_v is the number of joints per cubic metre

3) Joint spacing: distance between the discontinuity planes, depending to this distance the rock mass has a different designation according to Table 1

Table 1 Deere's classification of joint spacing (1967)

Description	Joint spacing	Type of rock mass
Really wide	>3 m	Solid
Wide	1-3 m	Massive
Moderately closed	0.3-1 m	Blocky
Closed	0.05-0.3 m	Fractured
Really closed	<0.05 m	Crushed

4) Nature of the joints: the joints themselves are described using the following parameters, the values that describe each parameter can be found in
    1) Aperture between joint edges
    2) Dimensions of the joint following trend and plunge
    3) Roughness of the joint edges
    4) Strength of the rock at the joint edges
    5) Joint filling
5) Presence of water
6) Orientation of the discontinuities

With the first five parameters of the classification and following Table 2 the primary or initial value for the rock mass is obtained. This value is further on adjusted with parameter 6 according to Table 3

Figure 11 is a representation of a rock block with the most important parameters used for geomechanical classifications.

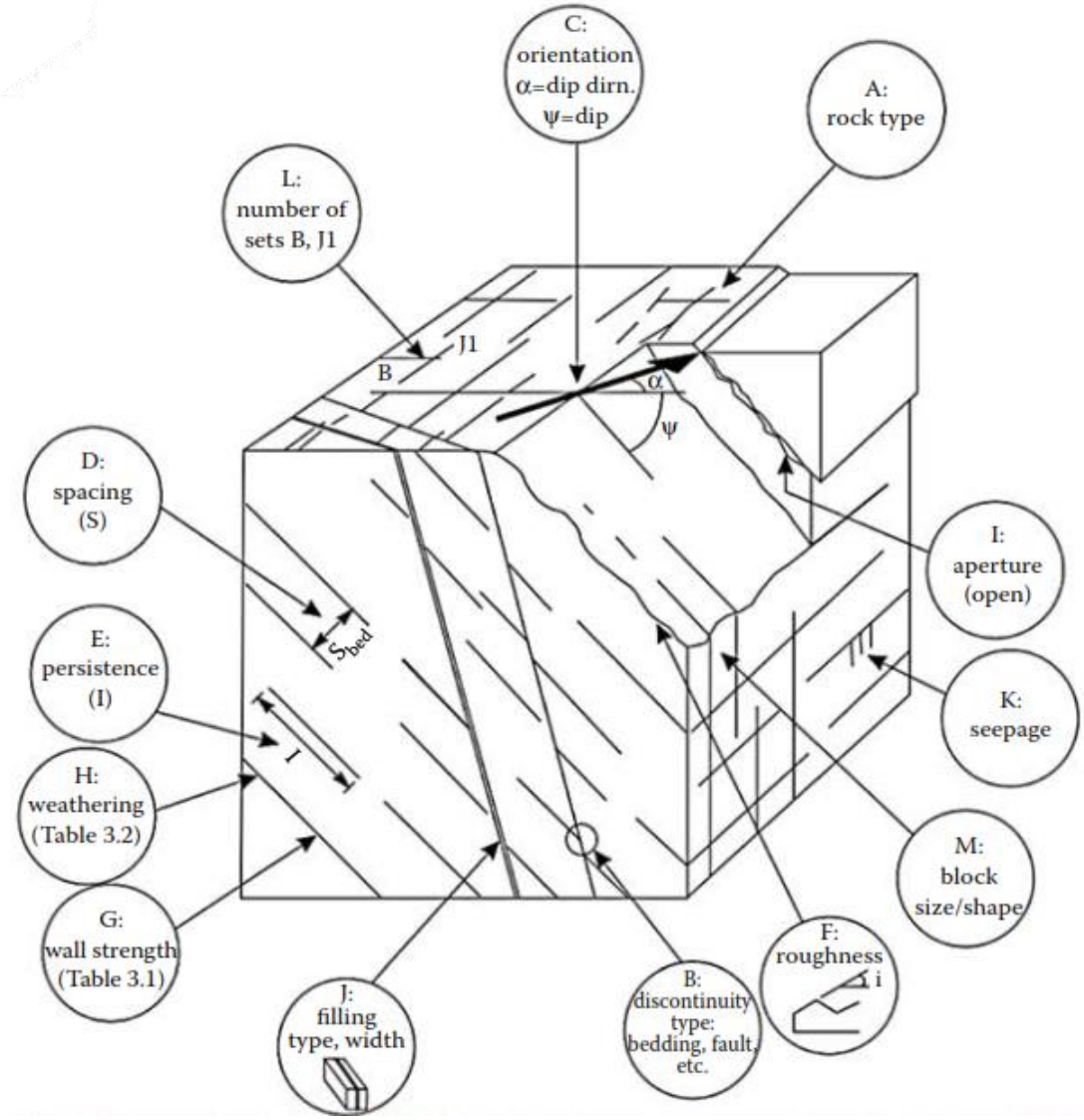

Figure 11 Parameters to describe a rock mass from (Duncan, 2018)

The last adjustment is done with Table 4 using the denomination obtained from parameter 6. The RMR is the result of adding each value together. Table 5 presents the denomination for the rock mass according to its RMR interval.

Table 2 RMR parameters classification translated from (Oyanguren & Monge, 2004)

Parameters		Scale							
1	Strength of undisturbed rock	Point load	>10 MPa	4-10 MPa	2-4 MPa	1-2 MPa	For these values simple compression is recommended		
		Simple compression	>250 MPa	100-250 MPa	50-100 MPa	25-50 MPa	5-25 MPa	1-5 MPa	<1 MPa
	Value		15	12	7	4	2	1	0
2	RQD		90-100 %	75-90 %	50-75 %	25-50 %	<25 %		
	Value		20	17	13	8	3		
3	Joint spacing		>2 m	0.6-2 m	0.2-0.6 m	0.06-0.2 m	<0.06 m		
	Value		20	15	10	8	5		
4	Joint condition		Very rough, not continuous, closed, rock healthy at the edges	Slightly rough, <1 mm separation, slightly weathered rock at the edges	Slightly rough, <1 mm separation, very weathered rock at the edges	Mirror, fault, or joint filling <5 mm thick or open joints 1-5mm, continuous joints	Soft filling with thickness >5 mm or open joints >5 mm continuous joints		
	Value		30	25	20	10	0		
5	Water	Water flow per 10 m of tunnel	None	<10 l/min	10-25 l/min	25-125 l/min	>125 l/min		
		Ratio between water pressure in the joint/maximum main stress σ_1	0	<0.1	0.1-0.2	0.2-0.5	>0.5		
		General conditions	Completely dry	Moist stains	Moisty	Water drops	Water flow		
		Value	15	10	7	4	0		

Table 3 Relative orientation between cavity axis and joints from (Oyanguren & Monge, 2004)

Trend perpendicular to tunnel axis				Trend parallel to tunnel axis		Dip 0-20 º (Independent of trend)
Direction towards dip		Direction against dip				
Dip 45-90 º	Dip 20-45 º	Dip 45-90 º	Dip 20-45 º	Dip 45-90 º	Dip 20-45 º	
Very favourable	Favourable	Regular	Unfavourable	Very unfavourable	Regular	Unfavourable

Table 4 RMR adjustment due to joint orientation from (Oyanguren & Monge, 2004)

Direction of discontinuities trend and plunge		Very favourable	Favourable	Regular	Unfavourable	Very unfavourable
Values	Tunnels and mines	0	-2	-5	-10	-12
	Foundations	0	-2	-7	-15	-25
	Slopes	0	-5	-25	-50	-60

Table 5 Rock mass classes under RMR criteria translated from (Oyanguren & Monge, 2004)

RMR value	81-100	61-80	41-60	21-40	<20
Number class	I	II	III	IV	V
Description	Very good	Good	Regular	Bad	Very bad

1.4.2. Q classification system (Barton et al 1974)

As in a similar way than RMR the Q index relies in 6 parameters:

- RQD
- J_n: number of groups of joints
- J_r: joint roughness
- J_a: joint weathering

  } These two parameters are influenced by joint filling
- J_w: decreasing factor accounting for water presence
- SRF: stress reduction factor, it depends on the actual tensional state of the rock mass

The Q value of the rock mass is obtained by using each parameter on equation 1

$$Q = \frac{\frac{RQD}{J_n} * J_r}{\frac{J_a}{SRF} * J_w} \quad 1$$

The parameters have a range between the values in Table 6

Table 6 ranges for Q parameters from (Oyanguren & Monge, 2004)

RQD	0-100
J_n	0.5-20
J_r	0.5-4
J_a	0.75-20
J_w	0.05-1
SRF	0.5-20

Due to the length and number of tables that contain the values and characteristics to determine each parameter they are presented in annex 2.

After calculating the Q value, the rock mass can be classified under the types showed on Table 7

Table 7 Type of rock mass under Q index criteria translated from (Oyanguren & Monge, 2004)

Type of rock mass	Q value
Exceptionally bad	10^{-3}-10^{-2}
Extraordinarily bad	10^{-2}-10^{-1}
Very bad	10^{-1}-1
Bad	1-4
Regular	4-10
Good	10-40
Very good	40-100
Extraordinarily good	100-400
Exceptionally good	400-1000

1.4.3. GSI classification (Oyanguren & Monge, 2004) (Duncan, 2018)

Developed to estimate the m_b and s parameters for the Hoek-Brown classification after realising that RMR was not adequate to relate failure criteria to geological observations specially for weak rock masses. The GSI is a modification of the RMR and Q classification as it was considered by Hoek-Brown that some of the parameters used were unnecessary for a breakage criterion. For RMR the discarded parameters are ground water conditions and orientation of the geological structure, in the case of the Q system ground water conditions and stress state SRF. This is due to the fact that on a breaking criterion, calculations are done in effective stresses thus not needing the water pressure. (Oyanguren & Monge, 2004)

GSI index is obtained after a careful visual inspection of the rock mass and it is mainly qualitative, Figure 35 shows the chart used with type of structures, the condition of the discontinuities' surface and the index assigned as a result applied to the case study of this project.

There are considerations in this index that adjust the assigned value, if the shear strength of the discontinuities is reduced by the presence of water the assigned grade is one less that what it should be. If the

analysis is done on a rock surface damaged by blasting activity the index should be moved a column towards the left.

As GSI is based on an isotropic behaviour of the rock mass it cannot be applied to rock masses with a dominant fractured direction, like slate masses, as the difference in strength between the rock and the discontinuities is too small to have an isotropic behaviour. It cannot be used in hard rock masses which present little to no fractures and the ones present have the same longitude as the height of the slope bench in this case the stability depends only on the behaviour of the discontinuity

1.4.4. RMR for rock slopes, SMR index (Oyanguren & Monge, 2004)

The Slope Mass Rating (SMR) is an adjustment to the RMR developed by Romana in (Romana, 1991) based on the following equation

$$SRM = RMR - (F_1 + F_2 + F_3) + F_4 \quad (2)$$

Where

- RMR is the calculated RMR for the rock mass
- $F_1 = \left[1 - sin(\alpha_J - \alpha_S)\right]^2$ α_j trend angle of discontinuities α_s slope trend angle
- $F_2 = \left(tan\beta_j\right)^2$ β_j dip angle of discontinuity if toppling is the most probable failure F_2=1
- F_3 relation between the dip angle of the joint and the rock slope, this value is obtained from Table 8

Table 8 Reduction factor for discontinuity orientation

Discontinuity orientation	Value
Very favourable	0
Favourable	-5
Regular	-25
Unfavourable	-50
Very unfavourable	-60

- F_4 factor related to the excavation method, slope in natural conditions (natural erosion, vegetation etc) +15, excavated with pre-splitting techniques +10, excavated with smooth blasting techniques +8, excavated with correctly done blasts 0, excavated with faulty blast that could have diminish the stability -8, excavated with rip techniques 0 (as this is only possible on soft rocks the method nor improves neither worsens stability)

This assessment method is indicated for preliminary stages of the project

1.5. Predominant weathering mechanism in arctic climate regions

In temperate climates the weathering mechanisms are a mixture of biological, chemical, and physical processes. In the arctic region the almost all year long sub-zero temperatures make the biological and chemical processes so slow that can be neglected.

Arctic regions are characterized for the presence of permafrost and high availability of water thus the main weathering mechanism are governed by these two factors.

Permafrost is defined as ground that stays below 0º C for two consecutive years

1.6. Slope failure modes and analyses

There are two developed methods or models to describe and analyse the stability and mode of failure of a slope: the limit equilibrium analysis (LEA) and the shear strength reduction (SSR). For the purpose of this project only the SSR method has been used for the subsequent analysis.

Limit equilibrium analysis had been the standard in the industry since its conception and are still used nowadays due to its reliability and number of cases analysed around the world which provides cases to study. The shear strength reduction method has started to gain popularity due to its powerfulness and flexibility while at the same time computers had become more powerful making this method time-cost effective.

In this section first LEA is going to be described for each of the different types of slope failure, secondly the SSR will be explained in general as it doesn't have different approaches depending on the type of failure mechanism as the LEA has.

1.6.1. Limit equilibrium analysis (LEA) methods

Plane (Duncan, 2018) (Oyanguren & Monge, 2004)

The plane failure is an uncommon type of failure as the required geometrical conditions are rarely met. Being the simplest mechanism, it is easy to understand failure concepts that will be more complicated on the complex failure types.

The conditions for this failure to happen are

- The strike of the sliding plane must be parallel with a ± 20 ° difference to the slope face
- The dip of the sliding plane must be less than the dip of the slope face $\Psi_p < \Psi_f$ check Figure 12
- The dip of the plane must be larger than the angle of friction $\Psi_p > \phi$ check Figure 12

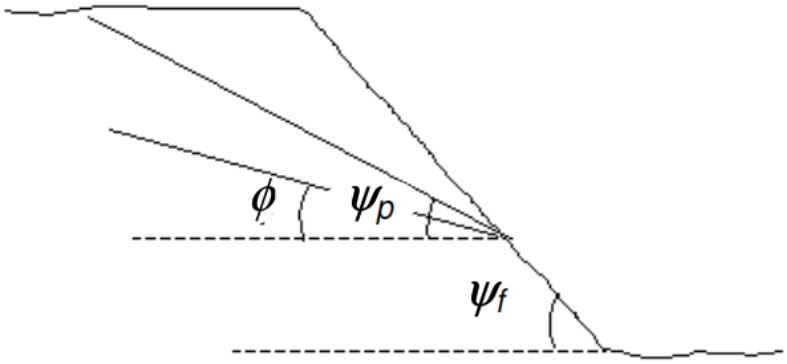

Figure 12 angle condition for plane failure (Oyanguren & Monge, 2004)

- The upper end of the sliding surface either intersects the upper slope, or terminates in a tension crack
- The presence of another two discontinuities that create lateral release surfaces that represent the lateral boundaries.

To analyse this failure the case used is the one with a tension crack in the upper surface of the slope as seen in Figure 13

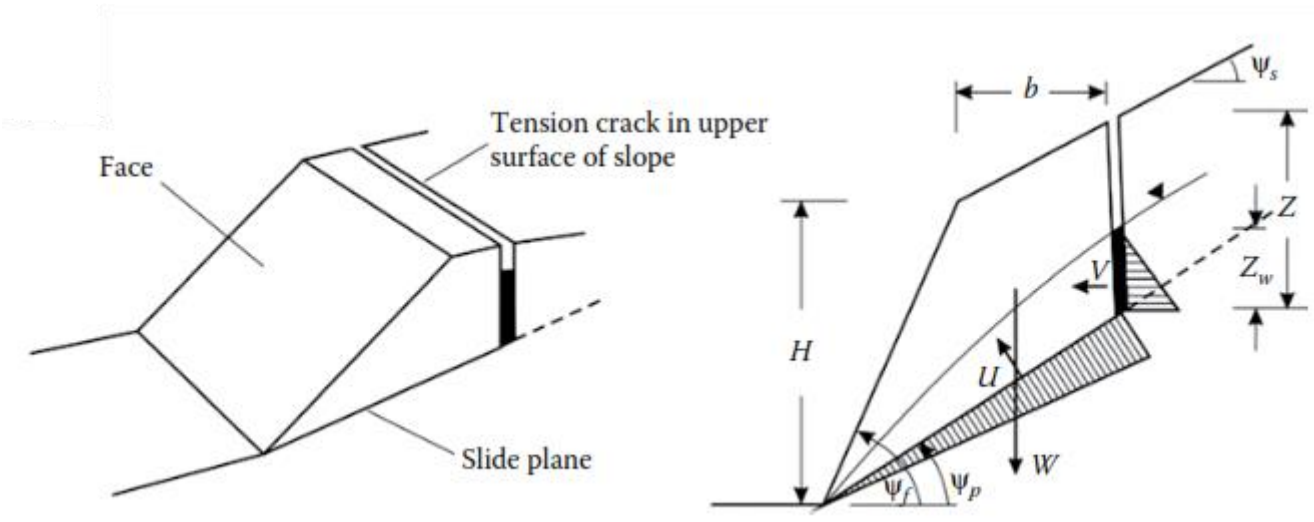

Figure 13 Plane failure with schematics of the forces involved (Duncan, 2018)

As assumptions:

- The sliding surface and tension crack strike parallel to the slope
- The tension crack is filled with water up to z_w
- The water pressure is represented by the greyed-out area in the force schematics on Figure 13
- The forces are supposed to act in the centroid of the mass thus producing no moments, the error introduced by this is neglectable if not used in steep slopes with steeply dipping discontinuities.
- The shear strength of the sliding surface is defined by $\tau = c + \sigma tan\phi$ as the Mohr-Coulomb criteria. On a rough surface the apparent cohesion and friction angle are a tangent that takes into account the normal stress σ on the sliding surface, this stress can be obtained from the curves in Figure 14.

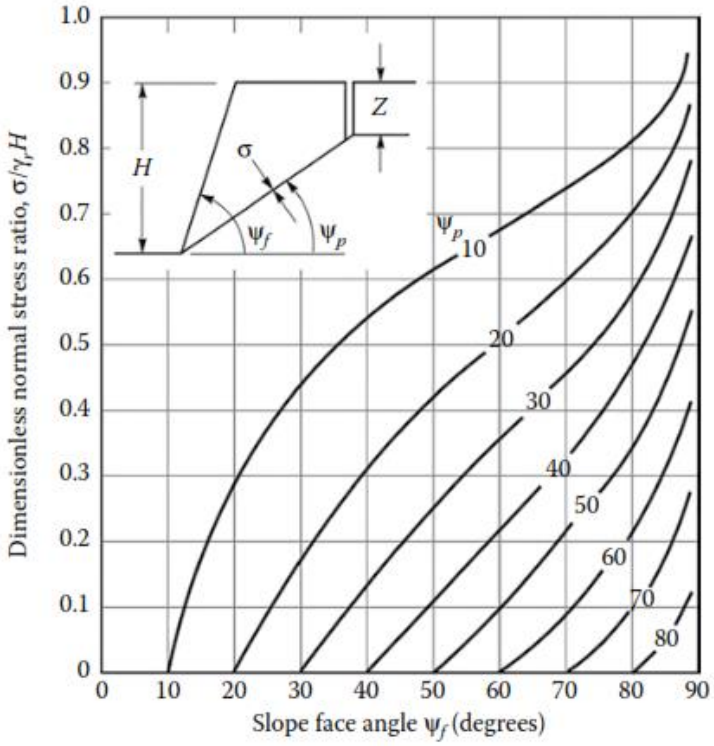

Figure 14 Normal stress on a sliding plane from (Duncan, 2018)

- There is no resistance on the lateral boundaries of the sliding block
- As the analysis is by-dimensional the area is represented by the length of the surface and the volume as the cross-section area of the block, due to the consideration of a slice of unit thickness at right angles to the slope face.

The factor of safety is FS is obtained as the ration between the resisting force and the driving force on equation 3

$$FS = \frac{Resisting force}{Driving force} = \frac{c * A + \sum N * tan\phi}{\sum S} \quad 3$$

Where c is cohesion, A is area of the sliding block, $\sum N$ sum of the normal forces, ϕ angle of friction and $\sum S$ sum of the shearing forces.

Using the example from Figure 13 equation 3 can be written as

$$FS = \frac{c * A + (W * \cos\psi_p - U - V * \sin\psi_p) * \tan\phi}{W * \sin\psi_p + V * \cos\psi_p} \quad (4)$$

A can be obtained from equation 5

$$A = (H + b * tan(\Psi_s) - z) * csc(\Psi_p) \quad (5)$$

Where H is height of the slope, b is the distance behind the slope crest at which the crack is located, z is crack depth, Ψ_s is the dip of the slope above the crest

As the crack is full of water up to a depth of z_w, U is the force in the sliding plane and V is the force in the tension crack. These forces can be calculated with equations 6 and 7

$$U = \frac{1}{2}\gamma_w * z_w * (H + b * tan(\Psi_s) - z) * csc\left(\Psi_p\right) \quad (6)$$

$$V = \frac{1}{2}\gamma_w * z_w^2 \quad (7)$$

γ_w is the unit weight of water

The weight of the block W is obtained with equation 8

$$W = \frac{1}{2}\gamma_r * H^2 \left[\left(1 - \frac{z}{H}\right)^2 * \cot\psi_p \left(\cot\psi_p * \tan\psi_f - 1\right]\right. \quad (8)$$

γ_r is the unit weight of the rock, ψ_f is the slope face angle, ψ_p is dip angle of the sliding plane

Particularising this case for the arctic region focusing on the ground water effects, during the melting season water runs into the cracks of the rock, building water pressure but this can be close to zero if the remaining rock mass is impermeable or the sliding plane contains a clay filling that has low conductivity. For this case U=0 and V is calculated with equation 7. In the case that the ground water cannot be discharged due to freezing conditions on the rock mass the uplift pressure can be approximated by a rectangular distribution with equation 9

$$U = A * p \quad (9)$$

Where A is the area of the sliding plane, equation 5, and p is the hydrostatic pressure obtained with equation 10

$$p = \gamma_w * z_w \quad (10)$$

This case is shown in Figure 15

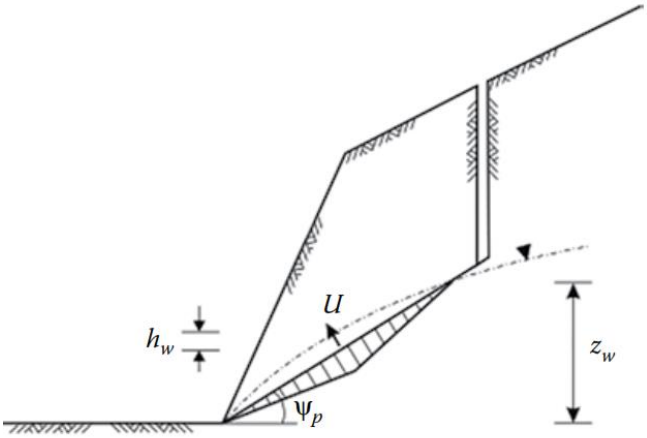

Figure 15 Sliding plane with a triangular distribution for the pressure in the case that the water table is below the base of the tension crack (Duncan, 2018)

One of the first symptoms to detect a block that is getting close to instability is the appearance of the explained tension cracks on the slope crest. This appears as a result of small movements on the rock mass with an accumulative effect, when the tension crack surfaces it can be supposed that shear failure has initiated.

Wedge (Duncan, 2018) (Oyanguren & Monge, 2004)

Type of failure controlled by two or more discontinuities characteristic of strong rock masses with well-defined discontinuities.

A wedge failure occurs when two planar discontinuities that strike obliquely to the face met on an intersection line creating a block that will slide along such intersection. Figure 16 shows a representation of this type of failure.

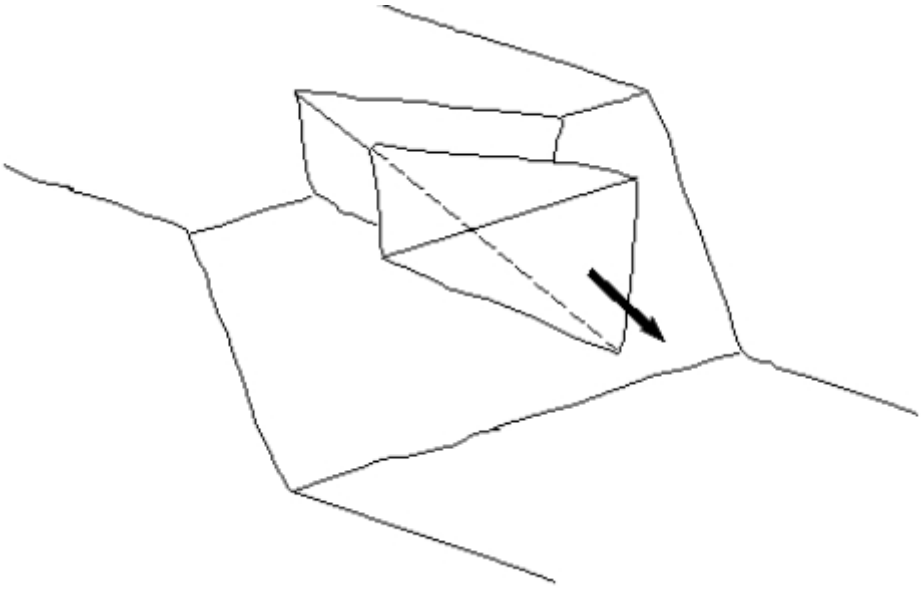

Figure 16 Wedge failure from (Oyanguren & Monge, 2004)

The conditions for a wedge failure are:

- Existence of two planes that intersect in a line, defined by its trend α_i and plunge Ψ_i
- The plunge of the intersection must be flatter than the dip of the face but higher than the angle of friction of both planes that define it $\Psi_f > \Psi_i > \phi$ as shown in Figure 17

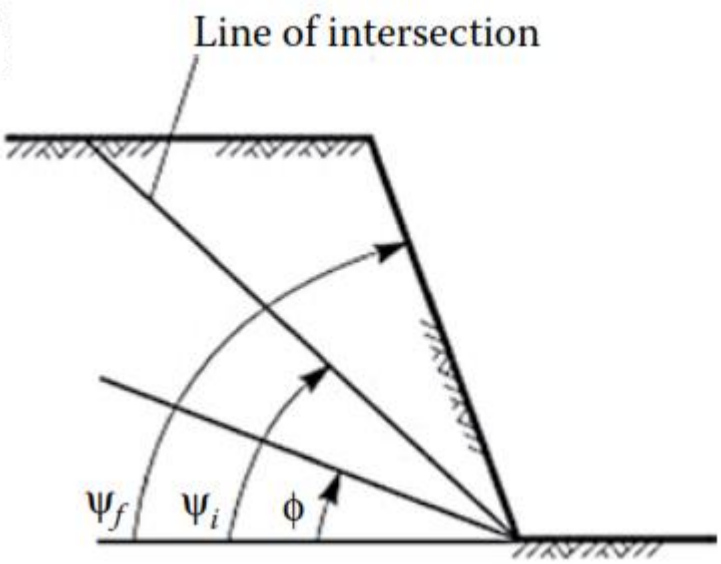

Figure 17 Types of angle for wedge failure from (Duncan, 2018)

- The line of intersection must dip outwards the face for the sliding to occur. The range is between α_i and α_i'

To obtain the trend α_i and plunge Ψ_i of the intersection between planes A and B equation 11 and 12 are used.

$$\alpha_i = tan^{-1}\left(\frac{tan(\Psi_A) * cos(\alpha_A) - tan(\Psi_B) * cos\ (\alpha_B)}{tan(\Psi_B) * sin(\alpha_B) - tan(\Psi_A) * sin\ (\alpha_A)}\right) \quad 11$$

$$\Psi_i = tan^{-1}(\tan(\Psi_A) * \cos(\alpha_A - \alpha_i)) = tan^{-1}(\tan(\Psi_B) * \cos(\alpha_B - \alpha_i)) \quad 12$$

α and Ψ are the trend and dip of the planes A and B that form the wedge, equation 11 gives two solutions separated by 180°, the correct value sits between α_A and α_B

The factor of safety on a wedge failure assuming the same friction angle ϕ for both planes is defined by equation 13

$$FS = \frac{(R_A + R_B) * tan(\phi)}{W * sin\ (\Psi_i)} \quad 13$$

R_A and R_B are the normal reactions from the planes $W * sin\ (\Psi_i)$ is the component of the weight along the intersection line.

The reactions are decomposed into normal and parallel with equations 14 and 15.

$$R_A * sin\left(\beta - \frac{1}{2} * \xi\right) = R_B * sin\left(\beta + \frac{1}{2} * \xi\right) \quad 14$$

$$R_A * cos\left(\beta - \frac{1}{2} * \xi\right) + R_B * cos\left(\beta + \frac{1}{2} * \xi\right) = W * cos\Psi_i \quad 15$$

The definition of the angles used in equations 14 and 15 can be found in Figure 18

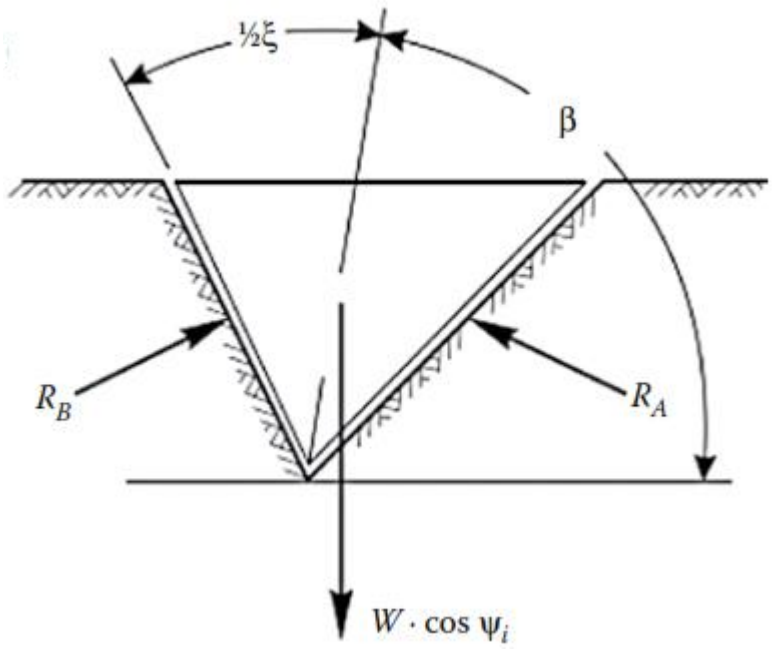

Figure 18 Angles and forces present on a wedge failure from (Duncan, 2018)

R_A and R_B are obtained with equation 16

$$R_A + R_B = \frac{W * cos(\Psi_i) * sin(\beta)}{sin\left(\frac{\xi}{2}\right)} \quad 16$$

Introducing equation 16 into equation 13 gives equation 17

$$FS = \frac{\frac{sin(\beta)}{sin\left(\frac{\xi}{2}\right)} * tan(\phi)}{tan(\Psi_i)} \quad 17$$

The wedge failure can be related to the plane failure through equation 18

$$FS_W = K * FS_P \quad 18$$

Where FS_w is the factor of safety for the wedge failure supported by friction and FS_p is the factor of safety for a plane failure that has the same Ψ_i as the intersection, K is a wedge factor that depends on ξ and β which can be obtained from the abacus in Figure 19

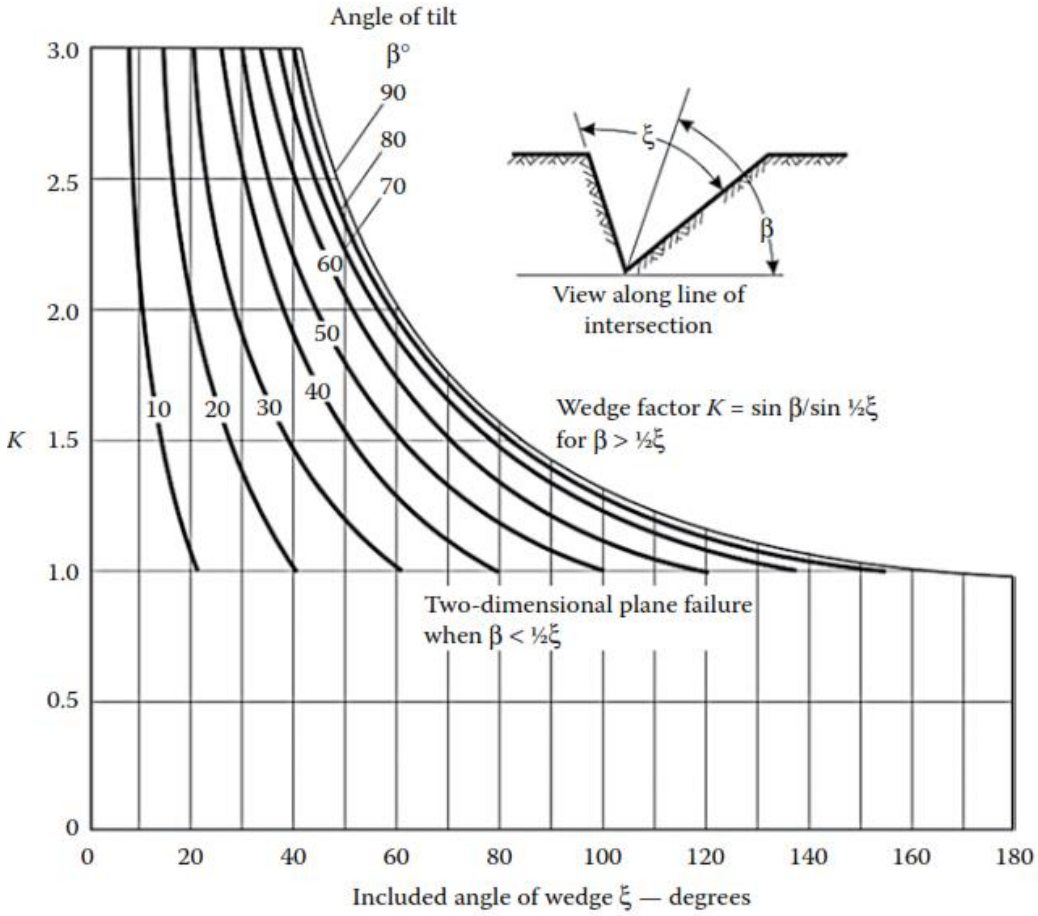

Figure 19 Abacus to obtain the K factor of a wedge failure (Duncan, 2018)

Circular (Duncan, 2018)

When the terrain is comprised of soil, debris or low quality and highly weathered rock mass the failure occurs through the whole mass following the line of least resistance. This type of failure is common in mine tailing dams, road slopes and natural slopes.

The failure occurs along a surface of failure with an approximately circular and concave shape that passes through the toe of the slope as shown in Figure 20

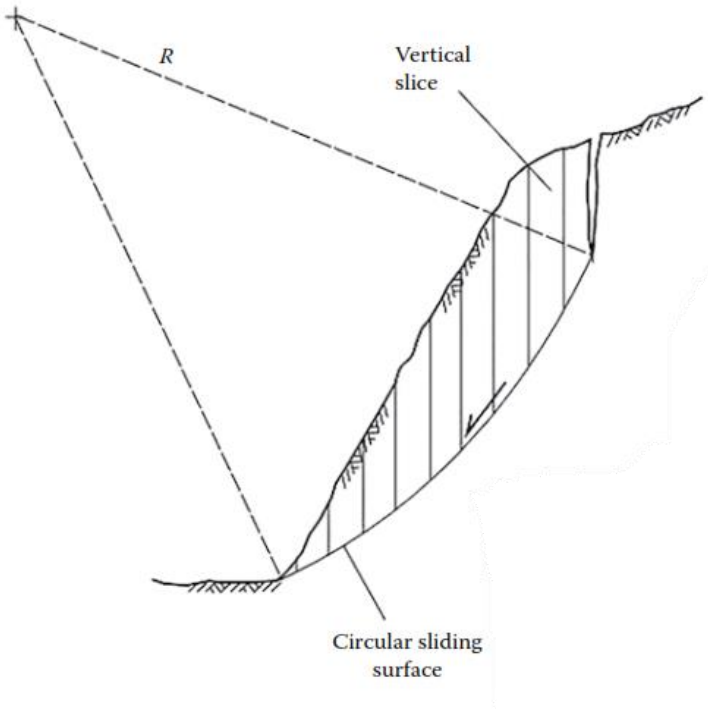

Figure 20 Scheme of a circular failure (Duncan, 2018)

The stability analysis of this kind of failures is done using the limit equilibrium procedure dividing the mass in slices, as shown in Figure 20. Each slice has an area A and an angle Ψ_p, in the easiest case the acting forces are the shear resistance S, cohesion (c) and friction angle ϕ, and forces E, dip angle Ψ and height h.

This process of analysis is iterative estimating an initial FS and refining it in each step. The number of equations depends on the number of slices used N, around 10 to 40 are needed for a realistic model, and the equilibrium conditions. If only force equilibrium is met the equations are 2N, if force and moment are met 3N is the number of equations. The number of unknows are 3N-1 for force criteria and 5N-2 for moment and force criteria. For the above the analysis are indeterminate and assumptions are made. (Duncan, 2018)

Equation 19 defines the factor of safety as:

$$FS = \frac{Shear\ strength\ available}{Shear\ stress\ needed\ for\ equilibrium} = \frac{[c + \sigma * tan(\phi)]}{(\tau_e)} \qquad 19$$

Equation 19 can be rearranged as

$$\tau_e = \frac{c + \sigma * tan(\phi)}{FS}$$

Frohlich (1955) cited in (Duncan, 2018) found that the lower bound for factors of safety that satisfy statics is obtained assuming that normal stress concentrates at a single point on the sliding surface. Research done by Spencer (1969) and Taylor (1937) using logarithmic spirals as sliding surfaces as seen in (Duncan, 2018) showed that factors of safety are closer to the lower bound of Frohlich with negligible differences making them accurate enough for day to day problems in simple circular failure.

The slice method for this type of failure is known as the Bishop and Janbu method, presenting differences between them in the application cases but with enough similarities to be described together.

Bishop method satisfies vertical and moment equilibrium with a circular surface, Janbu method can be used in any surface but only satisfies vertical equilibrium.

As seen in (Duncan, 2018) Nonveiller in 1965 noticed that the Janbu method should not be applied to deep slide surfaces with low-friction angles as the factor of safety will have a great error.

Using these methods is divided into different steps, the equations and factors that each step refer to are collected on Figure 23 and Figure 24 for Bishop and Janbu respectively.

1. Find sliding surface: defined by the profile of the slope. For circular failures the abacus shown in Figure 21 and Figure 22 present the centre of the sliding surface with the lowest safety factor. For the Janbu method the surface can be defined with weak zones and structural features. The analysis is iterative, and each run will use a slightly different surface until the lowest FS is found
2. Slice parameters: the surfaces are divided into slices defining for each of them the following parameters:
    a. Base angle Ψ_b
    b. Weight of the slice W
    c. Uplift of water force U
3. Shear-strength: using Mohr-Coulomb failure criteria if the same material applies for the whole surface the parameters will be the same for each slice, in the case of different materials the cohesion and friction angle have to be chosen taken them into account. If using nonlinear failure criteria cohesion and friction angle has to be calculated at the effective normal stress of each slice, this case is shown in Figure 25 for the Bishop's method.
4. FS iteration: after calculating all of the parameters needed (A,B,C,Q), starting with an FS value of 1 a new FS is obtained and used for the next iteration until the difference between steps is less than 0.001. This is regularly achieved after 7 iterations.
5. Corrections to the methods: Bishop requires two conditions to be met, first one is that the effective normal stress on each slice is always positive this is done through equation 9.8 in Figure 23, while this criteria fails on any slice a tension crack should be included into the analysis or the ground water force readjusted. Second one, equation 9.9 in Figure 23, verifies that the analysis is not invalidated by conditions that can exists if a deep slide surface has been assumed at the toe of a slope, all slices have to satisfy this condition if no the dimensions of them need to be changed, if is not solved in that way the analysis should be discarded. For the Janbu method equation 9.15 in Figure 24 shows the correction factor f_0, this factor is used to take into account the interslice forces that are a result of the slide surface assumed.

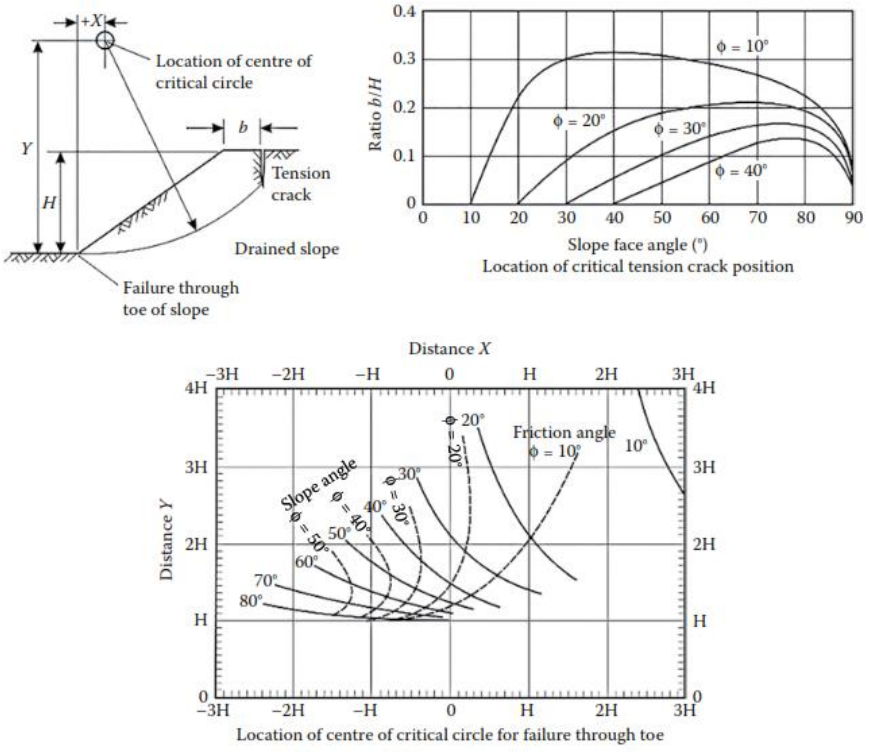

Figure 21 Location of critical sliding surface for circular shapes on drained slopes from (Duncan, 2018)

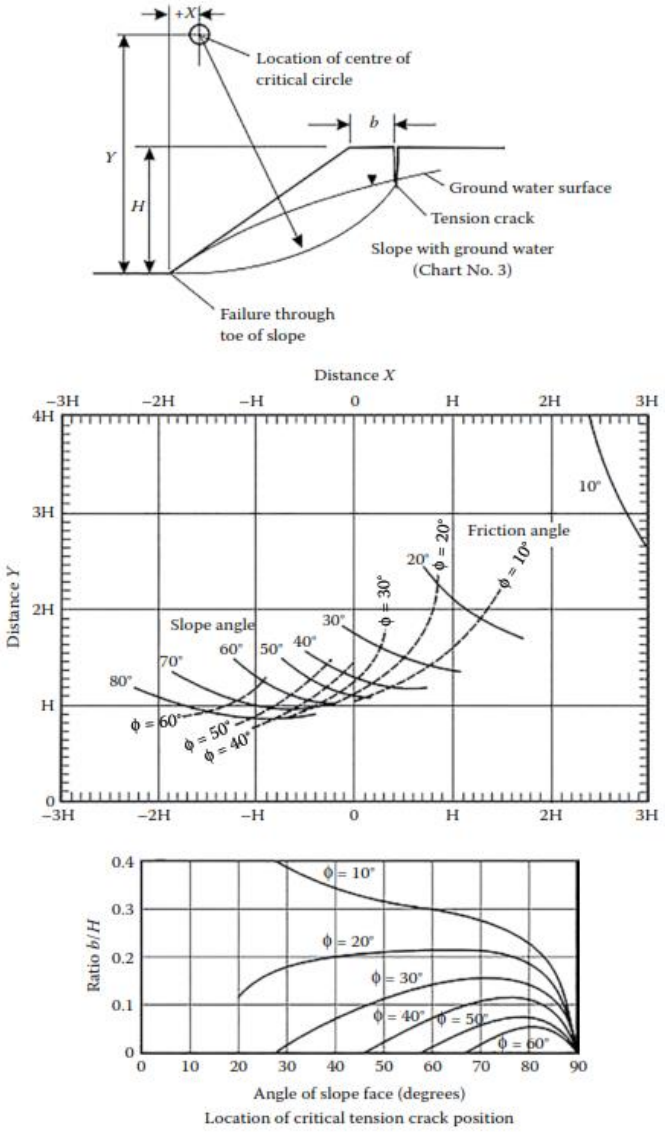

Figure 22 Location of critical sliding surface for circular shapes on slopes with ground water from (Duncan, 2018)

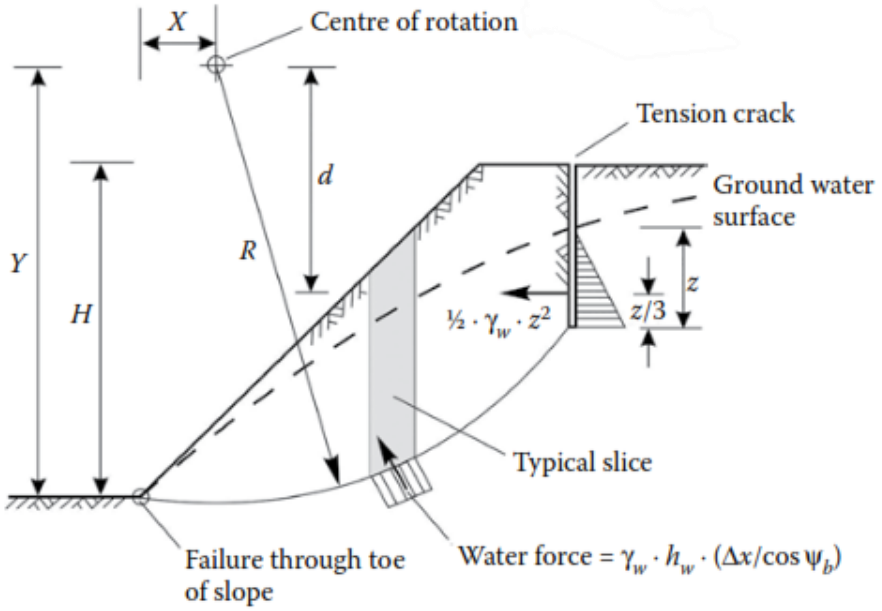

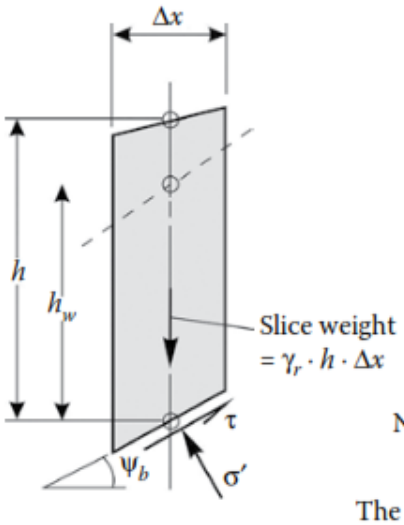

Factor of safety:

$$FS = \frac{\Sigma(A/(1+B/FS))}{\Sigma\,(C) + Q}$$

where

$$A = [c + (\gamma_r \cdot h - \gamma_w \cdot h_w) \cdot \tan\phi] \cdot (\Delta x/\cos\psi_b)$$
$$B = \tan\psi_b \cdot \tan\phi$$
$$C = \gamma_r \cdot h \cdot \Delta x \cdot \sin\psi_b$$
$$Q = \tfrac{1}{2} \cdot \gamma_w \cdot z^2 \cdot (d/R)$$

Note: Angle ψ_b is negative when sliding uphill

The following conditions must be satisfied for each slice:

1) $$\sigma' = \frac{\gamma_r \cdot h - \gamma_w \cdot h_w - c\,(\tan\psi_b/FS)}{1 + B/FS} \qquad (9.8)$$

2) $$\cos\psi_b\,(1+B/FS) > 0.2 \qquad (9.9)$$

Figure 23 Bishop's slice method from (Duncan, 2018)

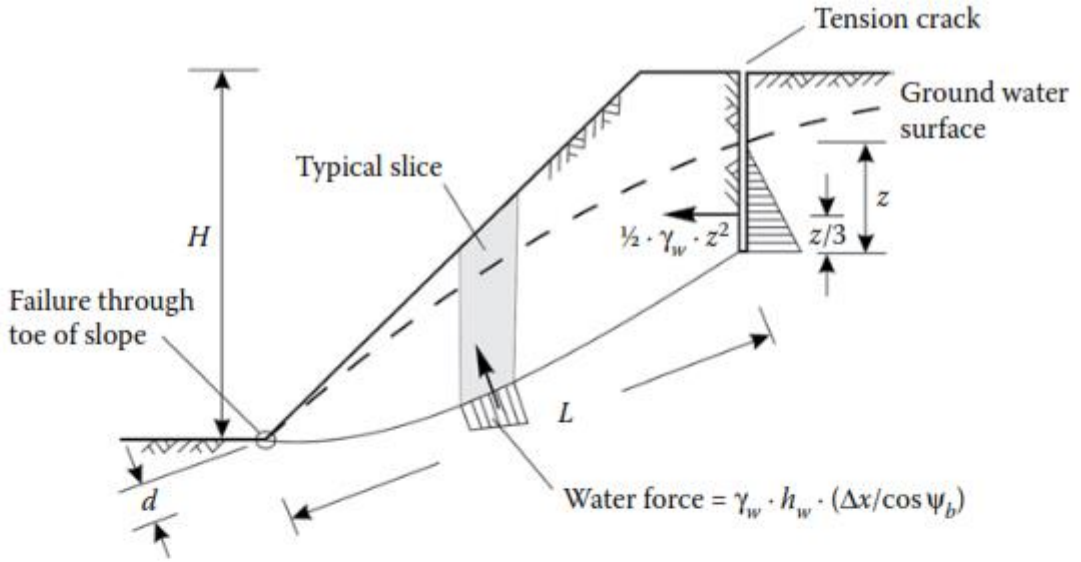

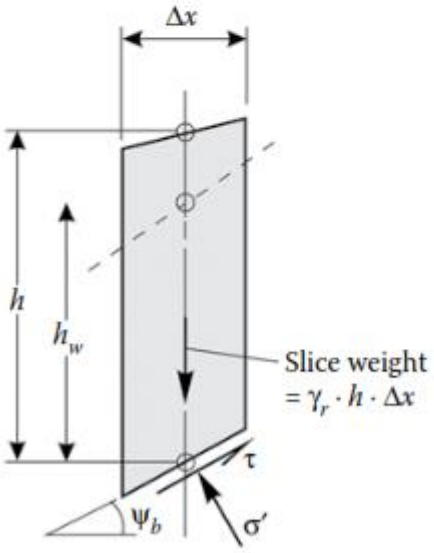

Factor of safety:

$$FS = \frac{f_o \cdot \Sigma\,(A/(1 + B/FS))}{\Sigma\,(C) + Q}$$

where

$$X = [c + (\gamma_r \cdot h - \gamma_w \cdot h_w)\tan\phi] \cdot (1 + \tan^2\psi_b)\,\Delta x$$

$$Y = \tan\psi_b \cdot \tan\phi$$

$$Z = \gamma_r \cdot h \cdot \Delta x \cdot \tan\psi_b$$

$$Q = \tfrac{1}{2} \cdot \gamma_w \cdot z^2$$

Note: Angle ψ_b is negative when sliding uphill

Approximate correction factor f_o

$$f_o = 1 + K(d/L - 1.4(d/L))^2 \qquad (9.15)$$

for $c' = 0; K = 0.31$

$c' > 0, \phi' > 0; K = 0.50$

Figure 24 Janbu's slice method from (Duncan, 2018)

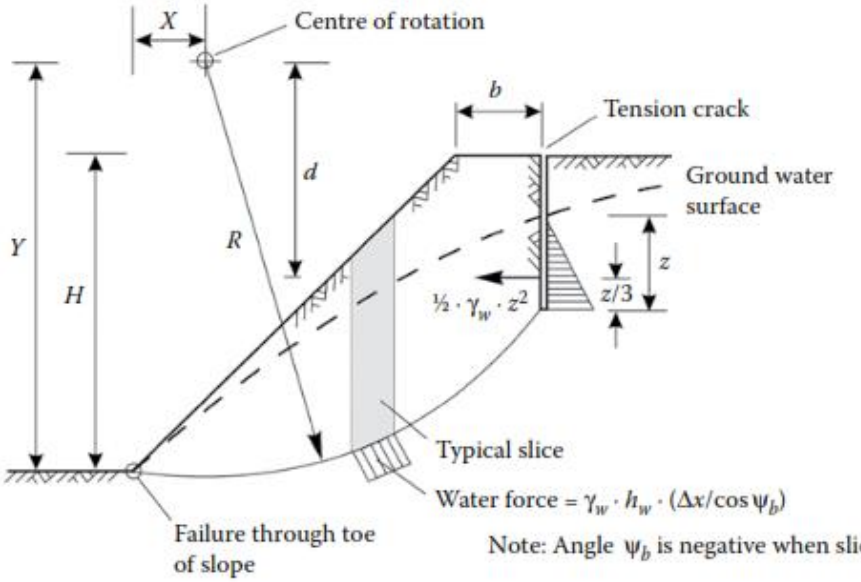

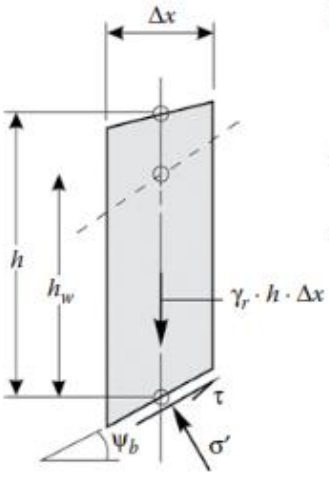

Factor of safety:

$$FS = \frac{\Sigma\,(c_i' + \sigma' \cdot \tan\phi_i')\,(\Delta x/\cos\psi_b)}{\Sigma(\gamma_r \cdot h \cdot \Delta x \cdot \sin\psi_b) + \tfrac{1}{2} \cdot \gamma_w \cdot z^2 \cdot d/R}$$

where

$$\sigma' = \gamma_r \cdot h \cdot \cos^2\psi_b - \gamma_w \cdot h_w \qquad \text{(Fellenius solution)}$$

and

$$\sigma' = \frac{\gamma_r \cdot h - \gamma_w \cdot h_w - (c_i' \cdot \tan\psi_b/FS)}{1 + \dfrac{\tan\phi_i' \cdot \tan\psi_b}{FS}} \qquad \text{(Bishop solution)}$$

$$\phi_i' = \sin^{-1}\left[\frac{6 \cdot a \cdot m_b(s + m_b \cdot \sigma_{3n}')^{a-1}}{2(1+a)(2+a) + 6 \cdot a \cdot m_b(s + m_b \cdot \sigma_{3n}')^{a-1}}\right]$$

$$c_i' = \frac{\sigma_{ci}[(1+2 \cdot a)s + (1-a)m_b \cdot \sigma_{3n}'](\sigma + m_b \cdot \sigma_{3n}')^{a-1}}{(1+a)(2+a)\sqrt{1 + [6 \cdot a \cdot m_b(s + m_b \cdot s_{3n}')^{a-1}][(1+a)(2+a)]}}$$

where $\sigma_{3n} = \sigma_{3\max}'/\sigma_{ci}$; see Equation 5.17 for parameter a

The conditions which must be satisfied for each slice are:

1) $\sigma' > 0$, where σ' is calculated by Bishop's method

2) $\cos\psi_b\,[1 + (\tan\psi_b \cdot \tan\phi_i')/FS] > 0.2$

Figure 25 Bishop's method for nonlinear defined materials (Duncan, 2018)

Toppling (Duncan, 2018)

This kind of failure occurs when the trend of the discontinuity is close to the one of the slope and has a hard plunge towards the inside of the rock mass.

There are three main toppling mechanism

1. Block toppling: in hard rock masses, discontinuities dipping steeply into the face combine with orthogonal joints to define columns and its height, respectively. The columns at the toe are pushed by the loads from the columns behind that allows toppling development up the slope. Bedded sandstone and columnar basalt are traditional rock types for this type of failure. Figure 26 shows in a simplified way a block toppling.

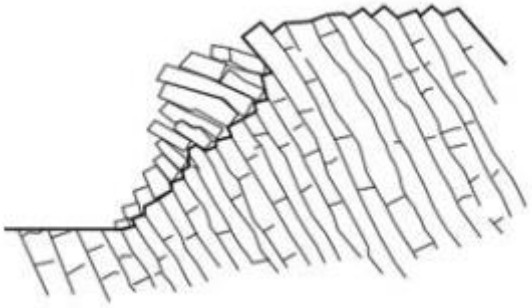

Figure 26 Block toppling from (Duncan, 2018)

2. Flexural toppling: following the same structure as a block topping in this case the orthogonal joints are not developed enough so the columns flex and bend forward as shown in Figure 27. This usually happens in thin bedded shale and slate types of rocks. Erosion or excavation of the toe starts the toppling process.

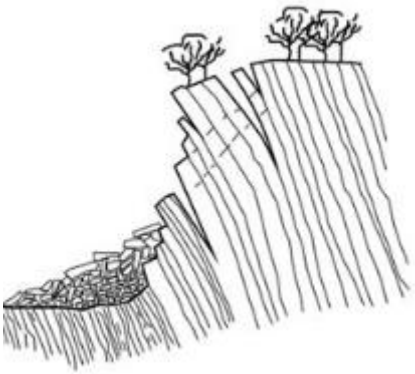

Figure 27 Flexural toppling from (Duncan, 2018)

3. Block-flexure toppling: this type of toppling is a mixture between the previous modes, it follows a pseudo flexure along columns which are divided in blocks by the numerous cross-joints present. The movement occurs due to the accumulation of displacements in the cross joints, this produces a much lower amount of tension cracks than in flexural toppling and less voids than block toppling Figure 28 shows this type of failure.

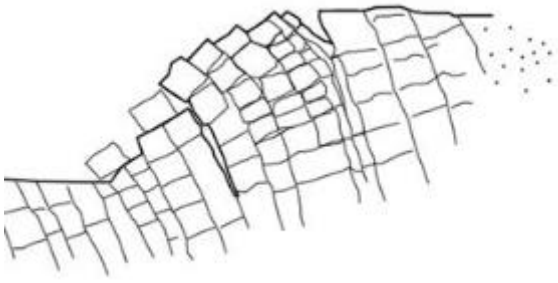

Figure 28 Block flexural toppling from (Duncan, 2018)

To calculate the block toppling stability in the book by (Duncan, 2018) are defined 7 steps which are included here, blocks are numbered from toe upwards:

1. Calculate number and size of the blocks with equation 20 to 25. Where H slope height, Ψ_b angle of base plane, Ψ_f angle of face, Ψ_p dip of the base of the blocks, Ψ_s angle of the upper slope above crest

$$n = \frac{H}{\Delta x}\left[csc\Psi_b + \left(\frac{cot\Psi_b - cot\Psi_f}{sin(\Psi_b - \Psi_f)}\right) * sin\Psi_s\right] \quad 20$$

$$y_n = n(a_1 - b) \quad 21$$

$$y_n = y_{n-1} - a_2 - b \quad 22$$

$$a_1 = \Delta x * tan(\Psi_f - \Psi_p) \quad 23$$

$$a_2 = \Delta x * tan(\Psi_p - \Psi_s) \quad 24$$

$$b = \Delta x * tan(\Psi_b - \Psi_p) \quad 25$$

2. Friction angles for base ϕ_p and sides ϕ_d are obtained by lab testing or inspection, ϕ_p should be greater than Ψ_p to prevent sliding
3. Using equation 26 the toppling condition is evaluated starting with the top block. For the upper toppling block the forces to prevent toppling and sliding are calculated with equations 27 and 28 respectively.

$$\frac{\Delta x}{y} < tan\Psi_p \quad 26$$

$$P_{n-1,t} = P_n \quad 27$$

$$P_{n-1,s} = P_n W_n \quad 28$$

4. n_1 is the uppermost block of the ones that topple
5. On block n_1 determine $P_{n-1,t}$ and $P_{n-1,s}$ if $P_{n-1,t} > P_{n-1,s}$ the block is on the toppling point and P_{n-1} is equal to $P_{n-1,t}$ on the opposite case if $P_{n-1,s} > P_{n-1,t}$ the block is on the sliding point and P_{n-1} is set to $P_{n-1,s}$. It is also necessary to check if the block doesn't slide at the base which means $R_n > 0$ with $\left(|S_n| > R_n * tan(\phi_p)\right)$
6. The analysis in step 5 is continued for the lower blocks. A block can topple even if equation 26 is not met if the force applied is high enough satisfying the conditions on step 5. If all blocks met $P_{n-1,t} > P_{n-1,s}$ the toppling occurs down to block 1 and sliding is not present.
7. If a block satisfies $P_{n-1,s} > P_{n-1,t}$ this block is n_2 and all the subsequent blocks lie into the sliding critical state

In the case of external forces (ground water, anchors, earthquakes…) actuating on the slope the limit equilibrium analysis allows to introduce additional forces to the ones already analysed if its direction, point of application and magnitude are known. To explain the modifications to the equations, the block diagram in Figure 29 and the steps from (Duncan, 2018) are going to be followed.

The external forces to be analysed are Q with angle Ψ_Q, ground water V_1 V_2 and V_3. The other forces present are P_n and P_{n-1} produced by the blocks above and below. With these external forces into account equations 27 and 28 are modified in the following way:

$$P_{n-1,t} = \left\{ P_n(M_n - \Delta x * tan\phi_d) + \frac{W_n}{2} * \left(y_n * sin\Psi_p - \Delta x * cos\Psi_p\right) + \frac{V_1 * y_w}{3} + \frac{y_w * \Delta x^2}{6} \right.$$
$$\left. * cos\Psi_p(z_w + 2y_w) - \frac{V_3 * z_w}{3} + Q\left[-sin\frac{\left(\Psi_Q - \Psi_p\right) * \Delta x}{2} + cos\left(\Psi_Q - \Psi_p\right) * y_n\right]\right\} L_n^{-1} \quad (29)$$

$$P_{n-1,s} = P_n + \left\{-W\left(cos\Psi_p * tan\phi_p - sin\Psi_p\right) + V_1 - V_2 * tan\phi_p - V_3 + Q \right.$$
$$\left. * \left[-sin\left(\Psi_Q - \Psi_p\right) * tan\phi_p + cos\left(\Psi_Q - \Psi_p\right)\right]\right\} * \left(1 - tan\phi_p * tan\phi_d\right)^{-1} \quad (30)$$

The values for the water force V_1, V_2 and V_3 are calculated with equations 31 to 33

$$V_1 = \frac{1}{2}\gamma_w * cos\Psi_p * y_w^2 \quad (31)$$

$$V_2 = \frac{1}{2}\gamma_w * cos\left[\Psi_p(y_w + z_w)\right] * \Delta x \quad (32)$$

$$V_3 = \frac{1}{2}\gamma_w * cos\Psi_p * z_w^2 \quad (33)$$

The rest of the analysis is as previously described but using the modified equations instead of the regular ones.

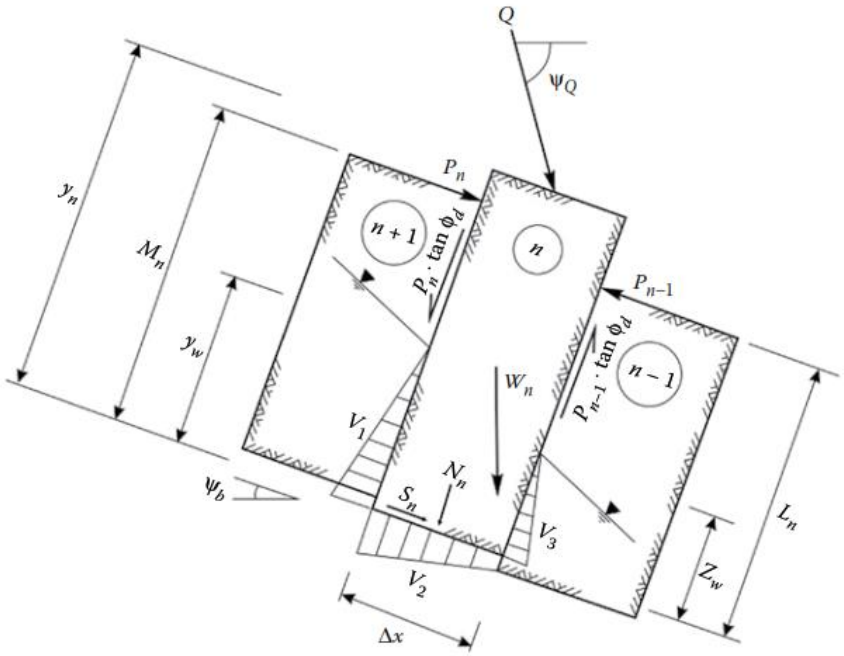

Figure 29 Example for external forces application from (Duncan, 2018)

1.6.2. Shear strength reduction method

The shear strength reduction method presents advantages to the LEA method showed in the previous section. It is a type of analysis based on finite elements FE calculations and its advantages relies on:

- Elimination of a priori assumptions on the shape and location of failure surfaces
- Elimination of assumptions regarding the inclinations and locations of interslice forces
- Capability to model progressive failure
- Calculation of deformations at slope stress levels
- Ability to perform successfully under a wide range of conditions. (Hammah, Curran, Yacoub, & Corkum, 2004)

SSR is based on reducing the strength parameters of the material by a factor and computing the finite element analysis. For this project, the parameters and behaviour employed are those of Mohr-Coulomb.

The simplicity, explicit representation in both principal and shear-normal stress space, adequate description of strength behaviour for a wide range of materials, and easy-to-obtain parameters of the Mohr-Coulomb criterion account for its popularity, being the most widely applied failure criterion in geotechnical engineering. (Hammah, Curran, Yacoub, & Corkum, 2004)

The SSR method reduces the Mohr-Coulomb parameters by a factor using equations 34 and 35 (Rocscience, 2004)

$$c^* = \frac{c}{F} \quad 34$$

$$\phi^* = \tan^{-1}\left(\frac{\tan\phi}{F}\right) \quad 35$$

On equations 34 and 35 the parameters are:

- c Mohr-Coulomb cohesion
- c^* Mohr-Coulomb reduced cohesion
- ϕ Mohr-Coulomb reduced friction angle
- ϕ^* Mohr-Coulomb reduced friction angle
- F Stress reduction factor

This process that is used during an SSR analysis follows the next steps:

1) Develop an FE model of a slope, using the appropriate material deformation and strength properties. Compute the model and record the maximum total deformation.
2) Increase the value of F (Stress Reduction Factor) and calculate factored Mohr-Coulomb material parameters with equations 34 and 35 above. Enter the new strength properties into the slope model and re-compute. Record the maximum total deformation.
3) Repeat 2, using systematic increments of F, until the FE model does not converge to a solution, i.e. continue to reduce material strength until the slope fails. The critical F value just beyond which failure occurs will be the slope factor of safety. (Hammah, Curran, Yacoub, & Corkum, 2004)

The tolerance parameter is what determines if the analysis has converged, the tolerance used for the simulations was set at 0.001. The simulation converges when the following two criteria are met:

1) Difference in Stress Reduction Factor (SRF) between two iterations of the SSR method is less than the tolerance
2) The Stress Analysis has converged to the SSR iteration with the lower SRF, but does not converge for the SSR iteration with the higher SRF (Rocscience)

In the case that the slope has a factor of safety below 1, the fractional F values are decremented which increases the factored strength parameters until the slope becomes stable.

If probabilistic analysis is used at the same time, this process is repeated for each change on the defined variables.

The step between SRF iterations was set as automatic.

1.7. Probabilistic analysis

The probabilistic analysis used in this project and used by Phase 2 is the Rosenblueth's point estimate method, developed by (Rosenblueth, 1975).

In this method random variable distributions are represented by two-point estimates at plus/minus one standard deviation from the mean. The FEM is resolved for each possible combination of point estimates which produces 2^m solutions which m is the number of variables involved. (Rocscience)

1.8. Mohr-Coulomb parameters from GSI and Hoek-Brown fieldwork data

(Hoek, Carranza-Torres, & Corkum, 2002) cited on (Hammah, Curran, Yacoub, & Corkum, 2004) presents a method to obtain Mohr-Coulomb equivalent parameters based on field data obtained under Hoek-Brown and GSI criteria. (Hoek, Carranza-Torres, & Corkum, 2002) define the equivalent Mohr-Coulomb criterion as that, which over a specified stress interval, minimizes the area between linear model and the Hoek-Brown curve. (Hammah, Curran, Yacoub, & Corkum, 2004)

The formulas to calculate the equivalent Mohr-Coulomb parameters are:

$$m_b = m_i * e^{\left(\frac{GSI-100}{28-14D}\right)} \quad (36)$$

$$s = e^{\left(\frac{GSI-100}{9-3D}\right)} \quad (37)$$

$$a = \frac{1}{2} + \frac{1}{6} * \left(e^{-\frac{GSI}{15}} - e^{-\frac{20}{3}}\right) \quad (38)$$

m_i is a material constant for the intact rock

m_b is a reduced value for m_i

s and a are rock mass constants

D characterizes the degree of stress relaxation have disturbed the rock mass

s_{ci} uniaxial compressive strength

$$f' = \sin^{-1}\left[\frac{6am_b(s + m_b s'_{3n})^{a-1}}{2(1+a)(2+a) + 6am_b(s + m_b s'_{3n})^{a-1}}\right] \quad (39)$$

$$c' = \frac{s_{ci}(1+2a)s + (1-a)m_b s'_{3n}(s + m_b s'_{3n})^{a-1}}{(1+a)(2+a)\sqrt{1 + \frac{6am_b(s + m_b s'_{3n})^{a-1}}{(1+a)(2+a)}}} \quad (40)$$

$$s'_{3n} = \frac{s'_{3max}}{s_{ci}} \quad (41)$$

The fitting procedure occurs over a stress range from s_t, the tensile strength, to the maximum compressive stress s'_{3max} in the slope which is calculated with equation 42

$$s'_{3max} = 0.72 s'_{cm} \left(\frac{s'_{cm}}{gH}\right)^{0.91} \quad (42)$$

g is the rock mass unit weight

H is the slope height

s'_{cm} is the rock mass strength which is calculated with equation 43

$$s'_{cm} = s_{ci}\frac{(m_b + 4s - a(m_b - 8s))\left(\frac{m_b}{4+s}\right)^{a-1}}{2(1+a)(2+a)} \quad 43$$

1.9. Previous master topic

Previously to develop this topic for the master thesis, work on improving the separation method for the coal extracted at mine 7 in Longyearbyen was conducted. This work involved finding separation methods employed in the mining industry that will be suitable for the climatic conditions present in the area and will continue by developing and building a test bench for the selected separation method.

This project was put to a halt due to the outbreak of the COVID-19 pandemic which force the finding and developing of the topic that covers this thesis. The job conducted until that point can be found in annex 1

2. Analysis of the region

After the description of the different rockfall and weathering mechanisms in chapter 1, in this section the area of study is going to be described morphologically and geologically, at the same time the tasks performed during fieldwork, geological inspection and DTM (Digital Terrain Model) acquisition will be described.

Figure 30 shows the study area with the location of the Bamsebu cabin, this area is located on the road that connects Longyearbyen with Bjørndalen.

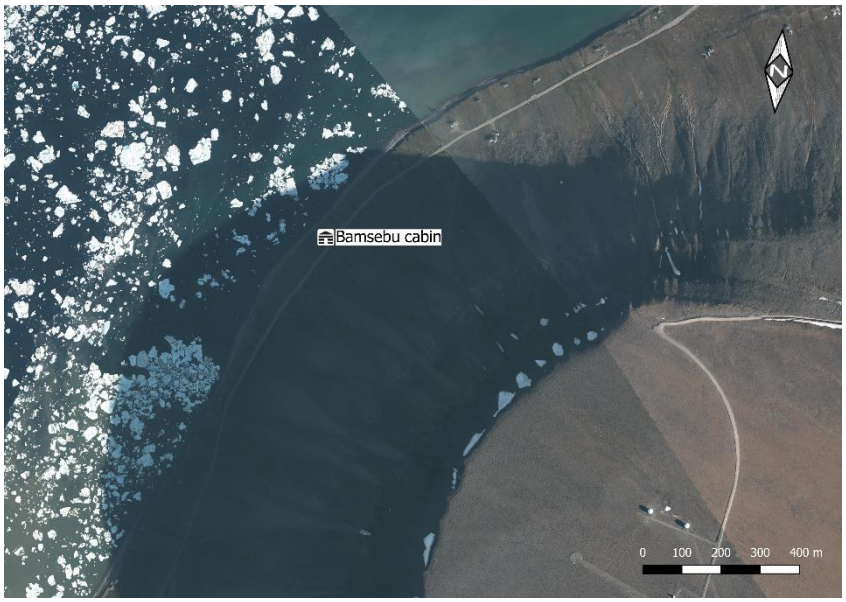

Figure 30 Location of the cabin in the analysis area. Map from (Norwegian Polar Institute) modifications by (Viejo)

According to Figure 31 extracted from the Geology of Svalbard book (Norwegian Polar Institute, 2007) the area of study presents strata from the tertiary geological period which is mainly made of sandstones and shales.

Figure 31 Location of tertiary geological formations (Norwegian Polar Institute, 2007)

From the cabin position the study area is shown in Figure 32 with a closer look at the outcrops in Figure 33.

Figure 32 Study area from the cabin location (Viejo)

2.1. Geological inspection

The rock outcrops have been numbered from right to left as shown in Figure 33 local terrain reconnaissance has been done on the outcrops 3, 4 and 5. For number 3 it was done on the left side of the outcrop, for number 4 it was done on the left side and for number 5 it was conducted on the centre area that connects 4 and 5 and also at the right side of the toe of the outcrop.

Figure 33 Studied rock outcrops 1 to 7 from right to left

In general the rock mass presents joints with up to 2 to 3 cm separation between edges as seen in Figure 34, some of the joints have clay and organic material infilling that will reduce its bearing capacity and rating. The horizontal joints that divide the rock mass in blocks doesn't present separation between the edges and in the cases that are separated is approximately half the width of the vertical ones as seen in the general picture shown in Figure 34. The edges of the discontinuities present JRC values between 2 to 6 according to the comparison chart from Barton and Choubey in (Evert, 2006)

A

B

Figure 34 A) distance between joint faces B) moss and clay was present in some fractures

Employing the GSI (geological strength index) charts the rock masses present a surface condition of the discontinuities between poor and fair with a structure between C and D classes the GSI range sits among 33 to 38. In Figure 35 is presented the table used for the GSI estimation, each line represents a 5 point value.

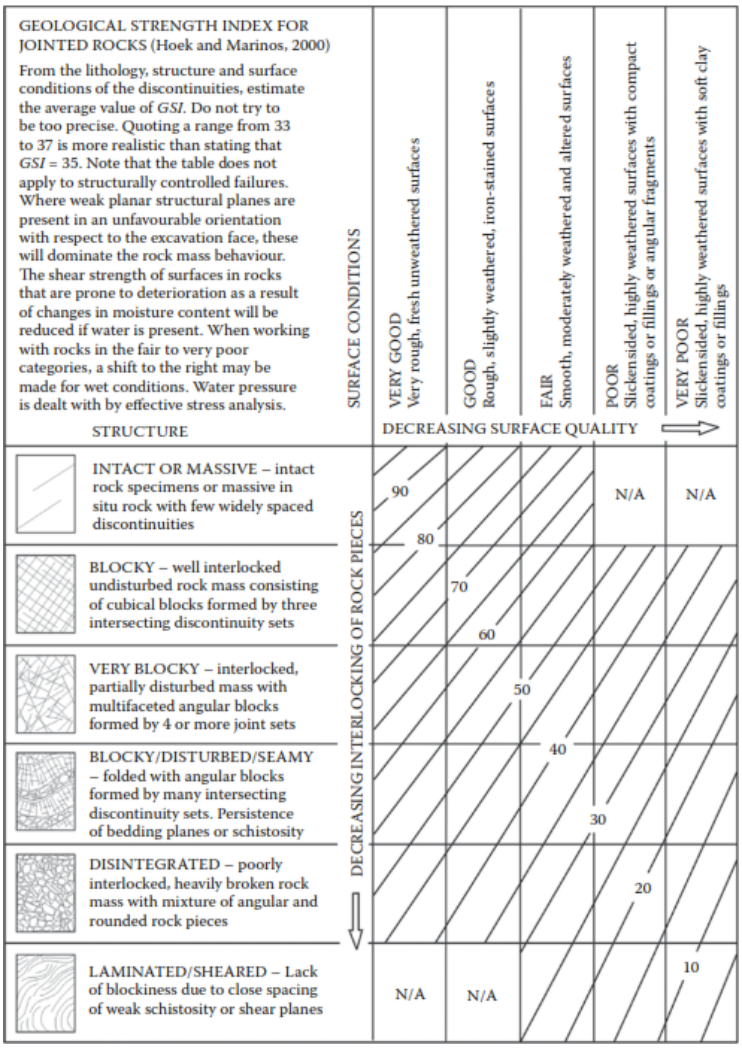

Figure 35 Table used for GSI estimation (Duncan, 2018)

Data about the strength of the rocks was obtained from Jean Gabriel Dorval (Dorval, 2020, p. Unpublished) and is presented in Table 9

Table 9 First cracking of rock from (Dorval, 2020)

Test	Mass applied	Force applied	Stress applied	
	Kg	N	kPa	MPa
2	400	3924	222.05	0.22205
3	1000	9810	555.13	0.55513
4	800	7848	444.11	0.44411

Figure 36 View of the left side of the fourth rock outcrop

Apart from the geomechanical classification done with the field data, samples extracted from outcrops 3, 4 and 5 in the form of blocks obtained from the wall were used to determine the density which will later be used as one of the input parameters for the simulations, in addition to that a rock piece from the area between outcrop 3 and 4 was also tested. The rock blocks are displayed in Figure 37

Figure 37 Samples collected for the density tests

2.1.1. Density measurement

The density of the rocks was obtained through the Archimedes principle by measuring the difference in the height of the water contained in a bucket, and as a consequence the volume, with and without the different rock blocks submerged on it.

The bucket used shown Figure 38 has a diameter of 18 cm and was filled with water up to 12 cm which was enough to cover the rock pieces. The empty volume of the bucket was calculated with equation 44

Figure 38 Bucket used and inside diameter

$$V = \pi * r^2 * h \quad (44)$$

The initial volume of water in the bucket was 3053.628 cm³ after that the rock fragments were introduced one by one and the change of height measured at the same point, to ensure that the measuring point was marked at the bottom of the bucket. By the end of the project inaccuracies were found on the method used, which changed the equation 44 for equation 45.

$$V = \frac{1}{3} * \pi * h * (R^2 + r^2 + R * r) \quad (45)$$

As a result, the obtained results changed for the ones in the corrected density values column. The results of this tests are shown in Table 10. Due to time constrains these values were not used in the simulations.

Table 10 Density values

Rock fragment	Density (kg/m³)	Corrected Density (kg/m³)
Zone 3	3400	3045
Zone 4	2859	2983
Zone 5	3638	2939
Area between 3 and 4	2745	2227

To obtain the density of the rocks on a saturated state the samples were submerged in water for 24 h, after that the same samples were weighted on the wet state and the same procedure was followed to obtain the saturated density, the results are in Table 11.

Table 11 Saturated density values

Rock fragment	Saturated density (kg/m³)	Corrected saturated density (kg/m³)
Zone 3	3423	3064
Zone 4	2916	3037
Zone 5	3697	2964
Area between 3 and 4	2800	2271

2.1.2. Groundwater state

During the inspection of the outcrops they were found to be on a complete dried state without any stain or humidity sign, Figure 39.

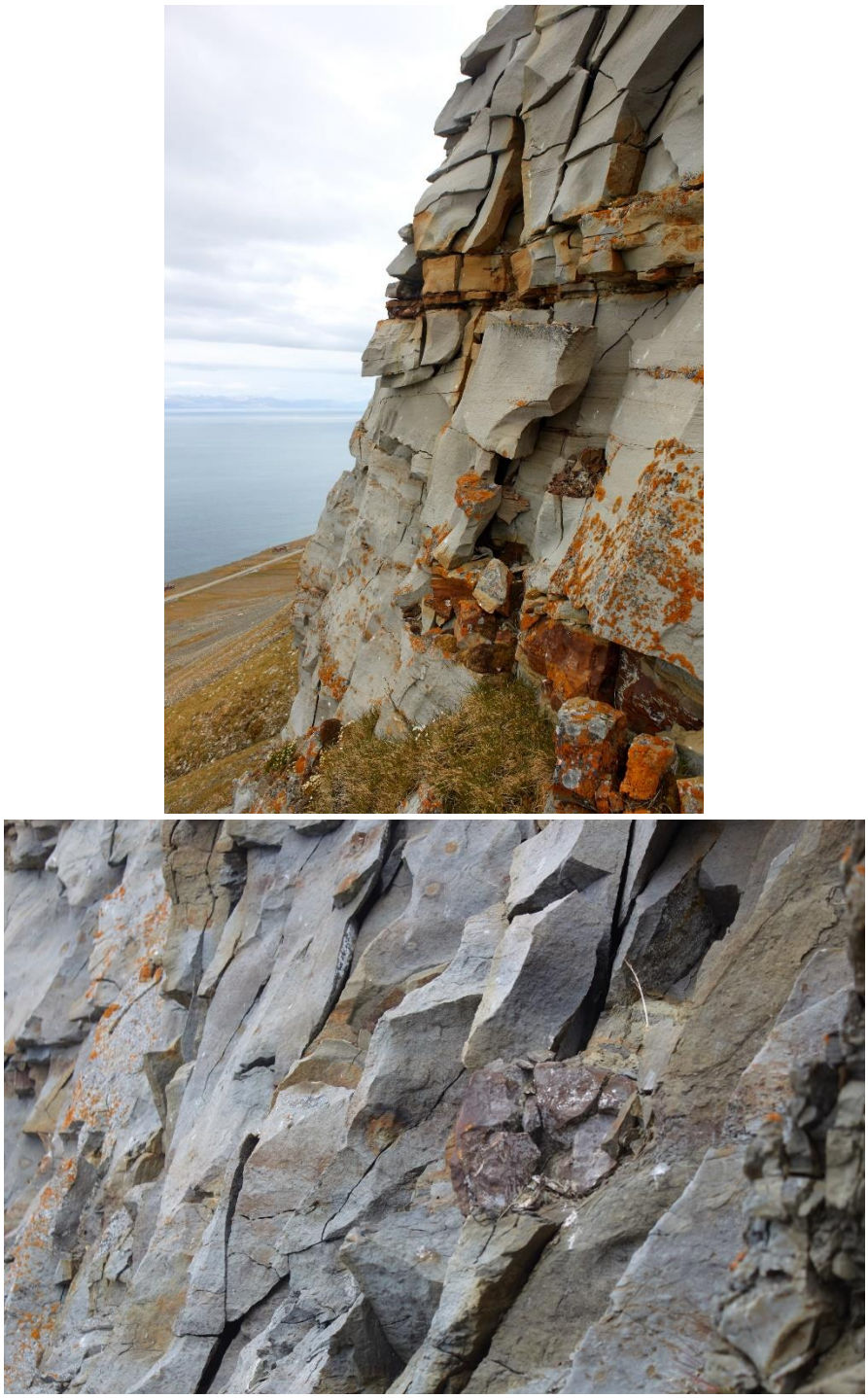

Figure 39 Closeup of the rock outcrops without any water sign

Despite this water could be heard running under the rock debris present at the cones between the rock outcrops which places the phreatic level below the toe of the rock outcrops. This water comes from the melting of the snow and the terrain on the upper levels of the slope, on Figure 40 can be seen the small waterfall that feeds the water stream that was heard.

As seen in Figure 40 the stream is localized at the middle of each one of the recesses at the vertical section, for the ones on the sides only some humidity stains are visible, of the slope which reduces the area exposed to the water action. It can be supposed that the area immediately surrounding the stream could be water saturated meanwhile the rest is dry on the surface but with some degree of water inside the mountain. At the same time the abundance of fractures and the characteristics of the rock favours a high drainage rate which could imply

that at the beginning of the melting season (half may to early June) the whole area can be at a saturated state but quickly reaching dry characteristics.

This is a seasonal state as during winter all the water present is on a frozen state, this will require on a later stage running simulations for summer and winter conditions with different levels for the phreatic line.

Figure 40 Water from melting processes coming down from the gulley

2.2. DTM acquisition

To have data on regarding heights, shapes, and slope angles for the interest area a Digital Terrain Model (DTM) was obtained. This task was performed with a RIEGL VZ1000 laser scanner, Figure 41, from which a point cloud is obtained, this data was processed to obtain a txt file with the coordinates of each point so it could be used into other programs.

Figure 41 Laser scanner employed to obtain the DTM of the slope

The resulted DTM is shown in Figure 42

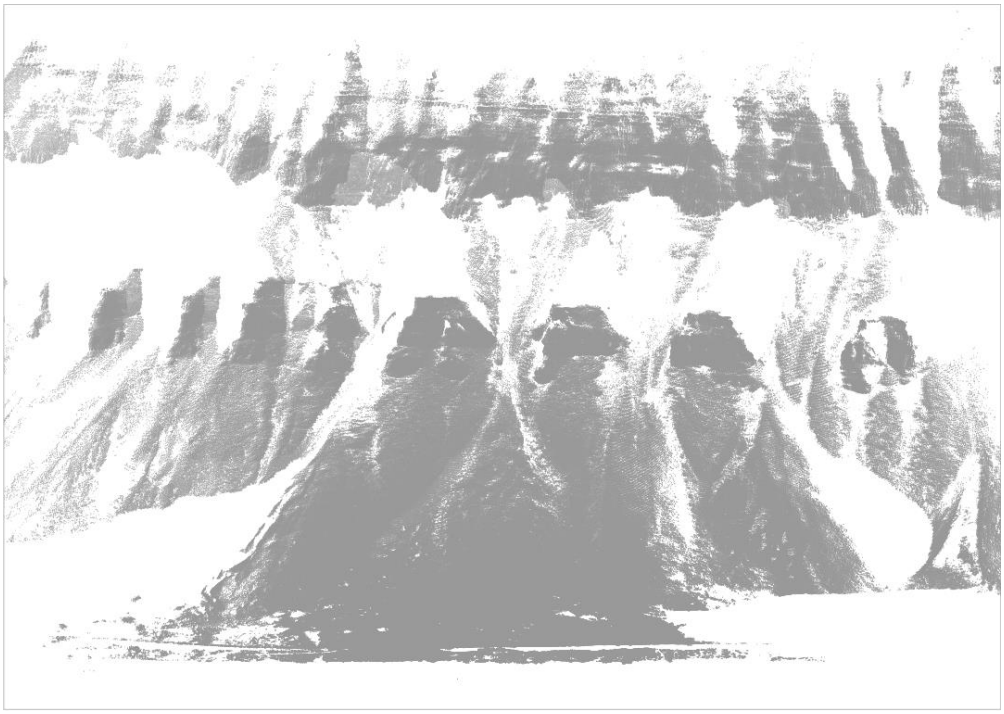

Figure 42 Obtained DTM of the study area

2.3. Obtained rock parameters

The data collected from the field was introduced into RocData, which processes and creates and equivalency between Hoek-Brown and Mohr-Coulomb using the formulas and method explained in 1.8

As a result, the rock of the area is expected to have values around the ones in Table 12

Table 12 Parameters of the rock in the study area

Section	GSI	γ (MN/m³)	Friction angle	Cohesion (MPa)	Intact uniaxial compression strength (MPa)	Uniaxial compression strength (MPa)	Tensile Strength (MPa)	E (MPa)
3	35	0.033	43.37	0.290	41	0.469	0.0091	644.27
4	38	0.028	44.05	0.257	32	0.461	0.0091	598.76
5 centre (between 4 and 5)	36	0.031	47.06	0.243	44	0.544	0.011	731.87
5	36	0.035	38.45	0.496	44	0.544	0.011	731.87
Vertical section	48	0.036	54	0.512	60	2.322	0.051	2888.52

2.4. Stereonet projection analysis

The measured dips and dip directions are presented in Table 13

Table 13 Dip and dip directions

	Dip	Dip direction
Horizontal planes	-10	340
	-8	83
	-10	339
	-9	345
Vertical planes	78	340
	70	145
	80	263
	76	335

This data can be plotted into a stereonet using the program Dips to facilitate its visualization as shown in Figure 43.

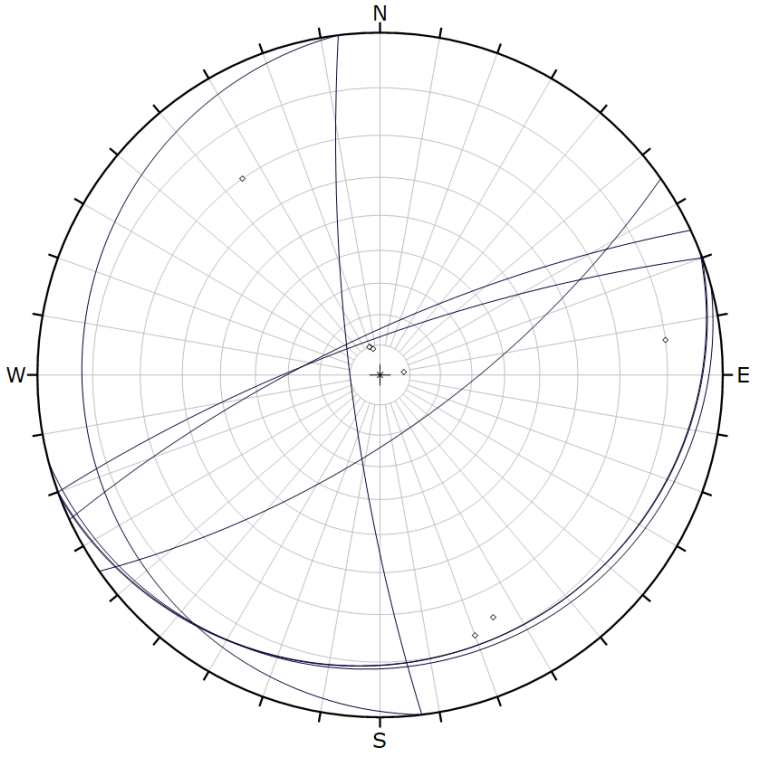

Figure 43 Stereonet projection of collected data

The stereonet gives the ability of performing stability analysis based on the intersections of the different planes, the situation of their poles (a perpendicular line to the plane that passes through the origin) in regard of the slope angle, direction and angle of friction.

The stability analysis has been performed for flexural and direct toppling, see Toppling, as due to the geological nature of the area it is supposed that this are the most probable failure mechanisms.

The problematic angles for the slope direction are between 70 and 350, the slope dip direction of the area sits between 230 to 350 as seen in Figure 44

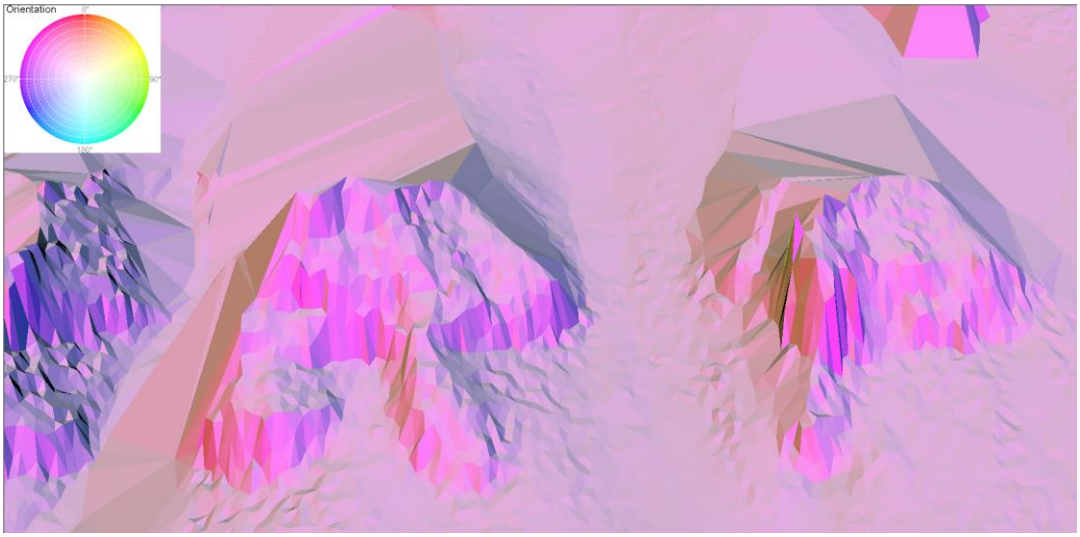

Figure 44 Direction of the slope dipping for areas 3, 4 and 5

2.4.1. Flexural toppling analysis

The first failure mechanism to be analysed was the flexural toppling. Using a slope with a direction of 250º and 76º in inclination the analysis looks as follows, Figure 45. This figure represents a safe case as all the poles from the planes are located outside the risk area (red zone into the stereonet).

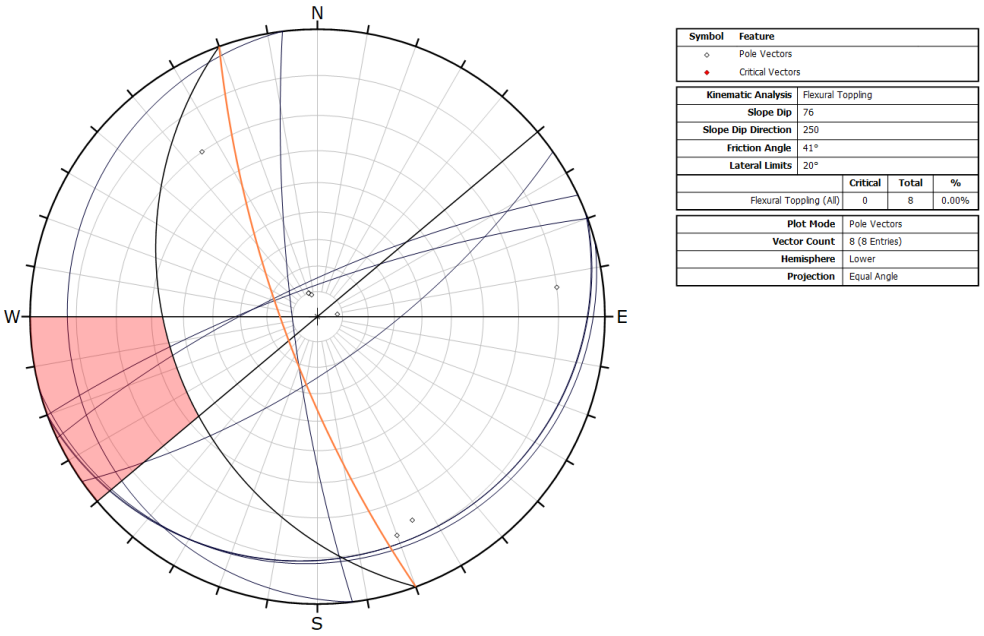

Figure 45 Flexural toppling stability analysis for a slope of 76 º with a direction of 250º

For the studied slopes only the sections which have dip directions between 305 to 345 º make the pole of one of the planes lie into the risk area as shown in Figure 46.

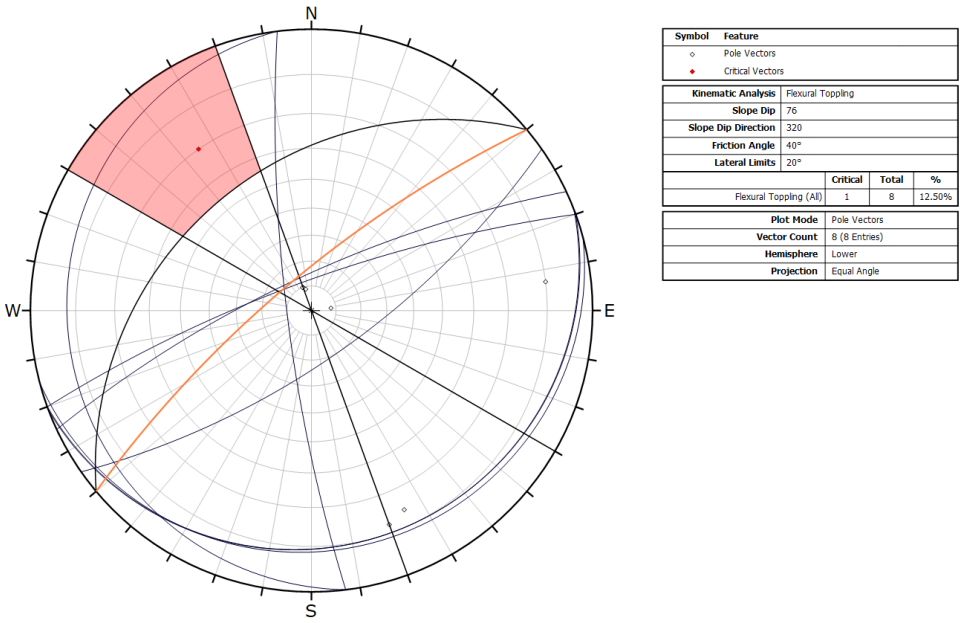

Figure 46 Flexural toppling stability analysis for a slope of 76º with a direction of 320 º

The results shown in the legend represent the probability of flexural toppling failure which is a 12.5 %

2.4.2. Direct toppling

For easiness of comparison the same slopes will be used for the analysis of direct toppling.

The slope with 76 º and direction 250 º is presented on Figure 47

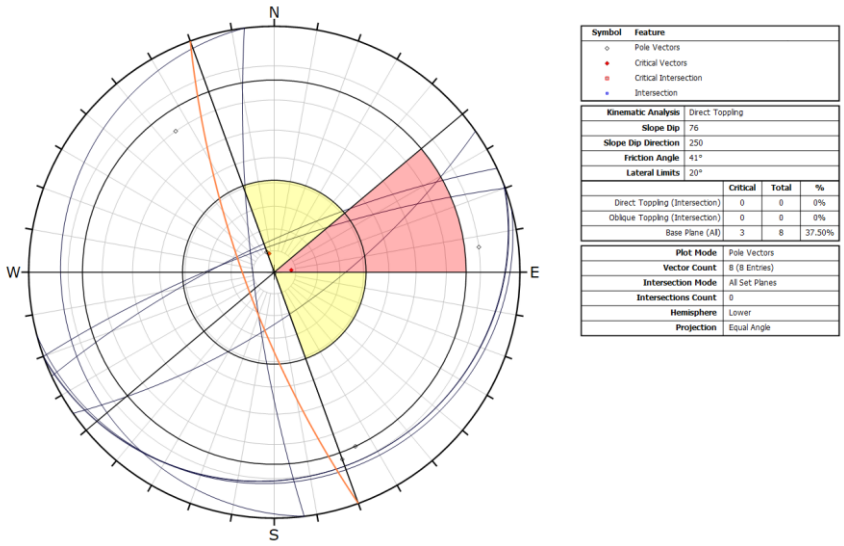

Figure 47 Direct toppling analysis for a 76º 250º slope

In the case of direct toppling the main mechanism is the intersection of a vertical and a horizontal plane as that is how the blocks in risk of falling are formed.

On Figure 47 no intersecting planes are localized inside the problematic areas, highlighted in yellow and red. What is in those are the poles of the drew planes, two poles are in the yellow area and one into the red area. The poles identify areas that could work as release planes for the toppling blocks in case they exist, the difference between them is that poles into the yellow area represent oblique failure as they are outside the side limits. The results of the analysis show a probability of those planes acting as release areas of 37.5 %

At the same time, they are located inside the friction cone which means there is no failure due to sliding.

Continuing with the other case, a slope with dip direction 320 º and dip 76º as shown in Figure 48. In this case one pole is in the yellow area with the same consequences than for the first case. The second pole is into the red area that is outside the friction cone, the friction cone can be found as the external boundary of the yellow area. When a pole its outside the friction cone implies that apart from being a possible release area for toppling failure it also is a sliding plane, meaning that in this case it exists a combined sliding and toppling failure with a probability of failure of 25 %

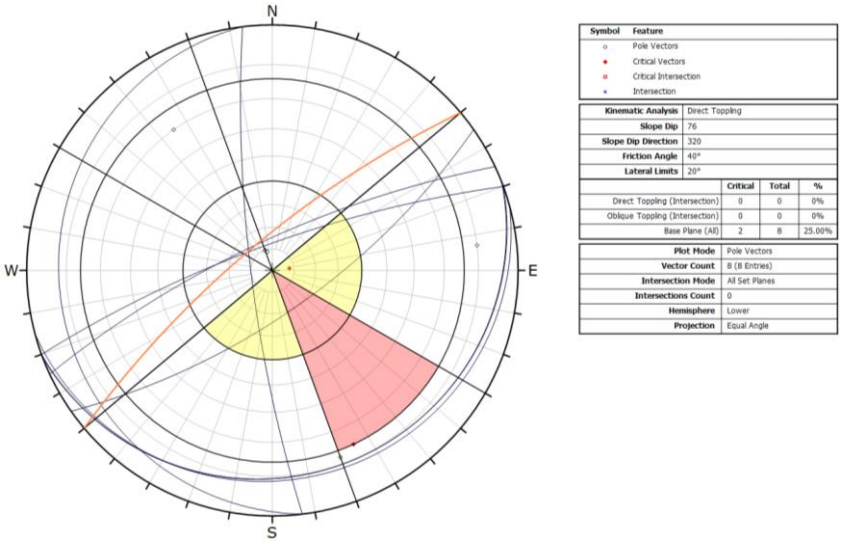

Figure 48 Direct toppling analysis for 76º and 320 º slope

This method of analysis shows that under a toppling case of rock failure, which is the one regarded as the most probable to happen, the slope is considered stable.

While doing this method no groundwater presence had been taken into consideration thus the changes that the soil suffers in bearing capacity, cohesion and friction angles connected with water in the terrain had not been assessed. To overcome this a more detailed analysis will be done in subsequent sections based on simulations via finite element analysis which can provide deeper understanding of the slope behaviour.

3. Slope stability analysis with finite elements

Before assessing the rockfall itself, the trajectories followed by the rocks, their run out points and possible damages the probability of the failure for the slope has to be analysed. The first step is to obtain the properties of the rock and the slope (GSI, density, dipping and slope angles, groundwater state) those values were obtained during the reconnaissance or through the DTM as seen in chapter 2

The areas that had been modelled and simulated were the same that the data acquisition was performed on as they are the sections directly threatening the cabin emplacement.

3.1. Section drawing

The areas were identified in the DTM and visualized with RocPro 3D to simplify the drawing process. In Figure 49 the areas on the DTM are identified for clarification.

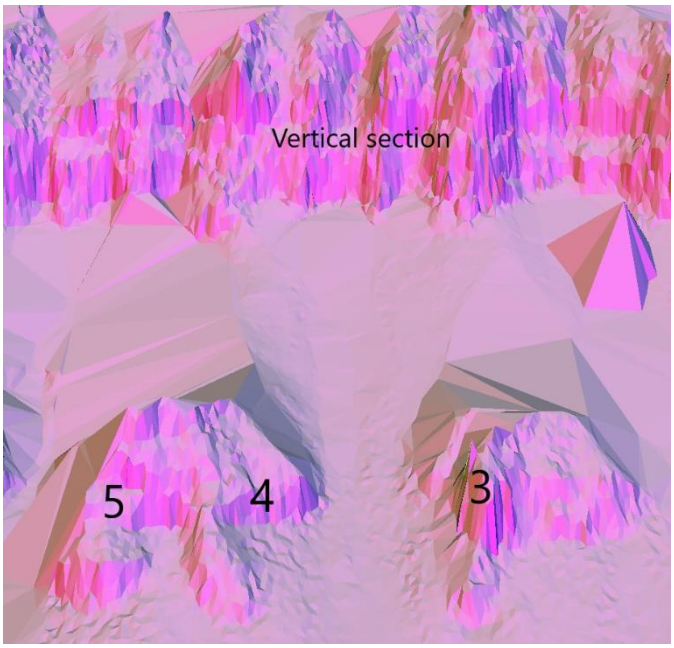

Figure 49 Study areas on the DTM representation

The sections were manually drew in profile perspective as Phase 2 works in 2D, angles and lengths for the different segments that comprises the sections where obtained from the DTM. The sections are presented in Figure 50.

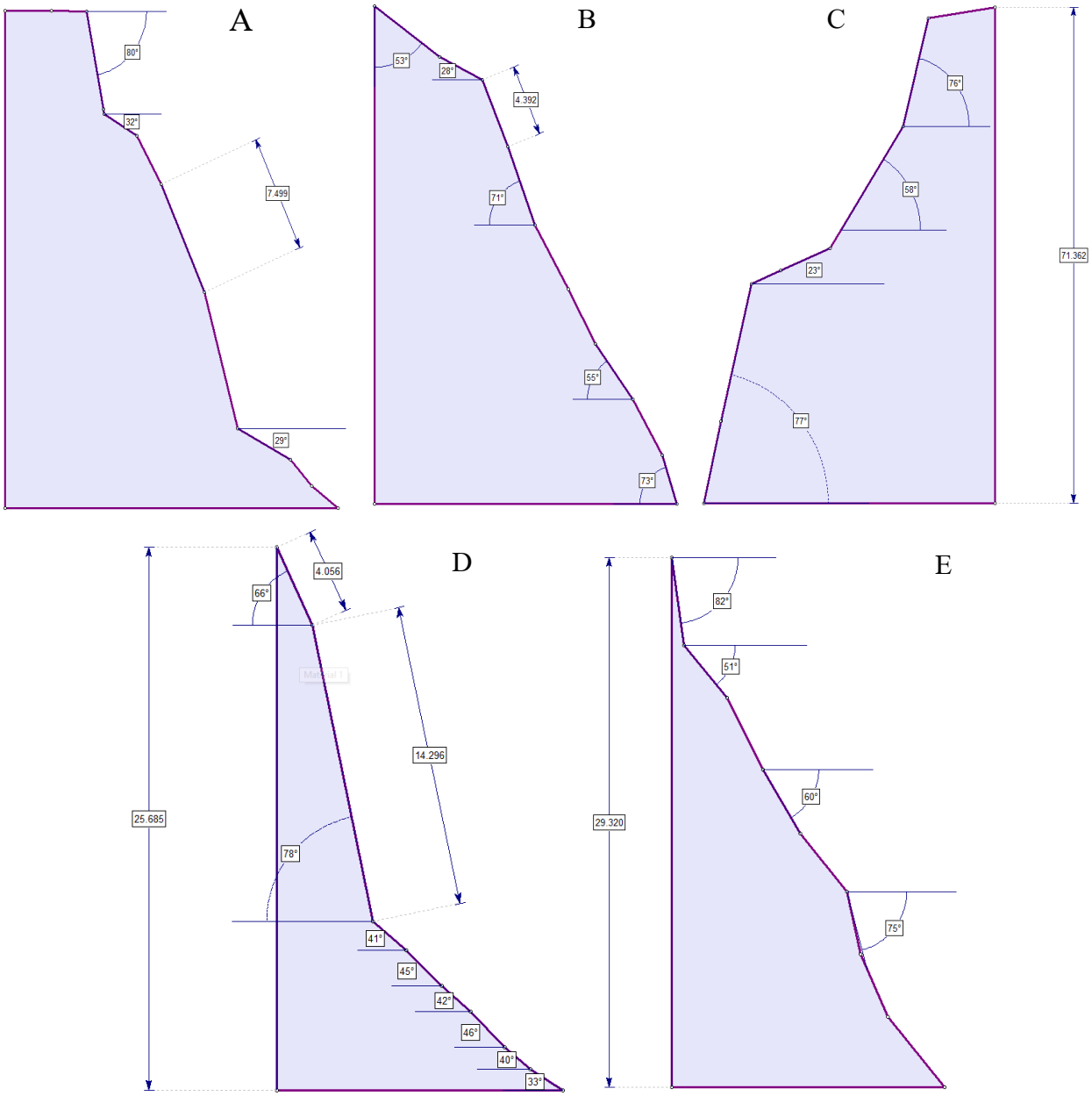

Figure 50 CAD drawings of the studied sections A section 3, B section 4, C section 5, D section 5 centre (between 4 and 5), E vertical section

3.2. Material (soil parameters) and joint generation

The next step was to include material and geological characteristics into the model. The material properties were assigned in accordance with the section being studied as shown in Table 12, introducing statistical variability to compensate for the uncertainties of a material such as natural rock can have being the final parameters for the simulation the ones included in Table 14.

Table 14 Properties for the material 1 and statistical variables

	Property	Mean	Std. Dev.
Section 3	Young's Modulus	644.27	100
	Tensile Strength	0.00917686	0.0005
	Friction Angle (peak)	43.3652	10
	Cohesion (peak)	0.28978	0.1
Section 4	Young's Modulus	628.557	100
	Tensile Strength	0.00895304	0
	Friction Angle (peak)	45.4458	10
	Cohesion (peak)	0.237604	0.1
Section 5 & 5 centre	Young's Modulus	731.87	100
	Tensile Strength	0.0107297	0.005
	Friction Angle (peak)	38.4495	7
	Cohesion (peak)	0.496018	0.1
Vertical section	Young's Modulus	3610.65	500
	Tensile Strength	0.0638892	0.005
	Friction Angle (peak)	55.4098	10
	Cohesion (peak)	0.573228	0.1

The joints and geological discontinuities were modelled as joint networks with a Veneziano method for its generation.

The Veneziano method was chosen as it provides random joint length, orientation and persistence which is considered the best approach for the type of joints observed. The Veneziano method is based on a Poisson line process adapted as seen in (Dershowitz, 1985) to generate joints of finite length. (Rocscience)

The network is generated in two steps:

1. Generating infinite joint lines, each of which passes through a point located according to a Poisson point process (i.e. points distributed in the trace plane according to a uniform distribution). The orientations of the lines may be constant or vary according to some orientation distribution.
2. Dividing each joint line into segments of random lengths. These lengths correspond to a specified statistical distribution. (In the original Veneziano formulation, lengths were assumed to have an exponential distribution. Phase2 relaxes this condition and allows users to specify other statistical distributions.) (Rocscience)

Two networks were defined, one for the set of vertical joints and another one for the set of horizontal ones, the direction of the joint networks was defined with the dip/dip direction method. The joint networks defined for each section are presented in Table 15 to Table 19

Table 15 Characteristics of the joints for section 3

Joint set 1 section 3					
Model	Veneziano				
Inclination	-75.8	Normal distribution	Deviation 5º	Min 14.2	Max 15
Length	4 m	Exponential Distribution	Min 3m	Max 3m	
Persistence	0.5	Normal Distribution	Deviation 0.1	Min 0.3	Max 0.3
Joint intensity	Method joints/area	0.3			
Joint ends	Open at boundary contacts	Surface Excavation			
Joint set 2 section 3					
Model	Veneziano				
Inclination º	9	Normal distribution	Deviation 1	Min 3	Max 3
Length m	1.5	Exponential Distribution	Min 1.4	Max 3m	
Persistence	0.5	Normal Distribution	Deviation 0.1	Min 0.3	Max 0.3
Joint intensity	Method joints/area	0.3			
Joint ends	Open at boundary contacts	Surface Excavation			

Table 16 Characteristics of the joint for section 4

Joint set 1 section 4					
Model	Veneziano				
Inclination º	-69	Normal distribution	Deviation 4	Min 6	Max 6
Length m	2.5	Lognormal Distribution	Deviation 1	Min 1.6	Max 3
Persistence	0.5	Normal Distribution	Deviation 0.1	Min 0.3	Max 0.3
Joint intensity	Method joints/area	0.4			
Joint ends	Open at boundary contacts	Surface Excavation			
Joint set 2 section 4					
Model	Veneziano				
Inclination º	8	Normal distribution	Deviation 2	Min 6	Max 6
Length m	6	Exponential Distribution	Min 3m	Max 3m	
Persistence	0.5	Normal Distribution	Deviation 0.1	Min 0.3	Max 0.3
Joint intensity	Method joints/area	0.25			
Joint ends	Open at boundary contacts	Surface Excavation			

Table 17 Characteristics of the joints for section 5

Joint set 1 section 5 centre					
Model	Veneziano				
Inclination º	-75	Normal distribution	Deviation 4	Min 6	Max 6
Length	0.5	Lognormal Distribution	Deviation 2	Min 0.2	Max 6
Persistence	0.5	Normal Distribution	Deviation 0.1	Min 0.3	Max 0.3
Joint intensity	Method joints/area	1			
Joint ends	Closed				
Joint set 2 section 5 centre					
Model	Veneziano				
Inclination º	10	Normal distribution	Deviation 2	Min 6	Max 6
Length m	0.2	Normal Distribution	Deviation 1	Min 0.1	Max 3
Persistence	0.5	Normal Distribution	Deviation 0.1	Min 0.3	Max 0.3
Joint intensity	Method joints/area	1			
Joint ends	Open at boundary contacts	Surface Excavation			

Table 18 Characteristics of the joints for section 5

Joint set 1 section 5					
Model	Veneziano				
Inclination º	70.15	Normal distribution	Deviation 5	Min 15	Max 15
Length	2	Lognormal Distribution	Deviation 1	Min 1.9	Max 3
Persistence	0.5	Normal Distribution	Deviation 0.1	Min 0.3	Max 0.3
Joint intensity	Method joints/area	0.1			
Joint ends	Open at boundary contacts	Surface Excavation			
Joint set 2 section 5					
Model	Veneziano				
Inclination º	-9	Normal distribution	Deviation 2	Min 6	Max 6
Length m	5	Exponential		Min 3	Max 3
Persistence	0.5	Normal Distribution	Deviation 0.1	Min 0.3	Max 0.3
Joint intensity	Method joints/area	0.2			
Joint ends	Open at boundary contacts	Surface Excavation			

Table 19 Characteristics of the joints for the vertical section

Joint set 1 vertical section					
Model	Veneziano				
Inclination º	82	Normal distribution	Deviation 5	Min 15	Max 8
Length	4	Exponential		Min 3	Max 3
Persistence	0.5	Normal Distribution	Deviation 0.1	Min 0.3	Max 0.3
Joint intensity	Method joints/area	0.3			
Joint ends	Open at boundary contacts	Surface Excavation			
Joint set 2 vertical section					
Model	Veneziano				
Inclination º	10	Normal distribution	Deviation 2	Min 6	Max 6
Length m	4	Exponential		Min 3	Max 3
Persistence	0.5	Normal Distribution	Deviation 0.1	Min 0.3	Max 0.3
Joint intensity	Method joints/area	0.2			
Joint ends	Open at boundary contacts	Surface Excavation			

The sections present the following aspect when the joint networks are applied, Figure 51. On Figure 51 A it can be seen a joint highlighted in green colour, that joint was manually added to model a separated block of rock found in the outcrop, the block in the field can be seen highlighted on the orange rectangle in Figure 52. The joint has an open beginning and a closed end.

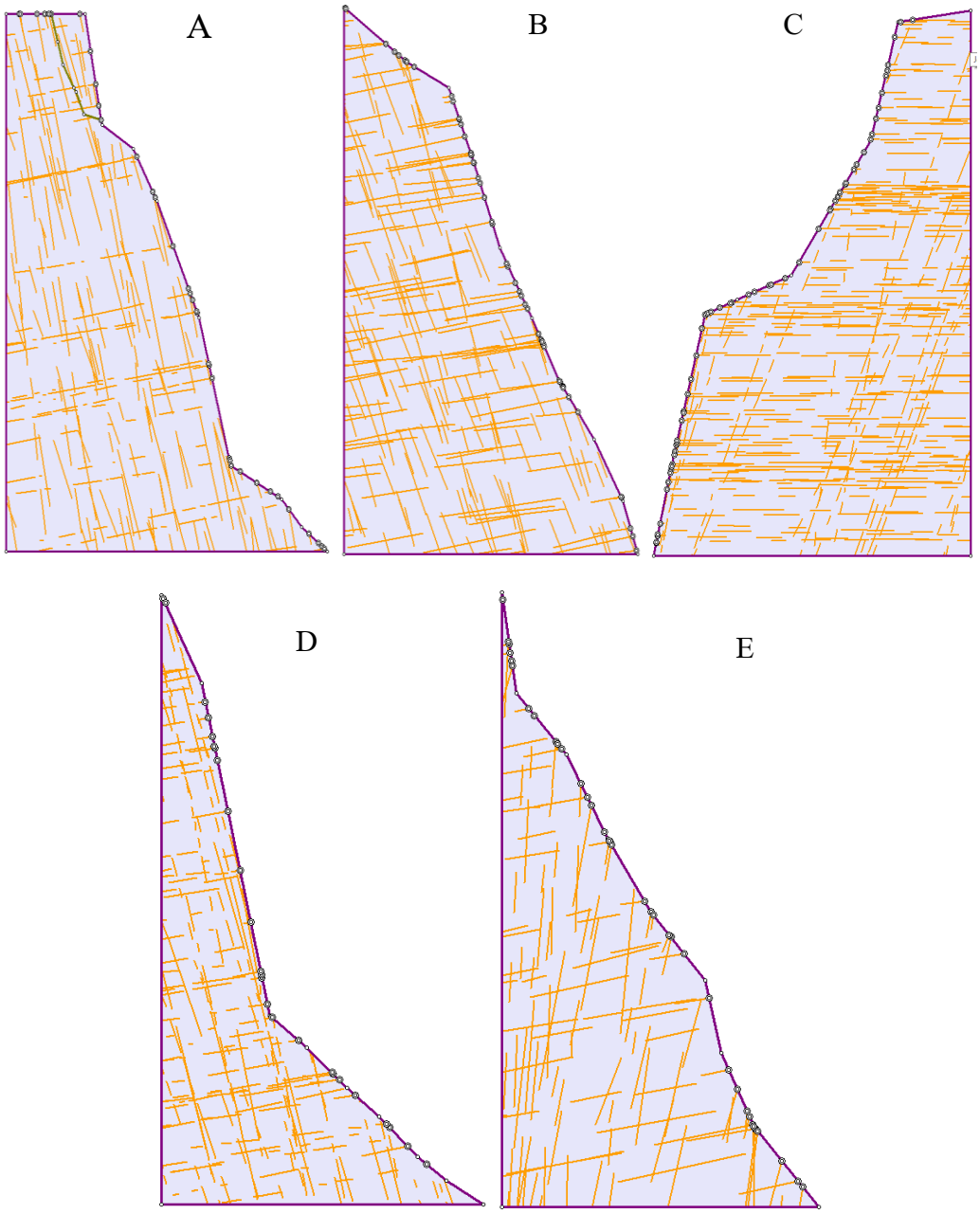

Figure 51 Sections with the joint network applied A section 3, B section 4, C section 5, D section 5 centre (between 4 and 5), E vertical section

Figure 52 Highlight of the modelled block in section 3

3.3. Model meshing

To perform a finite element analysis the models had to be divided into elements which interactions can be calculated, this is known as meshing. The meshing method used is a graded mesh generated using a quadtree nodal insertion technique (Rocscience).

The parameters used for the generation were

- Element type: 6 noded triangles
- Default number of nodes on external: 85 to 90

The number of nodes was selected after trial and error to obtain a reasonable number of elements while keeping the number of bad elements in the mesh at or below 1.5%

In Figure 53 the sections with the meshes applied are presented.

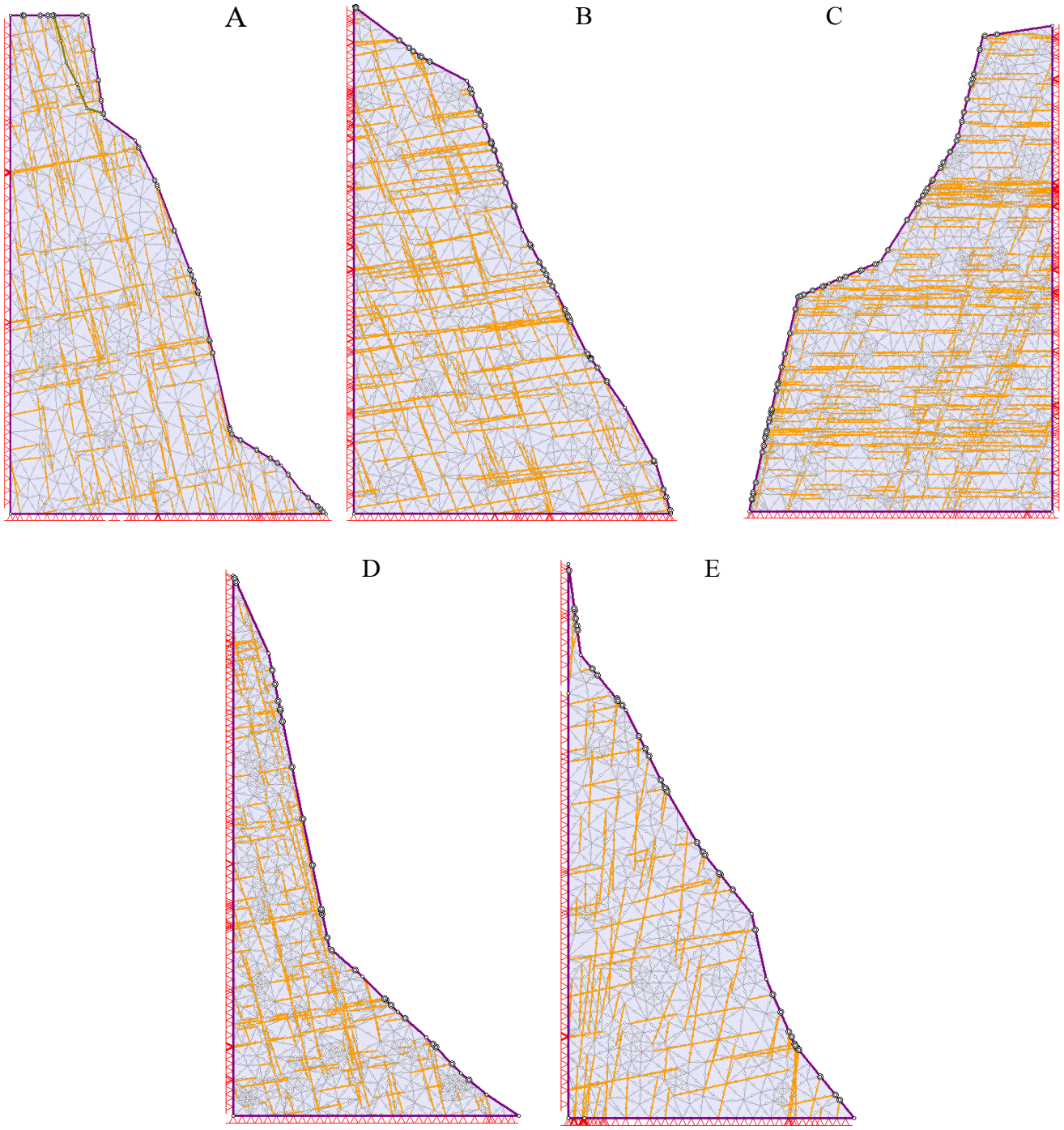

Figure 53 Modelled rock outcrops with applied mesh A section 3, B section 4, C section 5, D section 5 centre (between 4 and 5), E vertical section

3.4.Seismic parameters

Svalbard is situated close to an area of seismic activity as the Atlantic ridge is 200 km away from Longyearbyen, Figure 54.

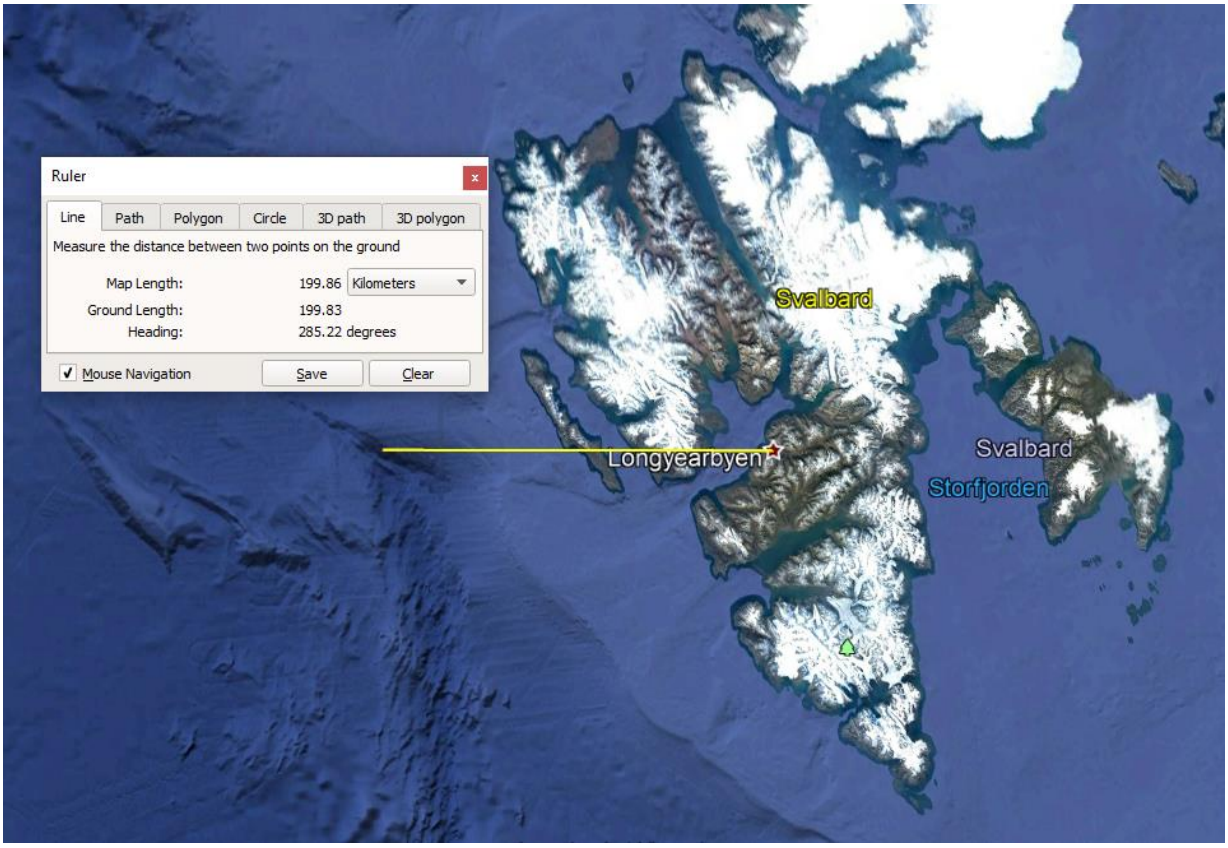

Figure 54 Distance from Longyearbyen (used as reference) to the Atlantic ridge (Landsat/Copernicus, Google Earth)

Using the IRIS earthquake browser data about the earthquakes in the area was obtained, in Figure 55 can be seen the newest 400 earthquakes around the archipelago, denoting a quite high level of activity.

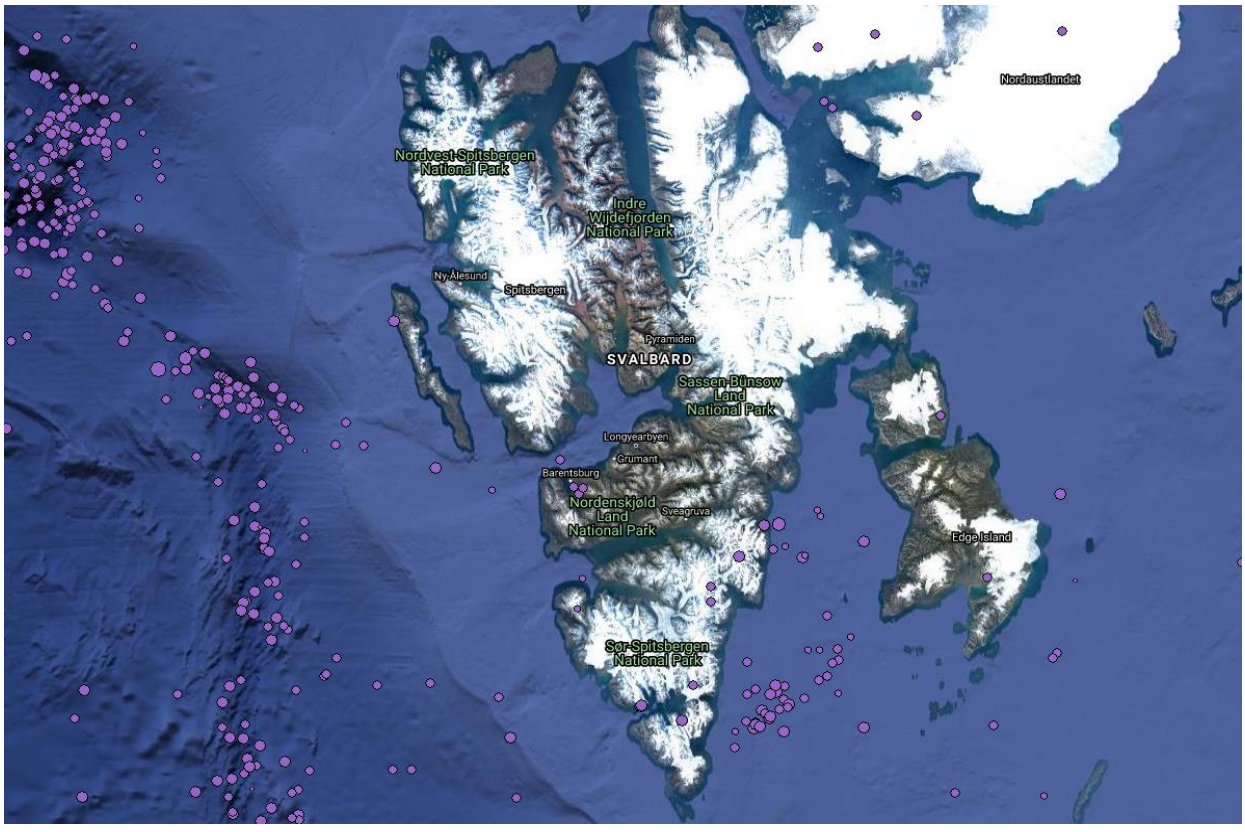

Figure 55 400 newest earthquakes around the Longyearbyen area (Incorporated Research Instiurions for Seismology (IRIS), 2020)

For the simulation purposes only the 3 highest earthquakes recorded since 2010 were selected as the seismometer station accessible records are only for the past 10 years, they are portrayed in Figure 56.

Figure 56 Three largest earthquakes since 2010 (Incorporated Research Instiutrions for Seismology (IRIS), 2020)

The magnitude of these earthquakes and its recorded acceleration is presented in Table 20

Table 20 Earthquake's magnitudes as Mwc

Earthquake	Magnitude (Mwc)	Max amplitude recorded (acceleration) nm/s²	Max amplitude recorded (acceleration) m/s²
02-09-2012	5.2	2 160 362	0.00216362
11-01-2015	5.4	407 771	0.000407771
29-03-2016	5.1	7 771 302	0.007771302

The seismographs were obtained from the Svalbard station that NORSAR has outside Longyearbyen at coordinates 78.18 N 16.37 E shown in Figure 57.

Figure 57 Location of the NORSAR Svalbard station

The seismographs are shown in Figure 58

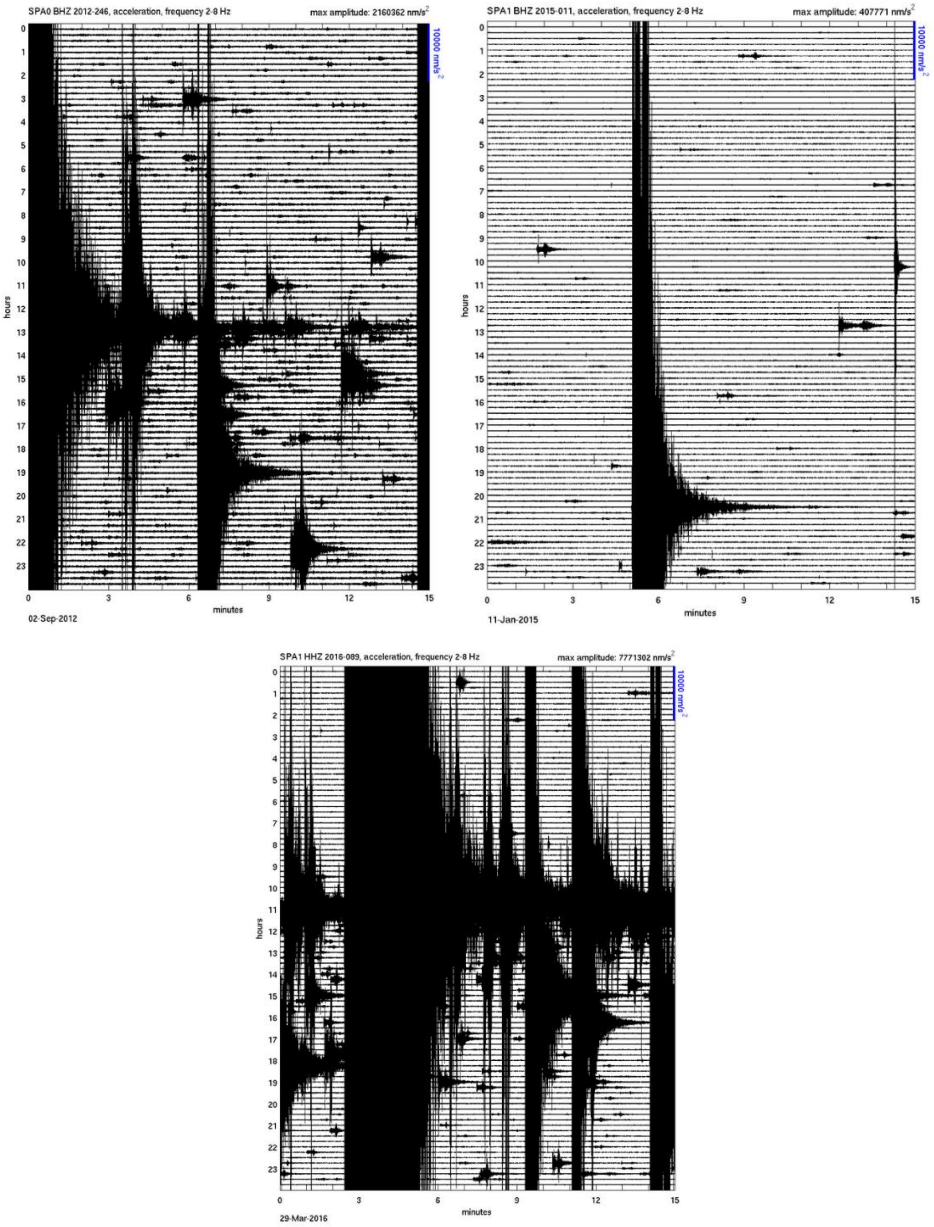

Figure 58 Seismographs for the 3 largest earthquakes since 2010

For its use into phase 2 the acceleration has to be expressed as a fraction of earth's gravity, the conversion is in Table 21.

Table 21 Earthquakes accelerations in relation to earth's g

Earthquake	Max amplitude recorded (acceleration) m/s^2	Relation with earth's gravity acceleration (m/s^2)
12-09-2012	0.00216362	0.000219 g
11-01-2015	0.000407771	0.0000413 g
29-03-2016	0.007771302	0.000787 g

The largest event recorded and used in this project, 29-03-2016, saturated the instruments which caused the low acceleration recorded and thus a bad representation of the event. To overcome this, data from other stations provided by Steve Gibbons from NGI and suggestions from Amir M Kaynia were used. For that specific event, the correct acceleration was 0.02g at 148.2 km of the epicentre, emplacement of the polish seismic station at Hornsund.

These accelerations are quite small, nonetheless this value was used for a stability simulation to assess the situation with real data on the seismic activity. To make the simulations into a more unfavourable scenario the acceleration provided on following simulation was 0.2 times g as suggested in (Rocscience). At the same

time, this approach will cover higher magnitude low probability earthquakes that in the historical series, as there are events of 6 and higher mwc.

Looking at the positions of the epicentres and the accelerations recorded, the 5.1 and 5.2 earthquakes gave higher accelerations than the 5.4 earthquake. The 5.1 and 5.2 events can be linked with an east-west axis with the 5.4 event perpendicular to it. This can indicate a geological feature that facilitates or amplifies seismic waves more on a horizontal component than on a vertical one, this factor will be taken into account during the simulations by stablishing a higher acceleration in the horizontal (0.2) than the vertical (0.1) plane.

3.5.Groundwater

The presence of water in the terrain was stablished using piezometric lines. As observed on the terrain the summer condition simulations will have the piezometric line at the bottom of the section or no line at all if no water was observed. For winter conditions no water is required as it is in a frozen state thus the decrease in material properties associated with its presence are not working.

The diminish in friction angle, cohesion and other parameters were manually adjusted by placing a second material, with the reduced properties below the piezometric line.

The sections look as in Figure 59 for regular (dry) summer or winter conditions, for global warming conditions with an increase in active layer thickness and overall precipitation resulting in an increase in water levels see Figure 60.

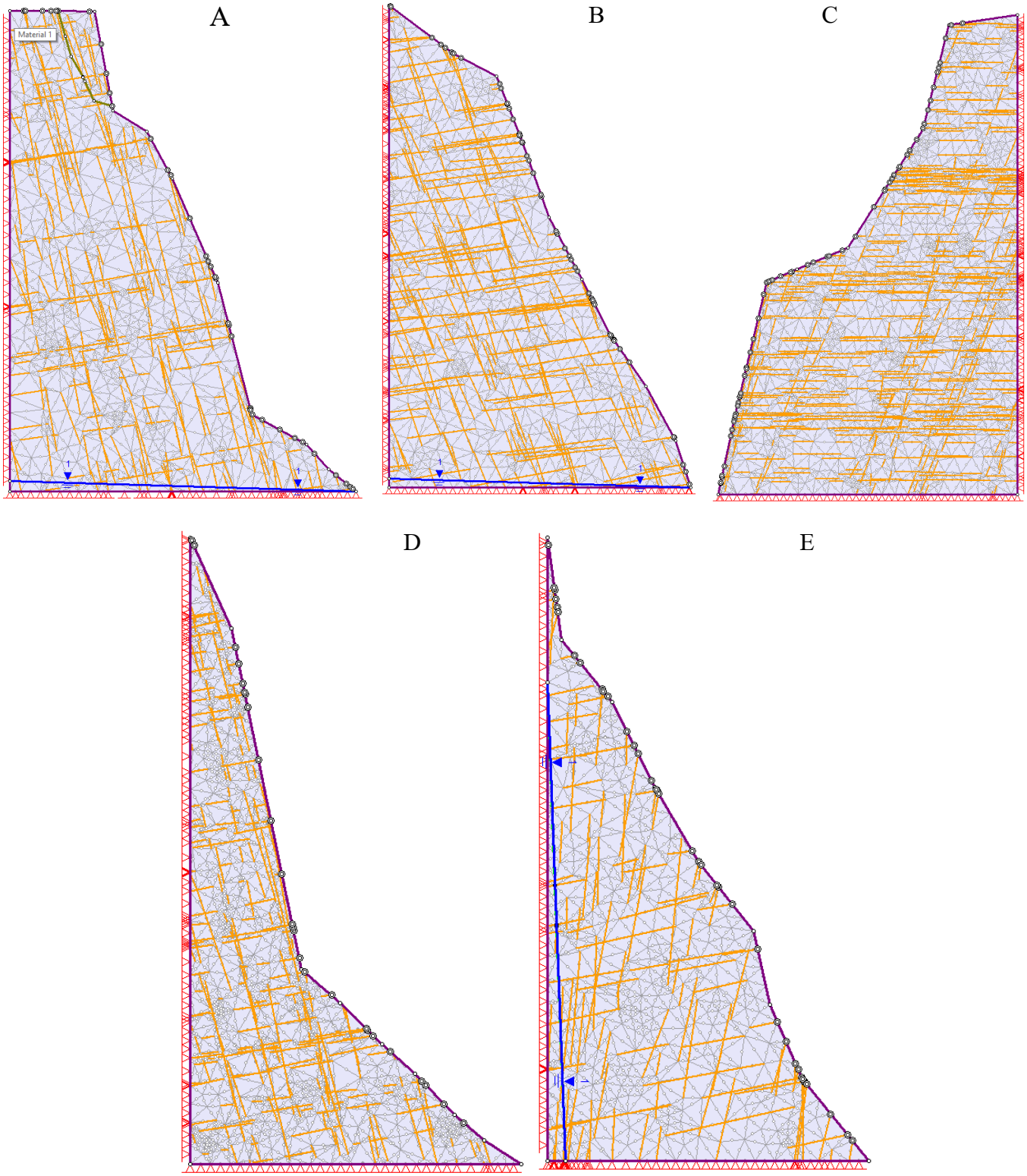

Figure 59 Sections with groundwater applied if necessary A section 3, B section 4, C section 5, D section 5 centre (between 4 and 5), E vertical section

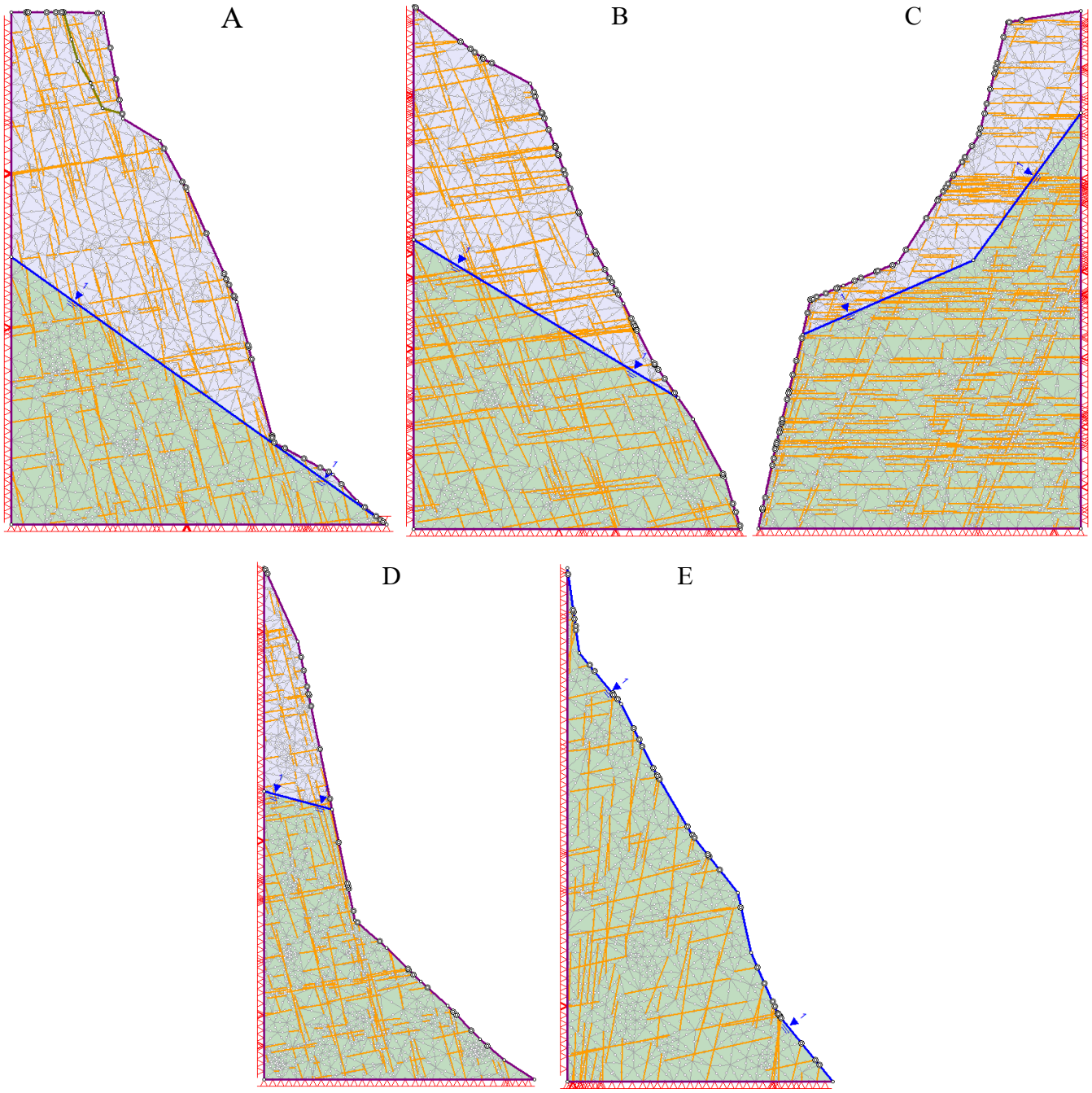

Figure 60 Sections with dry soil in light blue and saturated soil in green for global warming conditions, separated by the piezometric line in blue A section 3, B section 4, C section 5, D section 5 centre (between 4 and 5), E vertical section

3.6. Slope stability simulation results and discussion

The results that are going to be presented from the simulations are:

- Total displacement
- Maximum shear strain
- Critical stress reduction factor and mean stress reduction factor
- Probability of failure (PF)

The critical stress reduction factor (SRF) is the result of the simulation which is done using the mean values of the different variables and is the first one done, while the mean critical SRF is the mean value from the different SRF values calculated for each change to the variables tested during the probabilistic runs of the simulation. SRF represents the safety factor as that is the value that the shear strength of the terrain has to be reduced to become unstable, and the probability of failure which is the probability that the slope reaches at some point an SRF value below 1.

The analysis were done with and without a seismic load applied, to represent regular state, a real seismic load and an unusual seismic load as explained in 3.4

To assess the slope the safety factors proposed by the Norwegian road authority were selected as reference. The safety factors depend on the geological category, consequence and reliability indicators, following indications from Håndbok N200 (Statens Vegvesen, 2018) the slope was categorized as seen in Table 22. Thus, resulting in the safety factors shown in Table 23.

Table 22 Categorisation of the slope

Geotechnical class	3
Consequence class	3
Reliability class	3

Table 23 Safety factors according to Håndbok N200 (Statens Vegvesen, 2018)

Consequence class	Fracture mechanism		
	Thought, dilatant fracture	Neutral fracture	Brittle, contractile fracture
CC3 Most severe	1.4	1.5	1.6

3.6.1. Regular summer/winter simulation results

Stability with real recorded seismic load applied

The first set of simulations was done applying the value of 0.02 g recorded at the Horsund station from the earthquake 29-03-2016 as explained in 3.4, the second one was done with the value of 0.2 g.

Figure 61 shows the maximum shear strain for all the sections with the real seismic load applied. Sections A to C present shear strain that starts on the top back area and descends following a semi-circular path towards the front and base of the outcrop. This could suggest a circular failure instead of the toppling mechanism thought in the first time.

This supposition gains support as the total displacement of the mass shown in Figure 62 also shows a circular shape to it.

The obtained SRF (safety factor) for the sections is shown in Table 24 as said before the critical represents the deterministic solution meanwhile the mean critical represents the probabilistic results.

Table 24 SRF values for the sections under real seismic load

Section	Critical SRF	Mean SRF	σ (std dev)	PF %
3	2.32	2.35	0.6069	1.33
4	2.52	1.43	1.2693	36.86
5	1.78	1.81	0.2885	0.26
5 cent	0.9	0.79	0.6181	63.35
Vert	2.66	2.62	1.5795	15.25

Looking at the SRF only section 5 centre is below the required safety factors of the (Statens Vegvesen, 2018) at the same time this section has vegetation cover that could provide some support which could change the behaviour of the soil. Even if the section complies with the safety factor like section 4 the probability of failure can be quite high, looking at the standard deviation and probability of failure it looks like could be a correlation between high values of σ and high probability of failure (PF) percentages, as the PF represents the likeliness of having a SRF below 1.

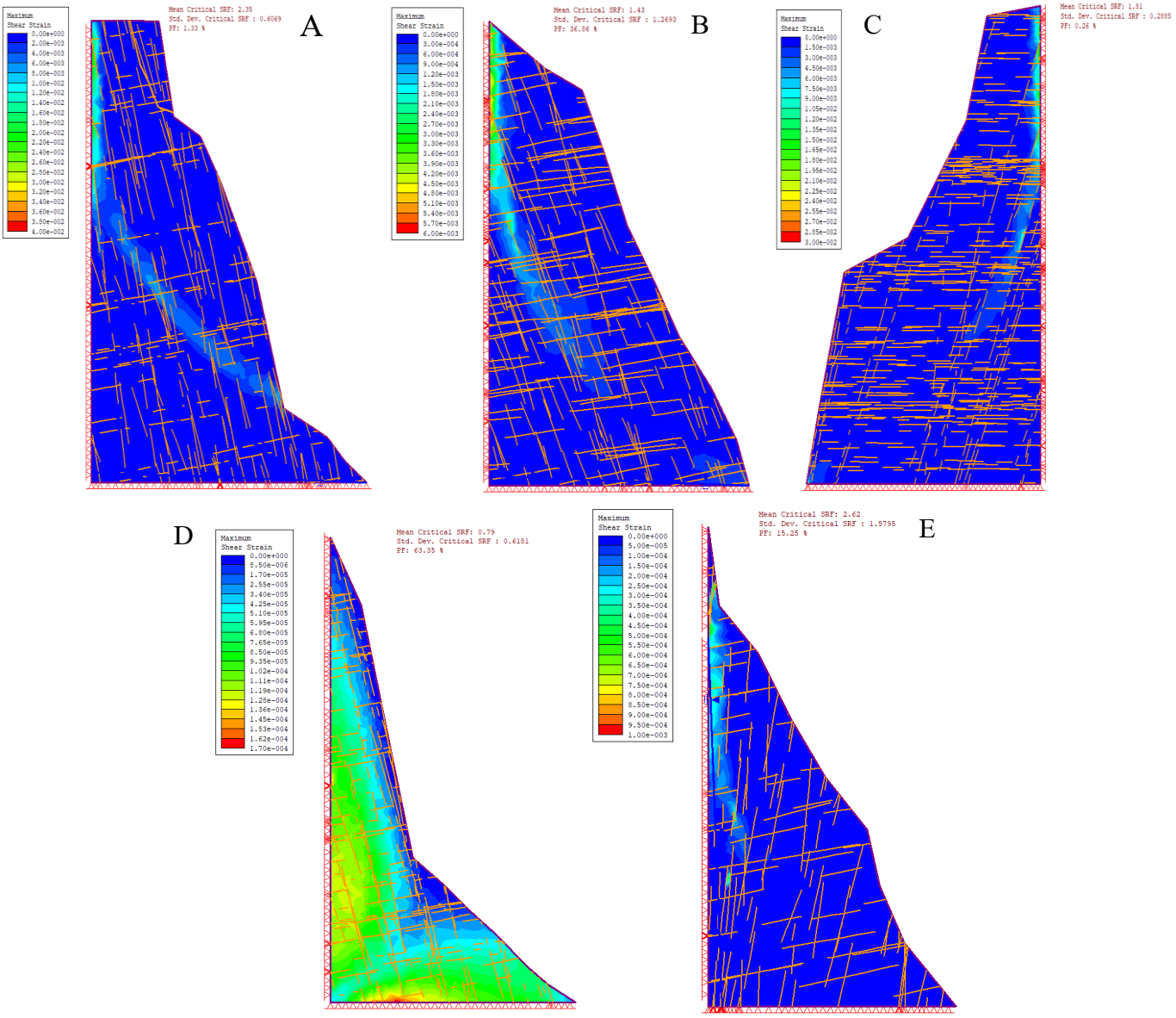

Figure 61 Maximum shear strain for the analysed sections under real seismic load A section 3, B section 4, C section 5, D section 5 centre (between 4 and 5), E vertical section

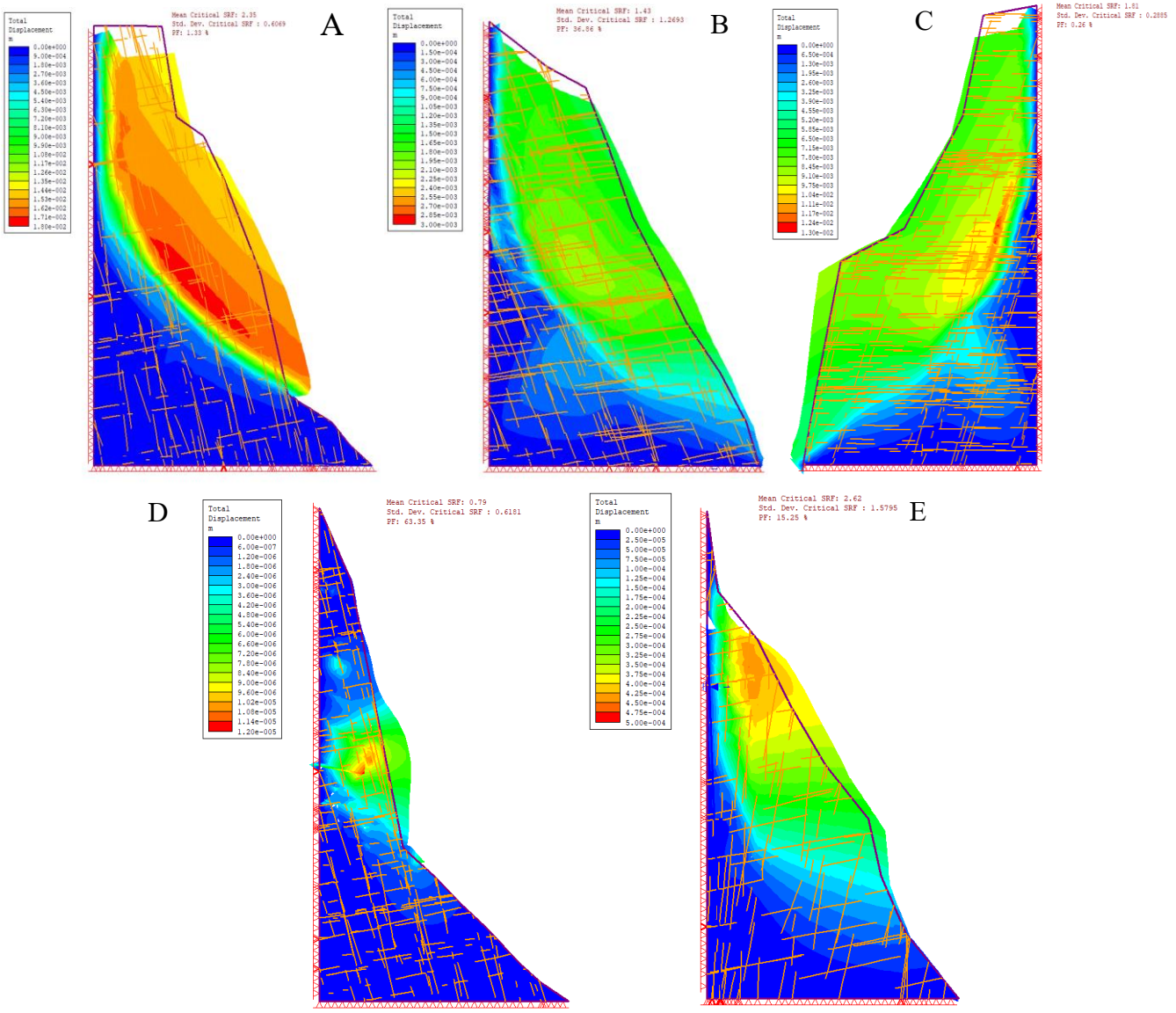

Figure 62 Total displacement for the analysed sections under real seismic load A section 3, B section 4, C section 5, D section 5 centre (between 4 and 5), E vertical section

Stability with improbable seismic load applied

Figure 63 shows the maximum shear strain for all the sections with the improbable seismic case applied.

Sections A to D present shear strain located on the top area with most of it into the wall side of the section, with B and C showing some strain located into more central points. The vertical section is the only one that presents strain over the whole mass of rock. This pattern is different when compared to the more circular one shown in the real earthquake scenario.

Comparing the improbable earthquake case with the real recorded one, all the sections, except 4, present SRF that do not comply with the ones from (Statens Vegvesen, 2018) at the same time in this scenario the values of σ are lower than those for the real seismic event, and the apparent correlation between σ and PF is not there. But in both cases section 4 and the vertical section are the ones that present a higher value of σ. The values are shown in Table 25.

Table 25 SRF values for the sections under improbable seismic load

Section	Critical SRF	Mean SRF	σ (std dev)	PF %
30	0.89	0.84	0.1023	94.6
4	1.93	1.52	0.6046	19.39
5	0.18	0.12	0.1297	100
5 cent	0.23	0.2	0.1158	100
Vert	0.64	0.52	0.2116	98.78

The displacement of the mass also presents slight differences to the one with the real seismic event, especially on section 3 with a less circular shaped failure on the improbable event than on the real one

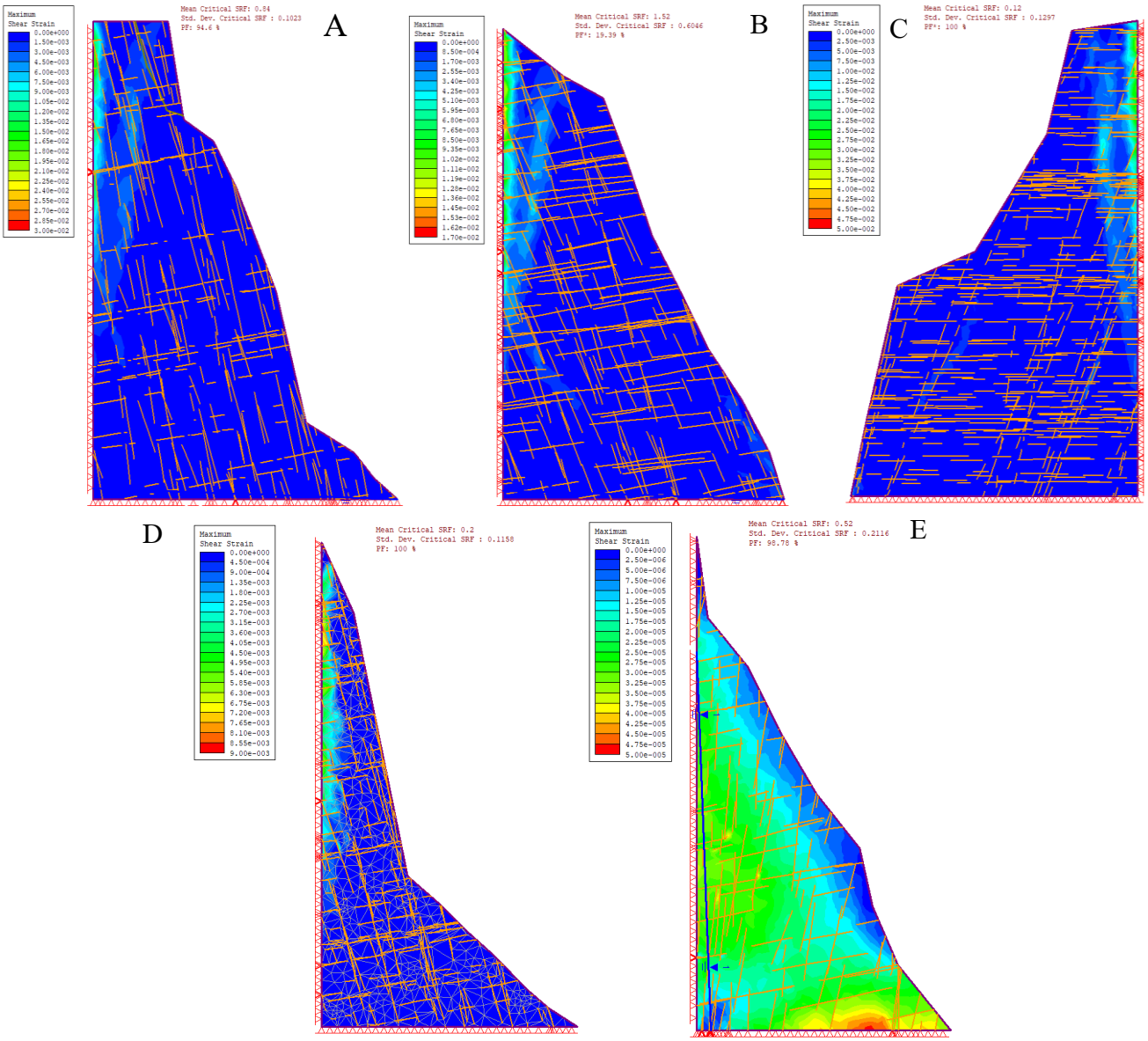

Figure 63 Maximum shear strain for the simulated sections during regular summer conditions with improbable seismic load applied A section 3, B section 4, C section 5, D section 5 centre (between 4 and 5), E vertical section

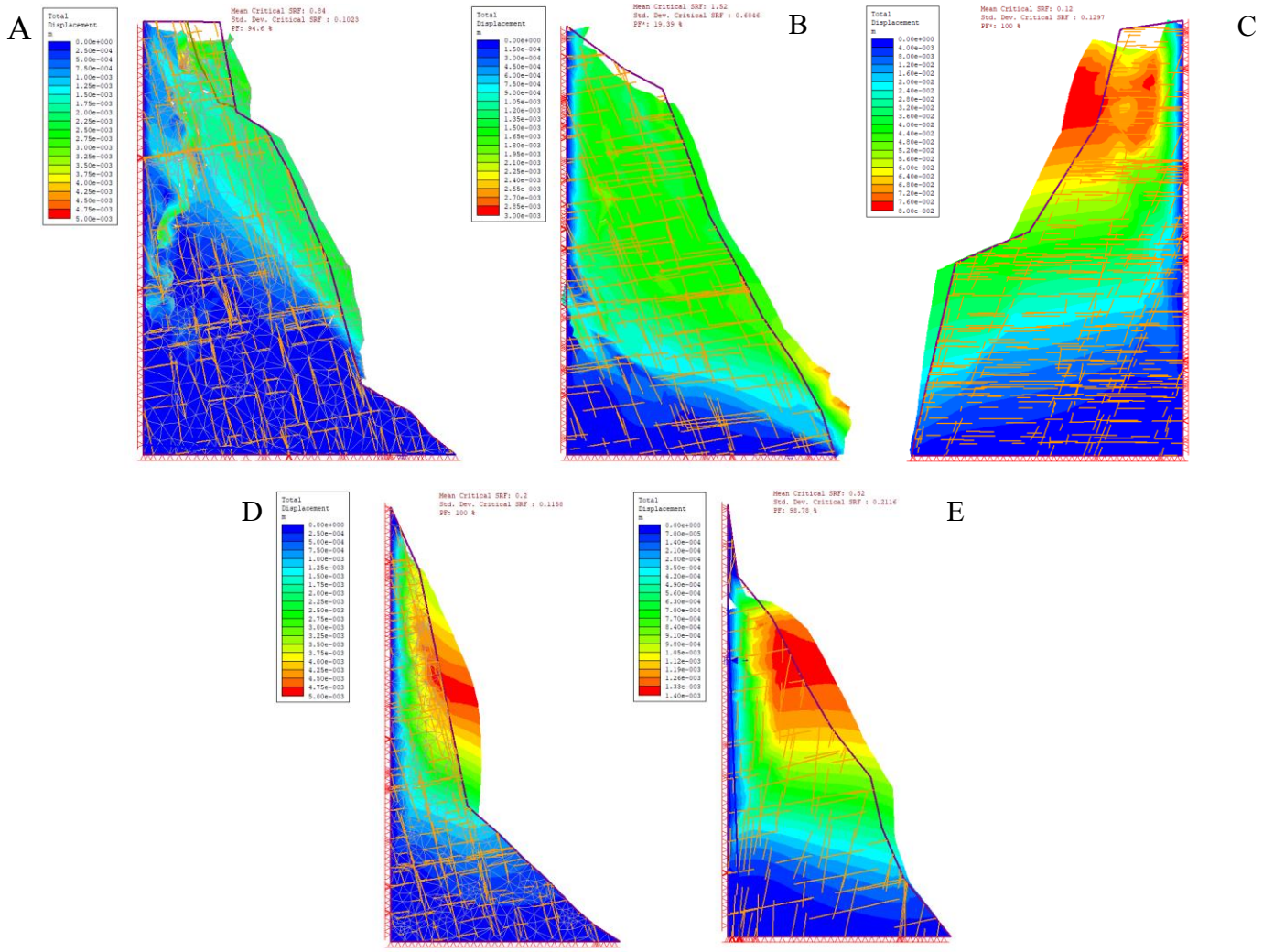

Figure 64 Total displacement for the simulated sections during regular summer conditions with improbable seismic load applied A section 3, B section 4, C section 5, D section 5 centre (between 4 and 5), E vertical section

Stability for regular conditions

For the regular conditions, the same procedure as with the seismic loading was followed. Figure 65 presents the sections maximum shear strength with no seismic loading.

The shear strain presents a similar pattern as when the seismic loading is applied, starts on the top back area, and descends following a semi-circular path. In this case it is worth noting that D and E present shearing in almost all the rock mass meanwhile for the case with seismic effect it varied. If it was with the real earthquake acceleration, D was the section with shearing on the whole mass meanwhile with the improbable earthquake, E was the section that presented this behaviour.

Under normal conditions only one of the analysed sections, 5 centre, present safety factors, see Table 26, below the ones considered in (Statens Vegvesen, 2018).

Table 26 SRF values for the sections under normal conditions

Section	Critical SRF	Mean SRF	σ (std dev)	PF %
3	2.4	2.43	0.6222	1.09
4	2.62	1.51	1.2783	34.47
5	1.85	1.82	0.4081	2.22
5 cent	1.21	1.02	0.8216	48.93
Vert	1.68	2.25	2.0695	27.24

The studied sections can be considered stable in almost any of the conditions present actually in the terrain. Regarding the section with the lowest SRF across both cases, 5 cent, this area was found to present abundant vegetation that could have a stabilization effect that had not been accounted for in these simulations.

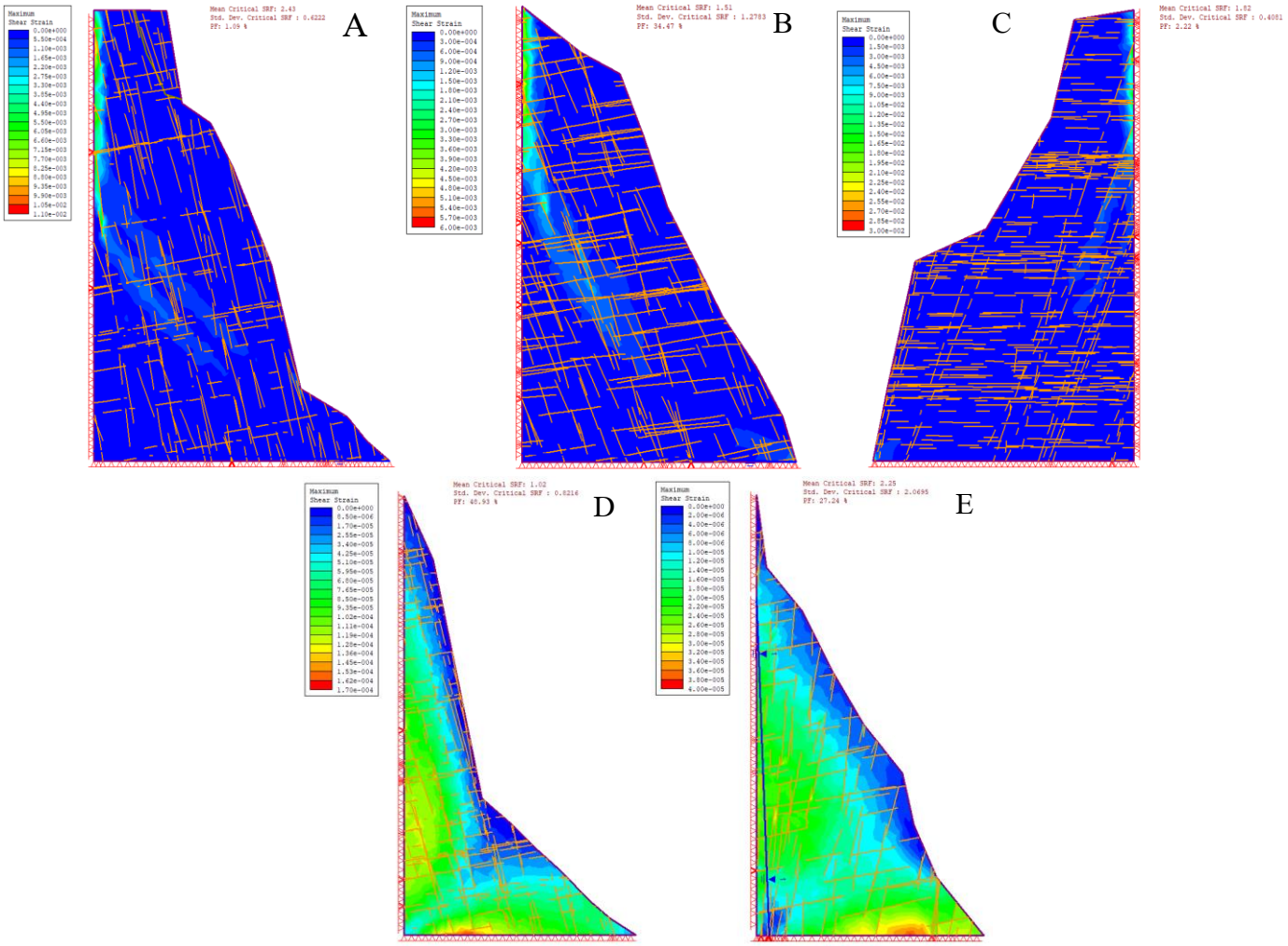

Figure 65 Maximum shear strain for the simulated sections during regular summer conditions without seismic load applied A section 3, B section 4, C section 5, D section 5 centre (between 4 and 5), E vertical section

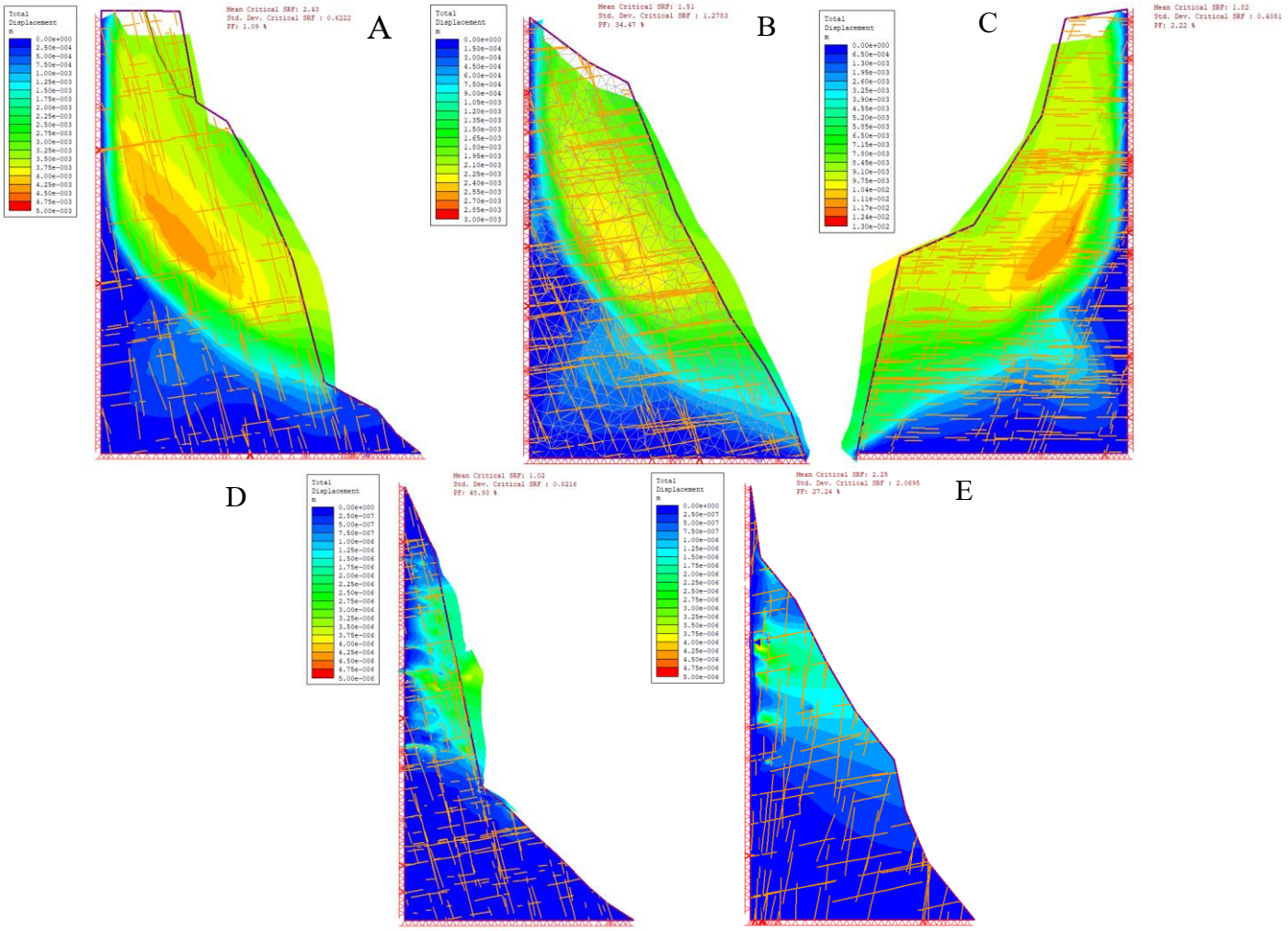

Figure 66 Total displacement for the simulated sections during regular summer conditions without seismic load applied A section 3, B section 4, C section 5, D section 5 centre (between 4 and 5), E vertical section

3.6.2. Simulation results with increased groundwater presence due to global warming effects

In the expected future scenario of increasing warmer temperatures, the active layer thickness will increase, therefore the amount of water released during the melting season will have a higher impact on the bearing properties of the terrain. At the same time on a major scale this scenario predicts an increase of precipitation which will also increase the amount of water present not derived from permafrost related processes.

The simulations presented here were done with high piezometric levels to account for this increase and as a result a higher area of terrain with decreased strength values compared with its drained (dry) situation.

The parameters to model the saturated terrain conditions were obtained from (Bo, et al., 2020) for sandstones, following the same procedure as in 2.3. After the saturated terrain parameters were obtained they were introduced as a new material that is located below the piezometric line as shown in Figure 60. The same approach was used for all the sections.

The parameters for material 2, which is the saturated one, are presented in Table 27. This parameters were obtained on a similar way as for material one explained in 3.2 using values from (Bo, et al., 2020) when necessary.

In a similar way as 3.6.1 the simulations were done with both types of seismic loads and without for normal conditions.

Table 27 Parameters for saturated conditions

	Property	Mean	Std. Dev.
Section 3	Young's Modulus	338.59	50
	Tensile Strength	0.00589654	0.001
	Friction Angle (peak)	32.6237	5
	Cohesion (peak)	0.345243	0.1
Section 4	Young's Modulus	315.96	100
	Tensile Strength	0.00370949	0.001
	Friction Angle (peak)	34.5524	2
	Cohesion (peak)	0.143439	0.02
Section 5 & 5 centre	Young's Modulus	406.83	100
	Tensile Strength	0.00540345	0.001
	Friction Angle (peak)	33.3611	2
	Cohesion (peak)	0.392426	0.1
Vertical section	Young's Modulus	3610.65	500
	Tensile Strength	0.0638892	0.005
	Friction Angle (peak)	55.4098	10
	Cohesion (peak)	0.573228	0.1

Stability with real recorded seismic load applied

As in previous simulations the strain on the analysed sections, Figure 67, present a circular shape pattern that start on the top back and descends across the middle part of the section. Also D and E present strain on the whole section which is a similar behaviour as the one observed for regular summer conditions, but differs from the same seismic load but in regular conditions as in that case only D had strain on the whole rock mass.

Under a warmer environment but under the action of the recorded seismic event conditions 4 out of the 5 sections present safety factors below the ones considered in (Statens Vegvesen, 2018). This presents a high risk scenario as a raise in temperatures is already an ongoing process while at the same time the seismic event employed in this case is quite a moderate and frequent one, resulting in both of the conditions for a destabilization a the following rockfall event to take place.

Table 28 SRF values for the sections in warmer scenario with real seismic load applied

Section	Critical SRF	Mean SRF	σ (std dev)	PF %
3	2.07	2.0.1	0.2903	0.03
4	1.58	1.26	0.5785	32.58
5	0.01	0.04	0.0181	100
5 cent	0.07	0.06	0.0123	100
Vert	0.27	0.21	0.0497	100

Regarding the displacement of the rock mass Figure 68 it presents a mixture of failure modes, with A and B looking more like circular failure with C and E more like toppling.

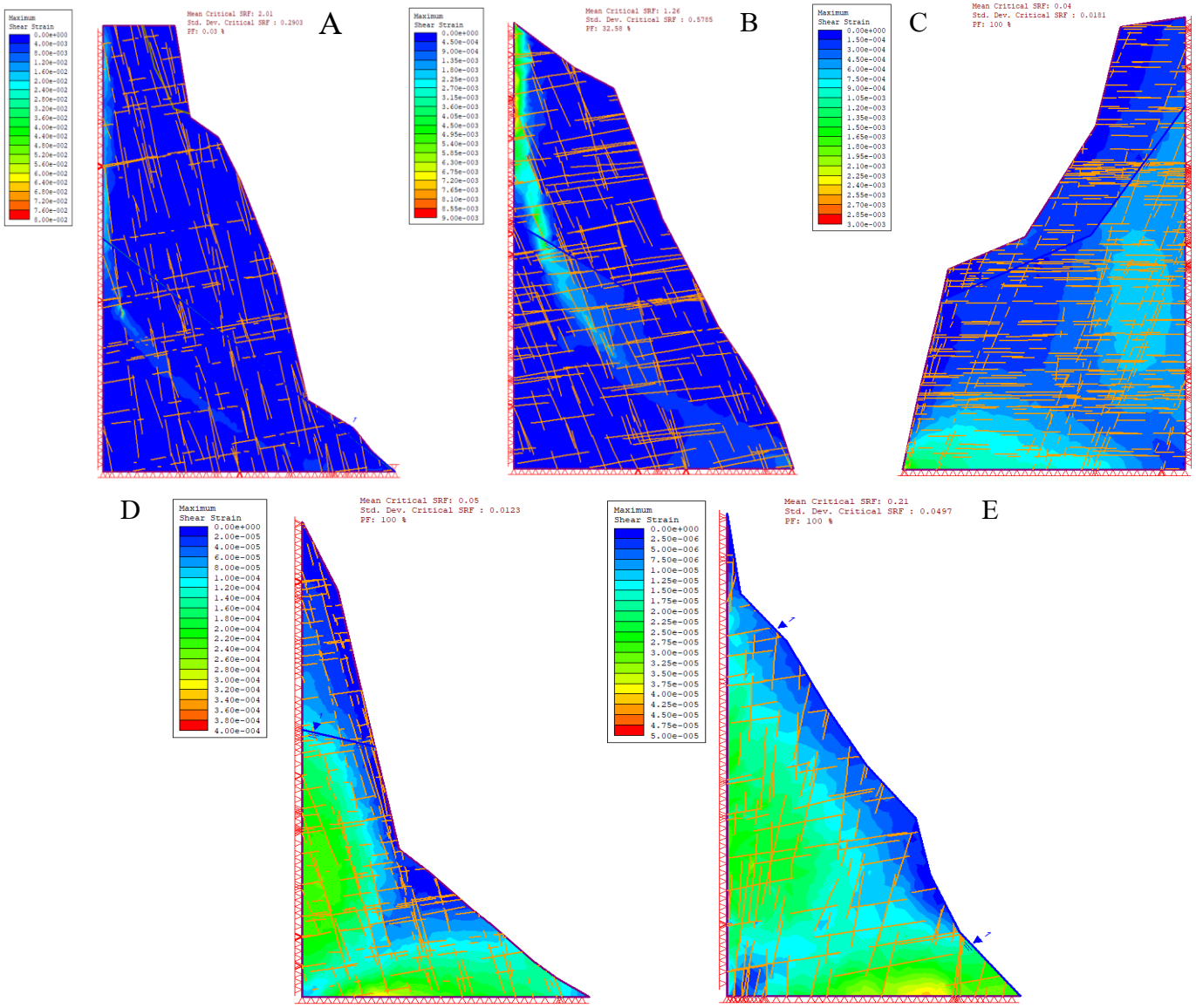

Figure 67 Maximum shear strain for the simulated sections during warmer conditions with real seismic load applied A section 3, B section 4, C section 5, D section 5 centre (between 4 and 5), E vertical section

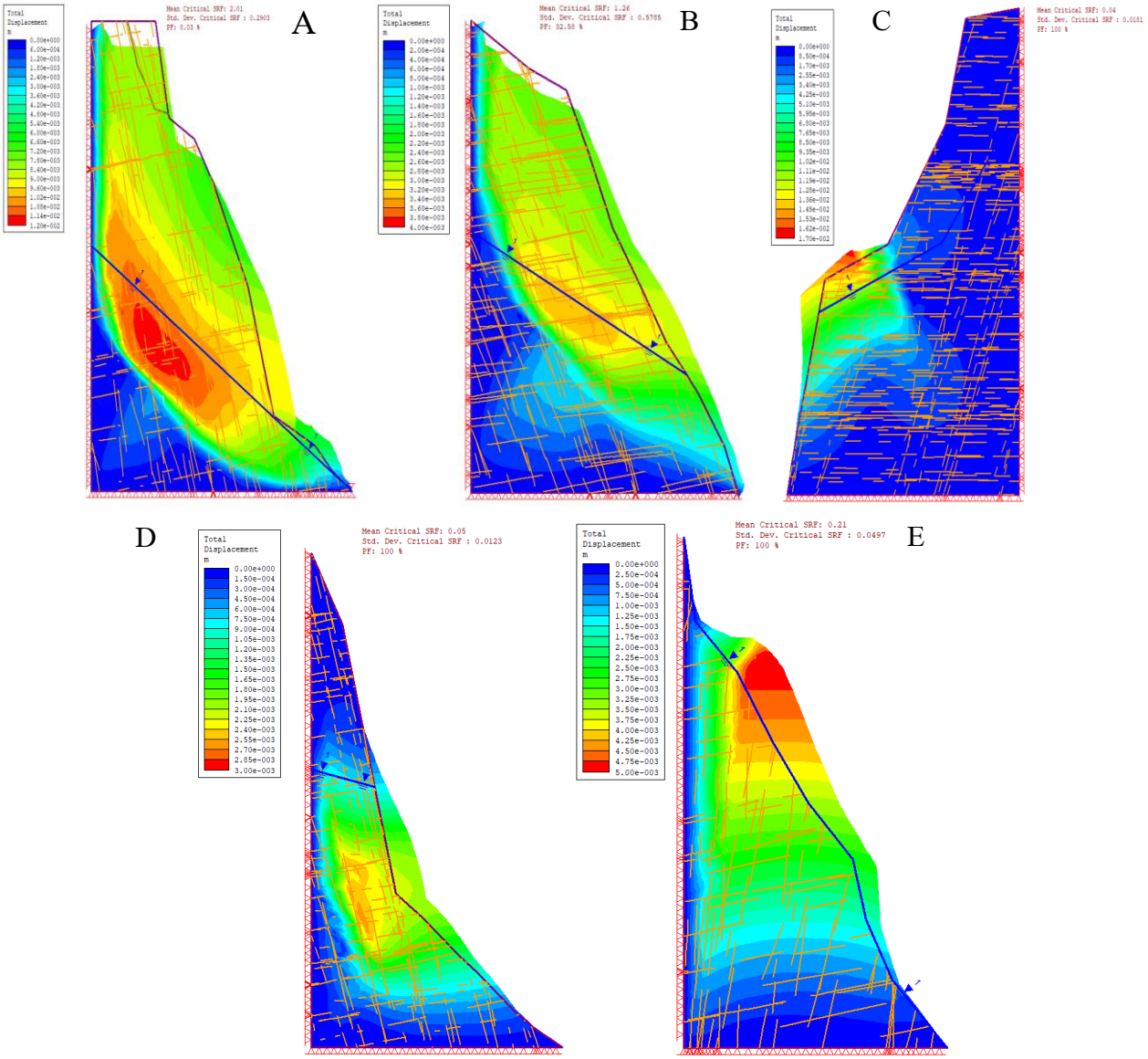

Figure 68 Total displacement for the simulated sections during warmer conditions with real seismic load applied A section 3, B section 4, C section 5, D section 5 centre (between 4 and 5), E vertical section

Stability with improbable seismic load applied

Checking the strain distribution shown in Figure 69, on A and B the circular pattern shown in the actual temperatures scenario has been changed for a vertical one tilted toward the front of the section, C presents higher strain levels on the saturated terrain which is expected due to the change in the properties of the material. D and E show similar behaviours as in previous instalments.

Regarding the displacement of the rock mass, this scenario shows more toppling like behaviour than previous cases, it can be appreciated in Figure 70 A, C and D how the mass move forward on a more blocky appearance than as a whole mass moving, B keeps the circular shape shown in previous iterations.

As in previous instances this type of seismic event means an absolute loss of stability on all the studied sections with SRF values close to cero in some cases.

Table 29 SRF values for the sections under warmer temperatures and improbable seismic load

Section	Critical SRF	Mean SRF	σ (std dev)	PF %
3	0.63	0.75	0.1336	97.02
4	1.22	0.83	0.4843	63.42
5	0.01	0.01	0.0032	100
5 cent	0.05	0.04	0.011	100
Vert	0.2	0.19	0.026	100

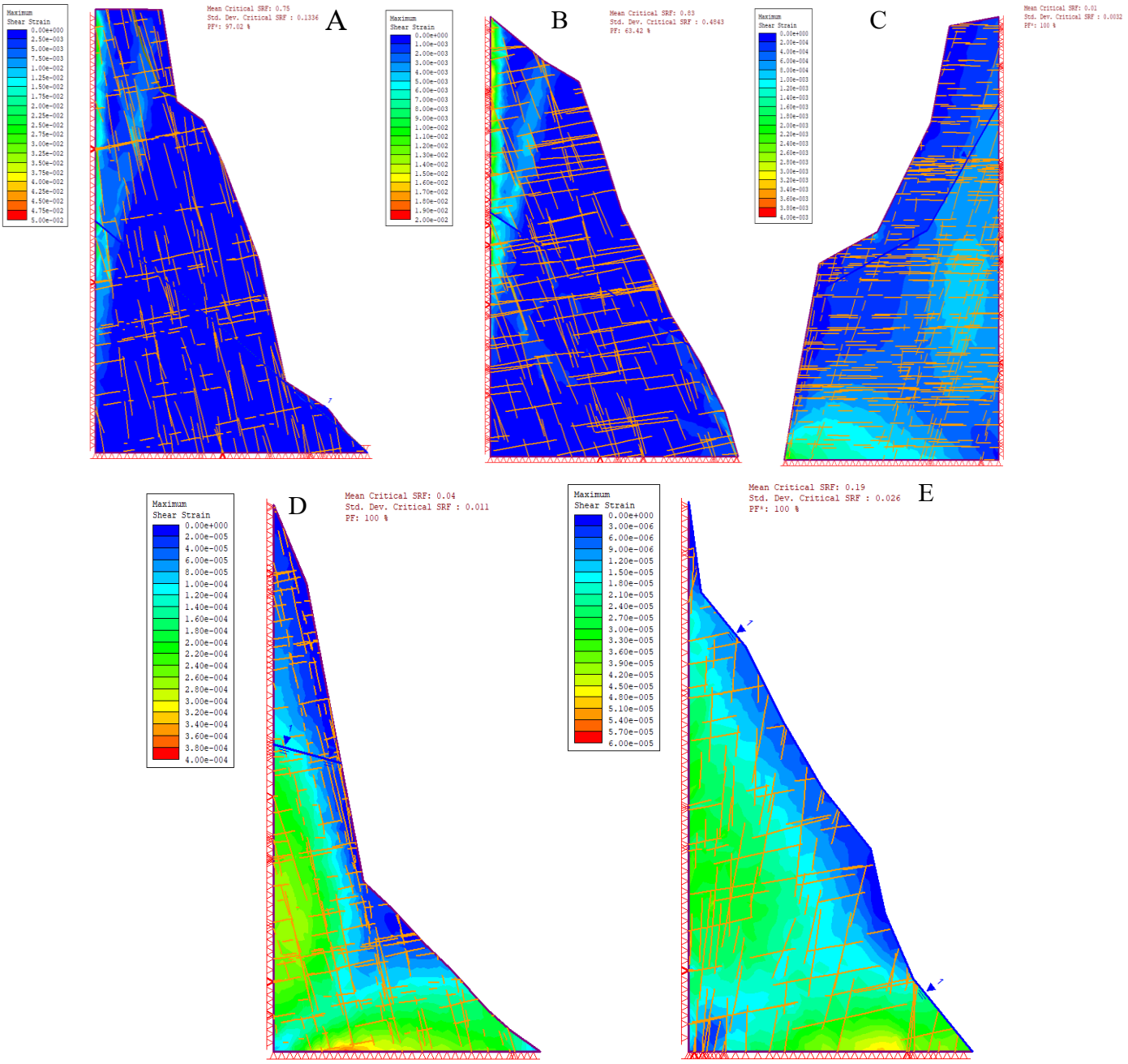

Figure 69 Maximum shear strain for the simulated sections during regular conditions with improbable seismic load applied A section 3, B section 4, C section 5, D section 5 centre (between 4 and 5), E vertical section

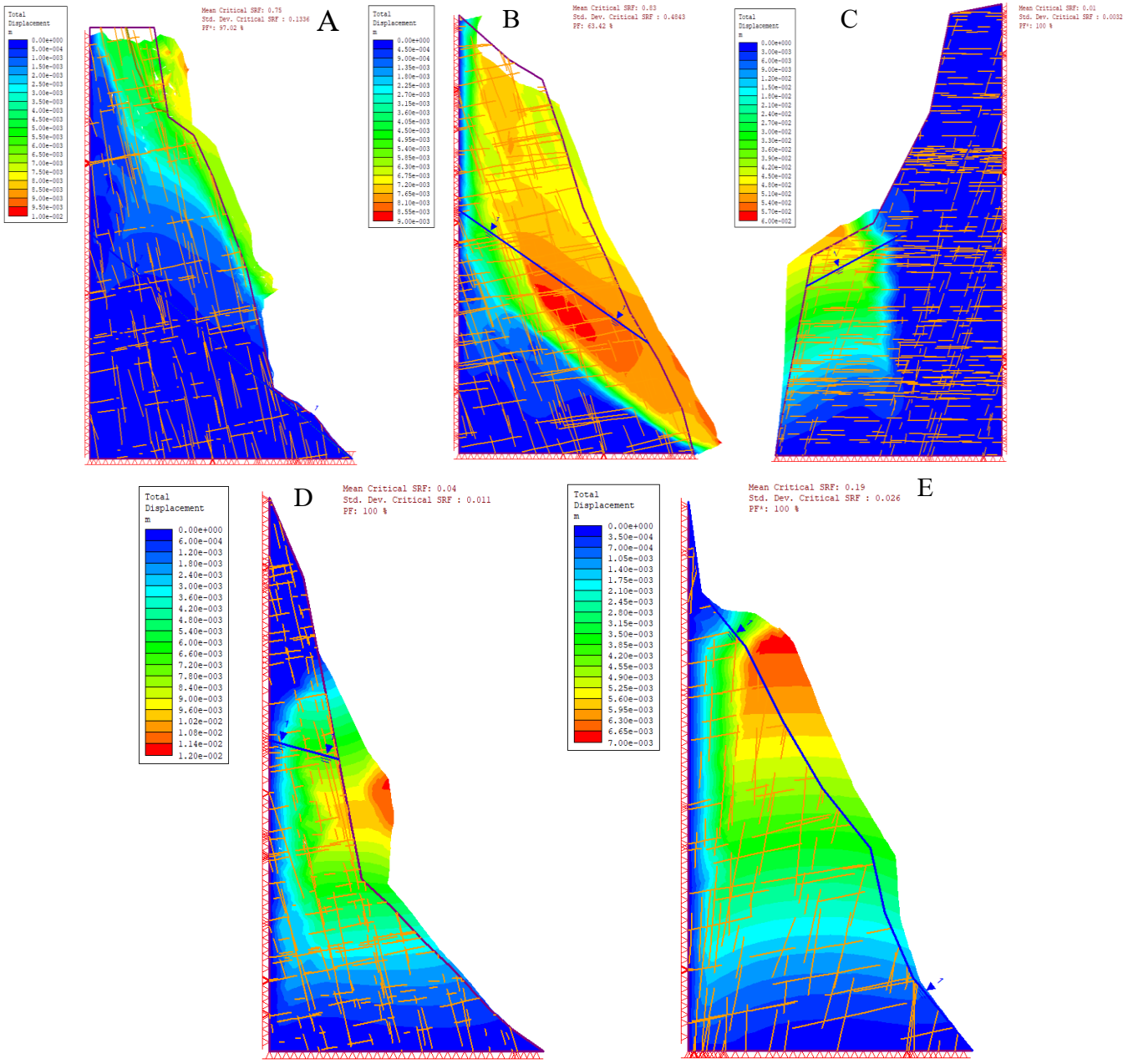

Figure 70 Total displacement for the simulated sections during warmer conditions with improbable seismic load applied A section 3, B section 4, C section 5, D section 5 centre (between 4 and 5), E vertical section

Stability for regular conditions

Under no seismic load with a scenario of higher temperatures the shear strain patterns, Figure 71, keep similar to the ones previously observed except for D which presents the shear strain just above the piezometric line.

For the total displacement, Figure 72, the movements of the rock mass are similar to previous cases with the major difference being that the shear strain present in Figure 71 D has not translated into displacement from that same point but below it.

Under a warmer environment but without seismic loads applied, 3 out of the 5 sections present safety factors, in Table 30, below the ones considered in (Statens Vegvesen, 2018). This is an almost identical case as the one with the real seismic load applied, being this the second high risk scenario present in the analysis.

Table 30 SRF values for the sections under warmer conditions without seismic load applied

Section	Critical SRF	Mean SRF	σ (std dev)	PF %
3	2.15	1.96	0.3185	0.13
4	1.64	0.96	0.6934	52.01
5	0.01	0.01	0.0055	100
5 cent	0.02	0.02	0.0033	100
Vert	0.28	0.21	0.0568	100

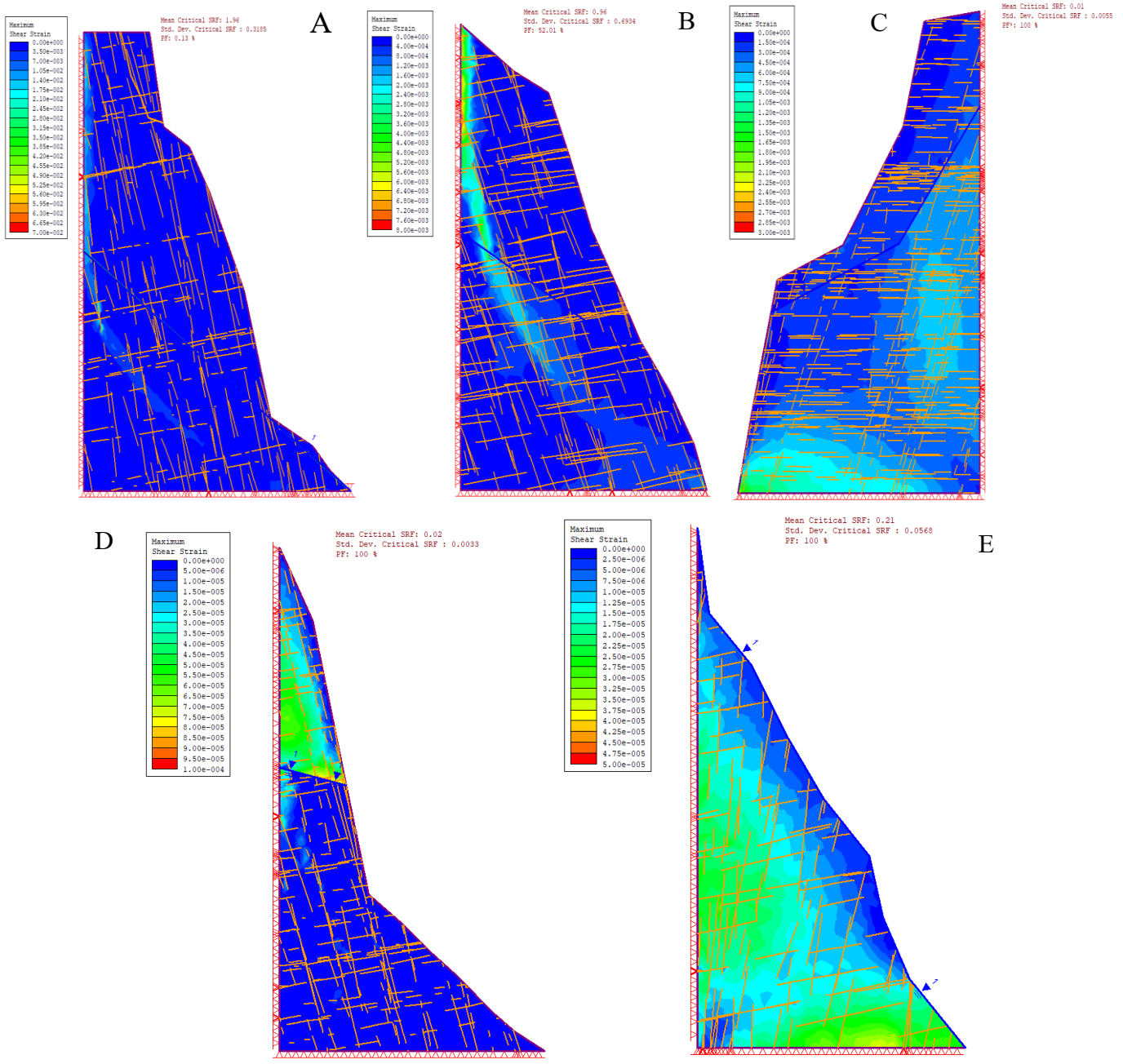

Figure 71 Maximum shear strain for the simulated sections during warmer conditions without seismic load applied A section 3, B section 4, C section 5, D section 5 centre (between 4 and 5), E vertical section

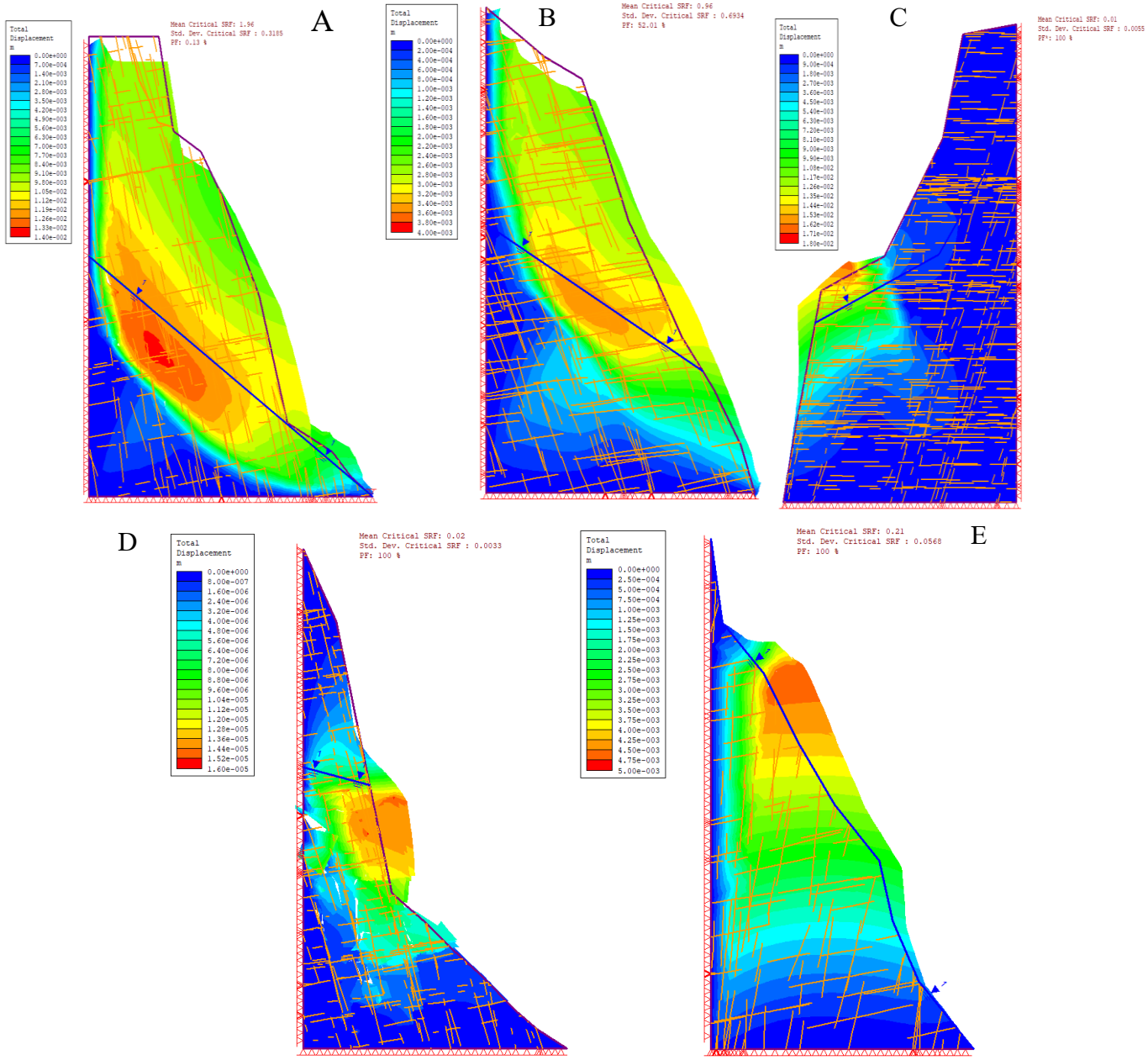

Figure 72 Total displacement for the simulated sections during warmer conditions without seismic load applied A section 3, B section 4, C section 5, D section 5 centre (between 4 and 5), E vertical section

3.7.Summary table

As a summary all the SRF values for the different cases had been collected in and colour coded according to the proposed safety values found in (Statens Vegvesen, 2018) and used previously.

Table 31 Summary results for the slope stability simulations performed

Section	Type of scenario	Actual conditions		Warmer climate scenario	
		Critical SRF	Mean critical SRF	Critical SRF	Mean critical SRF
3	Non earthquake	2.4	2.43	2.15	1.96
	Real earthquake	2.32	2.35	2.07	2.01
	Improbable earthquake	0.89	0.84	0.63	0.75
4	Non earthquake	2.62	1.51	1.64	0.96
	Real earthquake	2.52	1.43	1.58	1.26
	Improbable earthquake	1.93	1.52	1.22	0.83
5	Non earthquake	1.85	1.82	0.01	0.01
	Real earthquake	1.78	1.81	0.01	0.04
	Improbable earthquake	0.18	0.12	0.01	0.01
5 cent	Non earthquake	1.21	1.02	0.02	0.02
	Real earthquake	0.9	0.79	0.07	0.06
	Improbable earthquake	0.23	0.2	0.05	0.04
Vertical	Non earthquake	1.68	2.25	0.28	0.21
	Real earthquake	2.66	2.62	0.27	0.21
	Improbable earthquake	0.64	0.52	0.2	0.19

It can be said that section 5 centre is the most problematic among the ones studied, being unstable across all scenarios.

4. Rockfall simulations under current conditions

The trajectories and landing areas for any possible rockfall event that could occur were performed with RocPro 3D and RAMMS Rockfall to compare between two different approaches on the simulations of these events. First the results of RocPro will be presented followed by the ones from RAMMS. As in a similar approach as with the stability analysis these simulations have been done for actual climatic conditions and for future scenarios with higher groundwater and thus different soil parameters.

4.1. RocPro 3D simulations

4.1.1. Theory

RocPro is a 3D rockfall simulation program based on restitution coefficients for soils and using rigid body mechanics.

As explained in (RocPro 3D, 2019): the block trajectory (time evolution of its position and velocity) is described at each instant by one of the three following types of movements:

- free fall in the air
- frictional sliding (lumped mass) or frictional rolling (rigid block) onto the soil surface
- impact onto the soil

The impact of the block onto the soil, mainly characterized by a large energy dissipation, is considered here as quasi-instantaneous and its depth of penetration in the soil is neglected (it occurs at a fixed position). Starting e.g. from a free fall movement, the impact can lead either to a rebound of the block that begins a new free fall portion, or to a change of kinematics (depending on transition parameters), the block beginning then a sliding or rolling portion onto the soil.

The block trajectory is thus considered as a succession of kinematical phases (free fall portions, or portions with frictional sliding or rolling) separated by purely dissipative phases (impacts). (RocPro 3D, 2019)

The trajectory of a rigid block must satisfy the general dynamic equilibrium relation for translational movements (RocPro 3D, 2019):

$$\sum F = m \times \frac{d^2X}{d^2t} \qquad 46$$

Where F stands for the forces vector, X the global spatial coordinates vector (i.e. describing translation) and t the time.

However, the block shape and rotation are also taken into account, thus the general dynamic equilibrium relation for rotational movements must also be satisfied:

$$\sum M = I \times \frac{d\omega}{dt} \qquad 47$$

Where M stands for the momentum vector, I the block moment of inertia, ω its angular (or rotational) velocity and dω/dt its angular acceleration.

Although the block has a given size and shape, its friction within the air is negligible and its rotation has no effect on its kinematics (this assumption is valid for subsonic velocities and block sizes that are of interest for analysis of rock block trajectories). Consequently, the rotation velocity is not modified during free fall of the block. (RocPro 3D, 2019)

The equilibrium reduces here to equation 46 in which the only force is the block weight P, i.e. F= P. This force being conservative, no energy dissipation occurs during this phase. (RocPro 3D, 2019)

In the rigid block approach (block with a given shape, of radius R and moment of inertia I), the block kinematics onto a surface is considered as a frictional rolling. (RocPro 3D, 2019)

Assuming rolling without sliding for a sphere/plane contact, the geometric compatibility between V and ω yields (RocPro 3D, 2019):

$$\frac{d\omega}{dt} = \frac{1}{R}\frac{dV}{dt} \quad (48)$$

Considering that the sphere/plane contact has a radius u, the rotational equilibrium, equation 47, then writes (RocPro 3D, 2019):

$$I \times \frac{d\omega}{dt} = -T \times R + N \times U \quad (49)$$

T is friction

The forces entering in the translational equilibrium, equation 46, are then the block weight P (conservative), the rolling frictional force T (dissipative) and the normal reaction N. The equilibrium in translation, equation 46, thus writes (RocPro 3D, 2019):

$$\sum F = T + P + N = m \times \frac{d^2X}{d^2t} \quad (50)$$

As said before the impact onto the soil surface is considered as a quasi-instantaneous phenomenon during which the movement is nil (the impact occurs at a fixed position).

Then, the impact is characterized by an energy dissipation, accounted for here by the two restitution coefficients R_N (Normal restitution) and R_T (Tangential restitution). These coefficients are used to modify the velocity components expressed in local coordinates (normal and tangential components with respect to the surface at impact point, and rotational component). (RocPro 3D, 2019)

The normal restitution coefficient is assumed to be independent from the incident rotational velocity $w_{(i)}$, thus the reflected normal velocity $V_{N(r)}$ is obtained from the incident normal velocity $V_{N(i)}$ by (RocPro 3D, 2019):

$$V_{N(r)} = -R_N \times V_{N(i)} \quad (51)$$

A scaling of the R_N coefficient with the normal incident velocity $V_{N(i)}$ is done with (from (RocPro 3D, 2019))

$$R_N(V_N) = \frac{R_N}{1 + \left(\frac{|V_{N(i)}|}{K}\right)^2}$$

K equals= 9.1435 m/s the corrected value is used in 51

The reflected rotational velocity $\omega_{(r)}$ is obtained from the geometrical constrain in equation 52 (RocPro 3D, 2019):

$$\omega_{(r)} = \frac{V_{T(r)}}{R} \quad (52)$$

The reflected tangential velocity $V_{T(r)}$ is obtained as a function of incident rotational and tangential velocity. (RocPro 3D, 2019)

$$V_{T(r)} = \sqrt{\frac{R^2 \times (1 \times \omega_{(i)}^2 + m \times V_{T(i)}^2) \times FF \times SF}{1 + m \times R^2}} \quad (53)$$

FF accounts for the dependence of the tangential restitution coefficient on the incident tangential and angular velocities, due to their incompatibility at impact (in the general case $V_{T(i)} \neq R.w_{(i)}$) (RocPro 3D, 2019):

$$FF = R_T + \frac{1 - R_T}{1.2 + \left(\frac{V_{T(i)} - R \times \omega_{(i)}}{k_1}\right)^2} \quad 54$$

SF accounts for the dependence of the R_T coefficient on the incident normal velocity $V_{(Ni)}$ and on the normal coefficient R_N (RocPro 3D, 2019):

$$SF = \frac{R_T}{1 + \left(\frac{V_{N(i)}}{k_2 \times R_N}\right)^2} \quad 55$$

With the fixed empirical parameters $k_1 = 6.096$ m/s and $k_2 = 76.2$ m/s.

The probabilistic approach used in RocPro3D allows representing by probabilistic variables on the one hand some intrinsic blocks parameters, and on the other hand the main soils physical parameters used to compute blocks trajectories. (RocPro 3D, 2019)

Three blocks parameters can be represented by probabilistic (uniform) variables, namely: (RocPro 3D, 2019)

- their starting position,
- their mass (and size),
- their starting condition (velocity or falling height).

Five soil parameters can be represented by probabilistic (uniform or Gaussian) variables, namely: (RocPro 3D, 2019)

- The dynamic friction coefficient k for rolling (k_r)
- The restitution coefficients along the two components, i.e. normal R_N and tangential R_T
- The lateral (i.e. horizontal) deviation q_H and the flattening (i.e. vertical) q_V of the rebound angle to account for uncertainty on the local slope representation in the DTM. These two angles are applied to the reflected velocity obtained from the corrections brought to R_N and R_T

With ε the deterministic value, its probabilistic value ε_p can be expressed by equation 56 (RocPro 3D, 2019):

$$\varepsilon_p = \varepsilon + D(d_\varepsilon) \quad 56$$

D is a probability distribution of the parameter uncertainty d_ε, with d_ε depending on the incident velocity following the given model (RocPro 3D, 2019):

$$\begin{cases} if\ \|V\| \leq V_{\varepsilon(res)} \rightarrow d_{z(0)} + \dfrac{\|V\|}{V_{s(res)}} \times (d_{z(res)} - d_{z(0)}) \\ if\ \|V\| > V_{z(res)} \rightarrow d_z = d_{z(res)} \end{cases} \quad 57$$

For the soil parameters the Gaussian probabilistic value has been used $\varepsilon_{p(Gaussian)}$ of each parameter is computed from equation 58 (RocPro 3D, 2019):

$$\varepsilon_{p(Gaussian)} = \mu_\varepsilon + \sigma_\varepsilon \times N(0,1) \quad 58$$

Where μ_ε is the parameter mean value (corresponding here to ε), σ_ε its standard deviation (equivalent here to d_ε) and N(0,1) the standard normal distribution sampled from a Box-Muller transformation also using the random number generator.

4.1.2. Simulation parameters

The different parameters for the soil were extracted from the user's manual and are shown in Table 32. The probabilistic approach is obtained as explained in 4.1.1

Table 32 Soil parameters in RocPro 3D (RocPro 3D, 2019)

Parameters	Sane rock	Altered rock	Compact debris	Loose debris	Loose soil	Water surface
RESTITUTION COEFFICIENTS						
Mean normal value m_R_N [-]	0.55	0.5	0.4	0.32	0.3	0
Mean tangential value m_R_T [-]	0.9	0.85	0.85	0.82	0.8	0
Standard.-Deviation s_R [-]	0.011	0.0125	0.016	0.0048	0.012	0
Limit velocity V_R(lim) [m/s]	10	10	10	10	10	0
Limit Std.-Deviation s_R(lim) [-]	0.0055	0.0075	0.012	0.0016	0.006	0
LATERAL DEVIATION						
Standard.-Deviation s_qh [°]	10	8.75	7.5	6.25	5	0
Limit velocity V_qh(lim) [m/s]	10	10	10	10	10	0
Limit Std.-Deviation s_qh(lim) [°]	5	4.375	3.75	3.125	2.5	0
REBOUNDS FLATTENING						
Standard.-Deviation s_qv [°]	1	1	1	1	1	0
Limit velocity V_qv(lim) [m/s]	10	10	10	10	10	0
Limit Std.-Deviation s_qv(lim) [°]	2	2	2	2	2	0
FRICTION COEFFICIENT: sliding (lumped mass) or rolling (rigid block)						
Mean value m_k [-]	0.45	0.5	0.55	0.6	0.6	10
Standard.-Deviation s_k [-]	0.036	0.045	0.045	0.036	0.045	0
Limit velocity V_k(lim) [m/s]	10	10	10	10	10	0
Limit Std.-Deviation s_k(lim) [-]	0.03	0.03	0.03	0.03	0.03	0
TRANSITION PARAMETERS						
Angle b_lim (acute case) [°]	2	3	4	5	6	0
Angle b_lim' (obtuse case) [°]	25	30	35	40	45	0

The first step is to introduce the DTM obtained as shown in 2.2 into to RocPro to generate a TIN (triangular irregular network) and define the soils for the different sections of the terrain, the result can be seen on Figure 73. The colours represent the different soils used; their columns are shaded on those colours in Table 32 to identify their parameters.

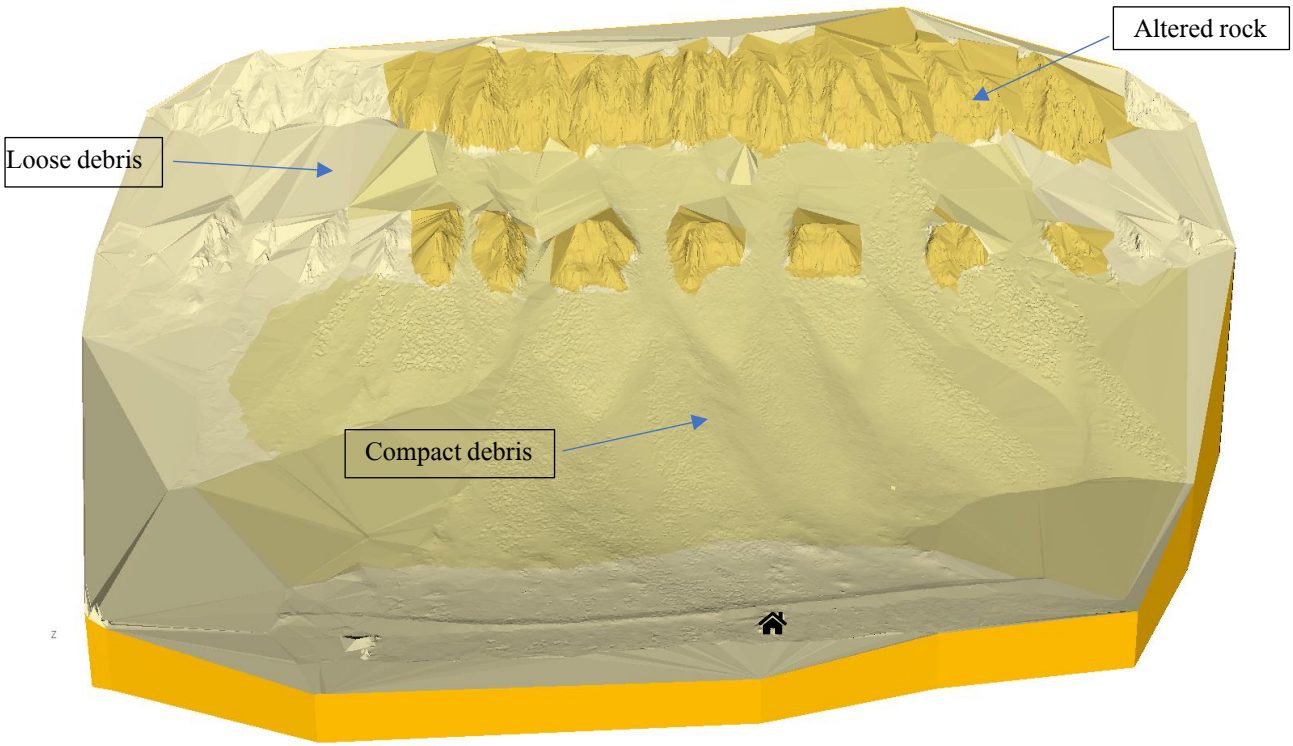

Figure 73 Model of the slope in RocPro 3D, colours represent the different soils applied to the model

The type of terrain was selected by looking for the closest one among the categories that resembled the one present into the area. Figure 74 show the terrain in the area, for the area close to the road and a little further up the terrain on the top of the figure applies, angular rock shapes with some vegetation in between but despite that the rocks are interlocked, that is why compact debris was chosen as terrain type. From the bottom picture in Figure 74 it can be seen that the terrain close to the road has more vegetation and lacks the rock cover seen in levels higher up, for that loose debris was chosen as the terrain type. At the release areas altered rock was identified as the perfect match due to being the rock on them actually altered.

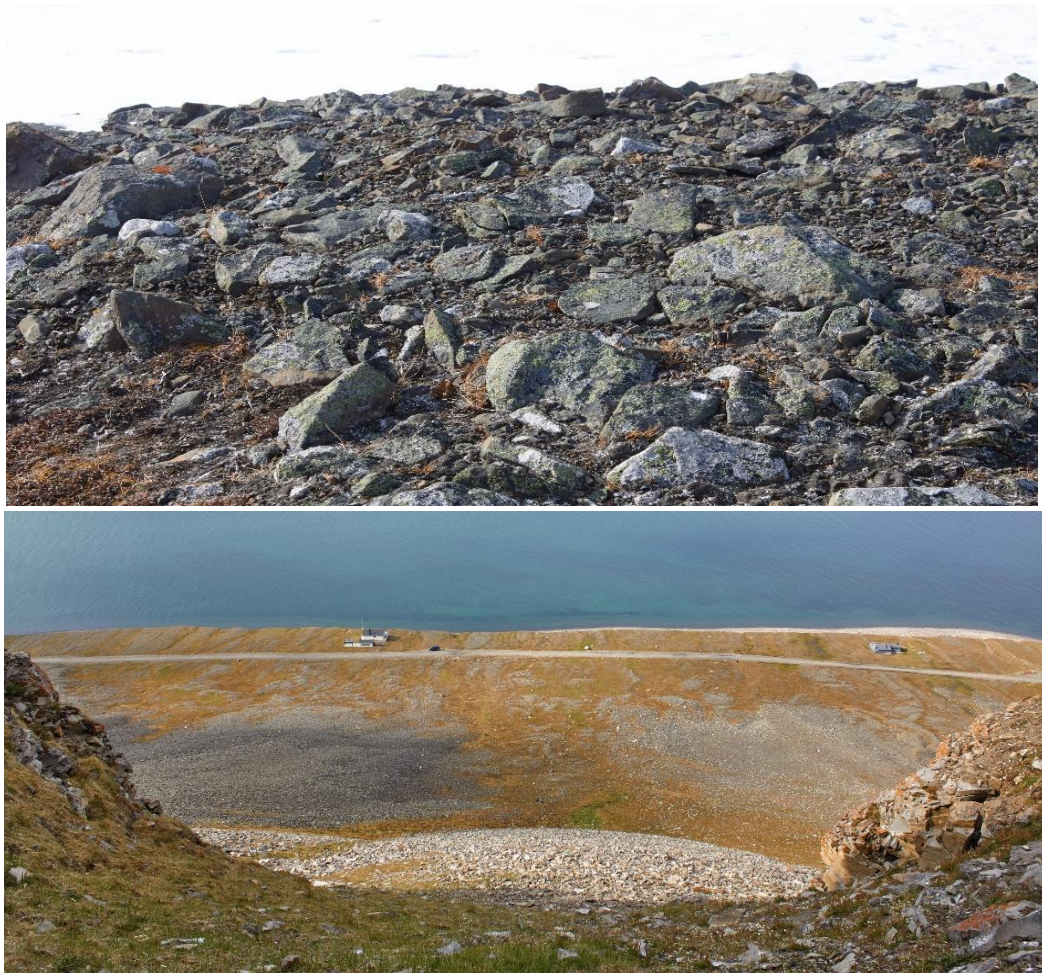

Figure 74 On top detail of the terrain close to the road in the run out area, on the bottom general view of the terrain from the section 5 centre

Release areas were drawn over the identified rock outcrops, seen as yellow polygons on Figure 75, the numbers that identify the release areas where applied by the program when they were created and doesn't correspond with the numeration of the rock outcrops used in Figure 33, for clarification Table 33 includes the associated outcrop for the release areas included on it. The release areas contain the parameters for the blocks that will be simulated during the rockfall. RocPro uses a sphere for the shape of the simulated block.

The parameters for the different release areas are in Table 33, as a probabilistic simulation is performed some of the release areas have on their parameters a range.

Table 33 Parameters for the spheres used in the simulation

Related outcrop	Release area	Density	Sphere diameter	Mass
2	0	2800	0.417-0.423	106.4-110.8
3	1	3400	0.45	162
6	2	2890	0.006-0.007	18.01-18.82
7	3	3100	0.42-0.428	120.3-127.7
1	4	3000	0.335-0.345	59.08-64.39
Vertical wall	5	3500	0.471-0.576	1649-2016
5 centre	6	3248.5	0.23	20.69
4	7	2859	0.35	64.18
5	8	3638	0.4	121.9

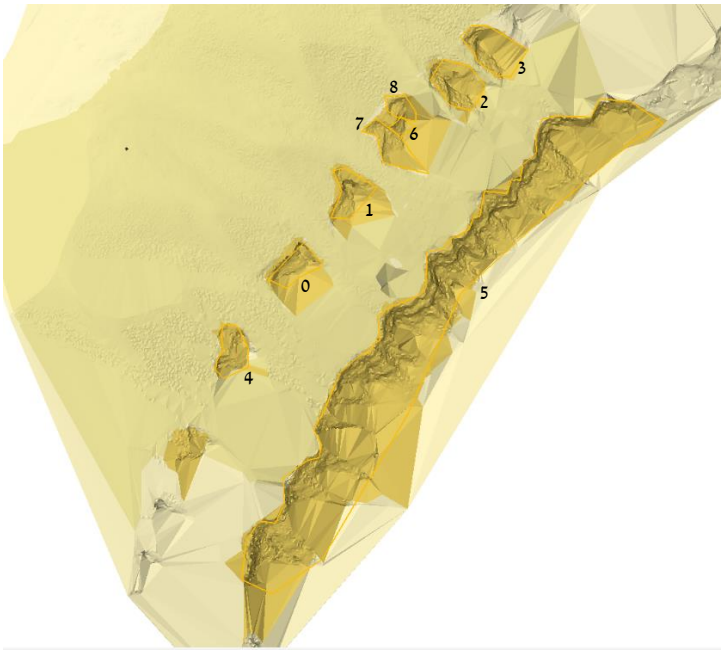

Figure 75 Release areas on the slope

4.2. RAMMS Rockfall simulations

4.2.1. Theory

The RAMMS: ROCKFALL model utilizes a hard- contact, rigid-body approach to model rockfall trajectories in general three-dimensional terrain (SLF/WSL, 2016)

To date most rockfall models utilize simple rebound mechanics to describe the complex interaction between the rock and the ground, rock geometries consisted of simplified shapes, spheres, or ellipsoids. (SLF/WSL, 2016)

The rock-ground interaction was parameterized using apparent restitution coefficients to model the rock jumping and to account for the wide variation of possible jump distances and heights, random, stochastic methods were used to define the bandwidth of possible restitution coefficients. (SLF/WSL, 2016)

In RAMMS the rock-ground interaction is parameterized by frictional operators that act at the rock surface. Compared to rebound models (that employ apparent restitution coefficients to model entire ground-rock interaction), the hard-contact, rigid-body approach applies contact forces to the rock's edges and corner points. The primary advantage of using hard-contact approach is that the role of rock shape is accounted for in the ground-rock interaction. This facilitates a natural modelling of the four primary modes of rock motion: sliding, rolling, skipping and jumping – without the use of random, stochastic methods to define the rebound parameters. (SLF/WSL, 2016)

The natural variation of jumps is defined automatically by the rock shape and orientation at impact, the statistical spread of rockfall runout and dispersion is generated only by changing the initial conditions. Ground parameters are not random: they are deterministic in the sense that one material type is assigned to describe hardness and the general tendency of the terrain to react to a rock impact. (SLF/WSL, 2016)

The RAMMS model needs the shape and size of the rock they are modelled as a convex hull polyhedron, real rock geometries obtained from laser scans during field investigations can be used in a modelling application, the rocks are considered indestructible; that is, they do not fragment or change form during the analysis. (SLF/WSL, 2016)

Another feature of the RAMMS: ROCKFALL model is the inclusion of rock rotations in both the airborne phase and during the interaction with the ground. The RAMMS: ROCKFALL model includes gyroscopic forces induced by rock rotations. These forces are necessary to model wheel-like rock skipping and jumping modes that are often responsible for extreme runout. To model ground interaction considering rocks with arbitrary geometry and rotational speed requires methods to accurately track the rock orientation relative to the ground. RAMMS: ROCKFALL employs quaternion algebra for this purpose. This method tracks rotation sequences even when non-linear contact forces change the translational and rotational direction of the rock. (SLF/WSL, 2016)

Rock bodies are introduced into the simulation domain coordinate frame with origin (O) as a cloud of points based in a coordinate system of their own with origin (K). The coordinate frame (K) serves to map the rotations of the rock-body. The centre-of-mass of the body is calculated assuming the density is homogeneous. The inertial tensor of the body is calculated finding the three principal moments of inertia; the origin is the rock's gravity centre (S). The translations of the rock-body in the simulation domain are mapped using coordinate frame S in relation to O. (SLF/WSL, 2016)

In free flight, the governing formula of motion is equation 59 (SLF/WSL, 2016)

$$M\dot{u} - h(q,u) = 0 \qquad 59$$

where M is the constant and diagonal mass matrix (containing the mass and three moments of inertia I). The vector u contains the rock's three translational and three rotational velocities. The rock-body's motion is governed by a number of forces which determine its trajectory. Gravitational force (Fg) acts globally; a drag force (D) is implemented to represent the effects of trees, undergrowth and soil deformation. Along with gyroscopic forces G which can cause rocks of irregular shape to become upright and rotate about a rolling axis.

All force terms h are a function of the rock's position q and velocity u forming the force vector h (SLF/WSL, 2016)

$$h(q,u) = \begin{bmatrix} F_g + D \\ G \end{bmatrix} \quad 60$$

On contact detection between the rock-body and the terrain, contact forces λ and frictional contact forces (Fc) act about the point of contact. These forces can be considered as external forces that change the direction of the falling rock. The contact of the rigid rock-body is detected by continually measuring the vertical gap length g_N between the rock-body's corner points (P) and the terrain projections (Q). The gap length is defined as equation 61.

$$g_N(X,Y,Z) = Z - Z_m(X_m, Y_m) \quad 61$$

When $g_N > 0$ there is no contact; when $g_N \leq 0$ there is contact and the contact forces λ acting at the contact point P, are computed. (SLF/WSL, 2016)

Contact forces are modelled as hard unilateral constraints with Coulomb friction using non-smooth contact dynamics approaches. For the case of contact, the governing equation of motion now becomes equation 62

$$M\dot{u} - h(q,u) = \lambda W(q) \quad 62$$

The contact frame C has a normal contact force component λ_N and two tangential components λ_{T1} λ_{T2}. The contact force λ_N guarantees the unilaterality of the contact, i.e. the non-penetration constrains. The tangential force components are due to Coulomb friction and are governed by the contact laws. (SLF/WSL, 2016)

Impulsive contact forces occur whenever the gap function detects contact with negative velocity $\gamma_{\bar{N}} < 0$ that is to say that the point would theoretically move through the terrain surface if not treated with the impulsive contact force. This requires a velocity jump such that the post impact normal velocity is non-negative $\gamma_N < 0$. (SLF/WSL, 2016)

This impact law is based on Newtonian impact law in which the relative normal velocities of the contact pair before and after impact are governed by ε_N the normal restitution coefficient. $\varepsilon_N = 1$ corresponds to complete restitution of normal velocity while a smaller ε_N dissipates energy. Generally speaking, this value is set very low. Newton's action-reaction law is always fulfilled. (SLF/WSL, 2016)

To determine the resultant force direction acting on the rock-body the configuration of the impact must be computed. This requires finding the relative velocity between the contact points P and the terrain Q. Importantly, the velocity of contact point P is composed of the translational velocity with respect to the body's centre of mass V_s and its angular velocity Ω_K in the fixed body frame (K); for which P also has a fixed position vector relative to the centre of mass S. That is, the contact algorithm in the rigid-body approach considers the rotational speed of the rock at contact. Because the forces are then applied at points away from the centre of mass, and with a direction respecting the impact configuration to a body with three degrees of translational and rotational freedom, torques and moment, arms can act generating rotations and rebounds that represent the true mechanics of an impact. (SLF/WSL, 2016)

Two physically different forces oppose the motion of a falling rock: sliding friction and drag. Sliding friction acts at points of the rock's surface that are in contact with the ground; it is Coulomb-type friction associated with the distance the rock slides on the ground. Drag, on the other hand, acts at the rock's centre of mass and therefore creates no additional rotational moments. It acts in the direction opposite to the rock's movement (velocity). (SLF/WSL, 2016)

To simulate ground deformation within the framework of a hard contact model requires introducing a slip (s) dependent friction that acts during sliding and accounts for the increase in friction due to material accumulation behind the rock- body as it slides through the impact. The slip dependent friction is an extension

of the Coulomb friction model in which the friction value μ is made dependent on the slip distance (s) travelled by the centre of mass μ(s) (SLF/WSL, 2016)

An additional slip dependent drag force is introduced to account for the viscoplastic deformation that occurs in soft soils under rock impact. Large viscoplastic deformations are also encountered in harder substrate materials such as scree, where rubbing between scree granules dissipates energy. Viscoplastic ground drag is given by equation 63 (SLF/WSL, 2016):

$$F_v = -\frac{m}{2} C_v v_s^2 \qquad 63$$

4.2.2. Simulation parameters

Following a procedure similar to the one explained in 4.1 the terrain was created into RAMMS rockfall as shown in Figure 76.

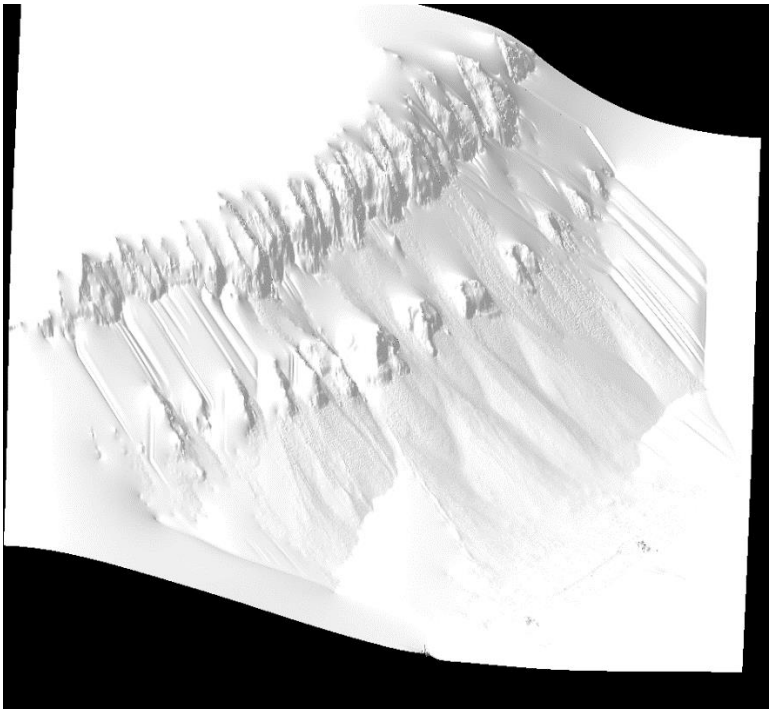

Figure 76 DTM generated inside RAMMS rockfall

With the terrain created the next step was to define the release zones and the types of soil that defines the terrain.

The type of terrain was defined using the examples of soil depicted into the RAMMS rockfall manual as shown in Figure 77 with the parameters for each in Table 34.

Table 34 RAMMS soil parameters

Terrain	Mu_Min	Mu_Max	Beta	Kappa	Epsilon	Drag
Extra soft	0.2	2	50	1	0	0.9
Soft	0.25	2	100	1.25	0	0.8
Medium soft	0.3	2	125	1.5	0	0.7
Medium	0.35	2	150	2	0	0.6
Medium hard	0.4	2	175	2.5	0	0.5
Hard	0.55	2	158	3	0	0.4
Extra hard	0.8	2	200	4	0	0.3

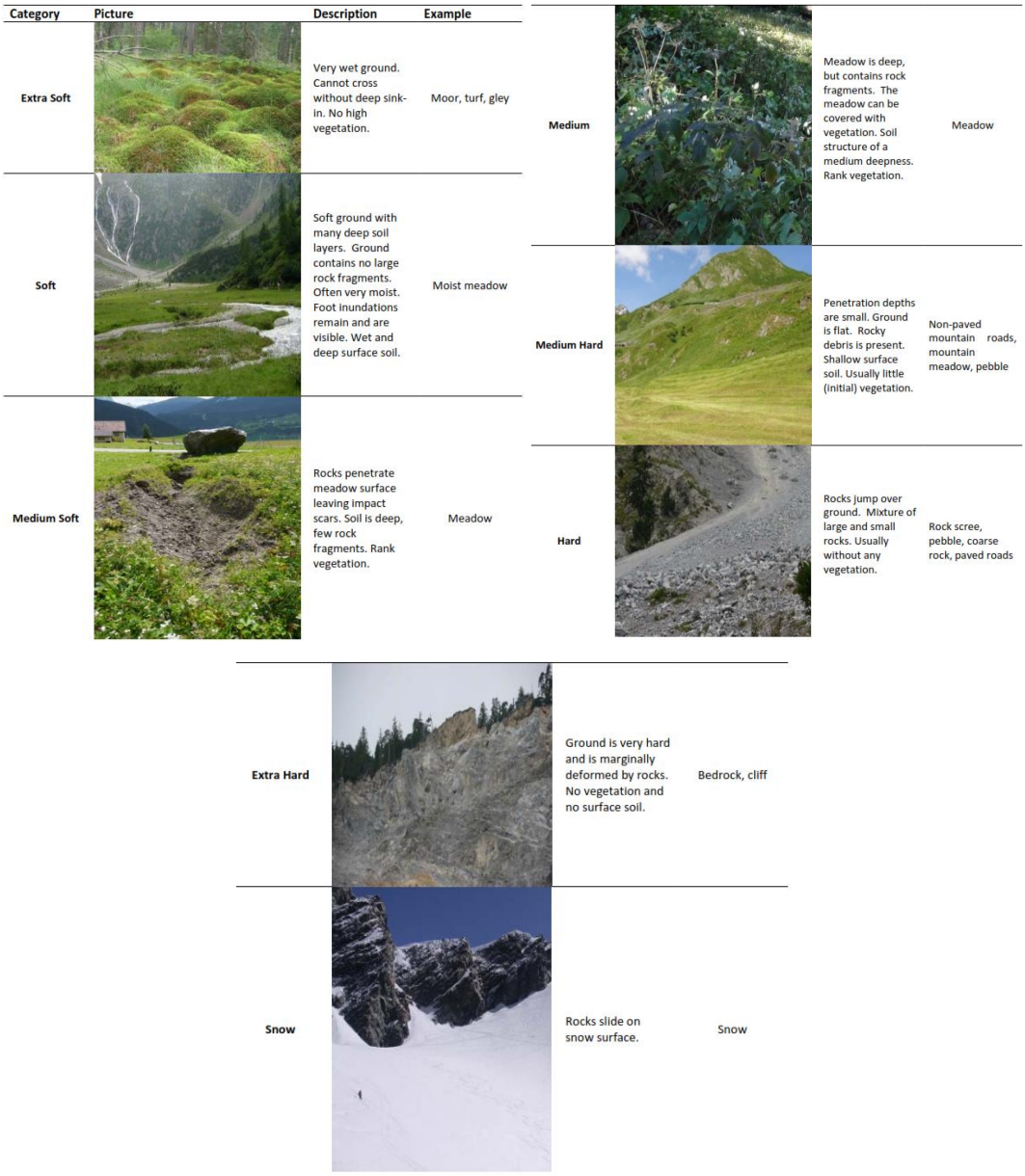

Figure 77 Types of terrain in RAMMS rockfall (SLF/WSL, 2016)

The soils selected were extra hard for the release areas, hard for the zones between release areas (vertical wall and outcrops), medium hard for the terrain below the rock outcrops and medium for the low terrain. The polygons used to define and separate the types of soils are shown in Figure 78, light green are the release areas, orange is the terrain between the vertical section and the rock outcrops, blue is the midground and dark green represents the low ground.

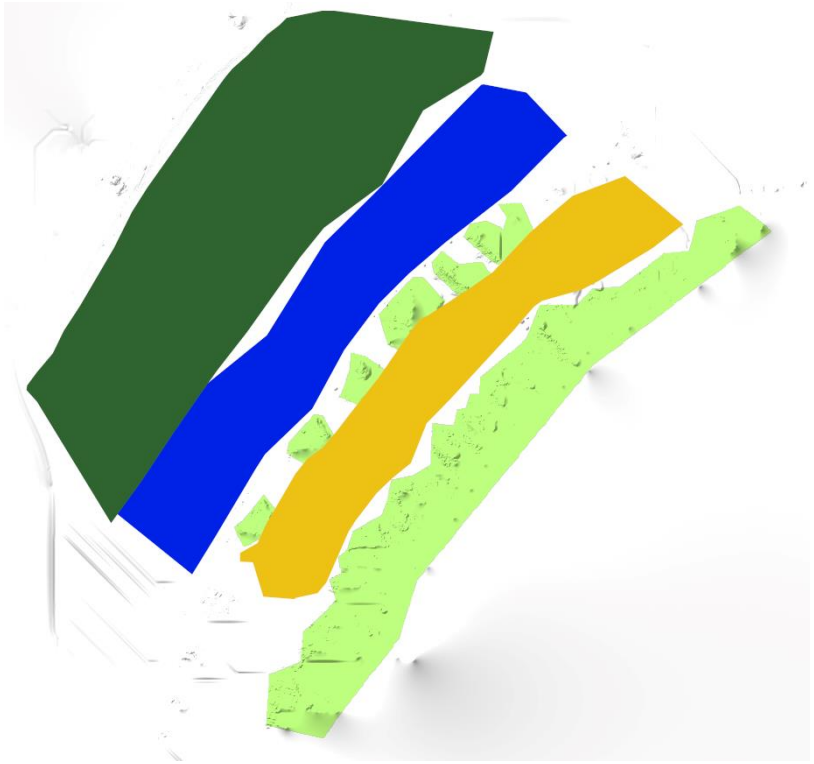

Figure 78 Polygons used to define the soil types on the terrain

The release areas where defined by lines at the edge of the different studied sections instead, this is shown in Figure 79.

Figure 79 Release lines for the RAMMS rockfall simulations

In the type of model that RAMMS uses the shape of the rock is of utmost importance as it changes the impact behaviour (drag, slip, rotate), energy absorbed and released and trajectory after impact. During fieldwork photos of the big rocks present at the area were taken to generate 3D models using photogrammetry techniques, these models were then included into RAMMS Rockfall rock builder. The rocks used are shown in Figure 80.

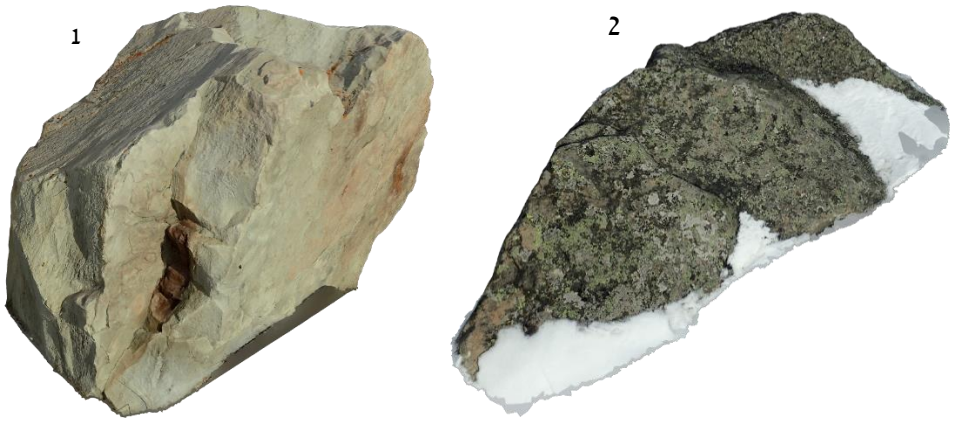

Figure 80 3D models of the rocks used for the RAMMS Rockfall simulations

The simulations were done using both rocks but not simultaneously, in that way is easier to see the behaviour of the different shapes and density assigned to each rock. The densities are the same as the ones calculated on step 2.1.1, the highest and the lowest values were selected to represent both extremes of the possibilities.

The characteristics of the rocks are in Table 35

Table 35 Characteristics of the rocks used in RAMMS Rockfall simulations

Rock	Density kg/m³	Volume m³	Mass kg
1	3400	0.84	2856
2	2859	0.14	400.26

Each simulation consisted of 1120 rock runs.

5. Rockfall simulations under current conditions results and discussion

5.1. RocPro results and discussion

From the simulations the data that is presented is the energy, the velocity, and the jump height of the rockfall event with a confidence interval of the 95 %. For easy location, the cabin emplacement has been signalled with a black house icon.

Figure 81 shows the first set of RocPro results regarding energy, velocity and height. In addition, Figure 82 shows the trajectories from an aerial view point. None of the simulated trajectories represent a direct threat to the cabin or its surroundings.

All of the stopping points for the simulated rocks are located on the safe side of the road away from the cabin but, close to the change of terrain class higher on the new terrain, to check if this is a problem with the terrain settings or with how the simulation takes place this results will compared later on with the ones from RAMMS rockfall directly and by incorporating the drag coefficients of RAMMS terrain values into RocPro.

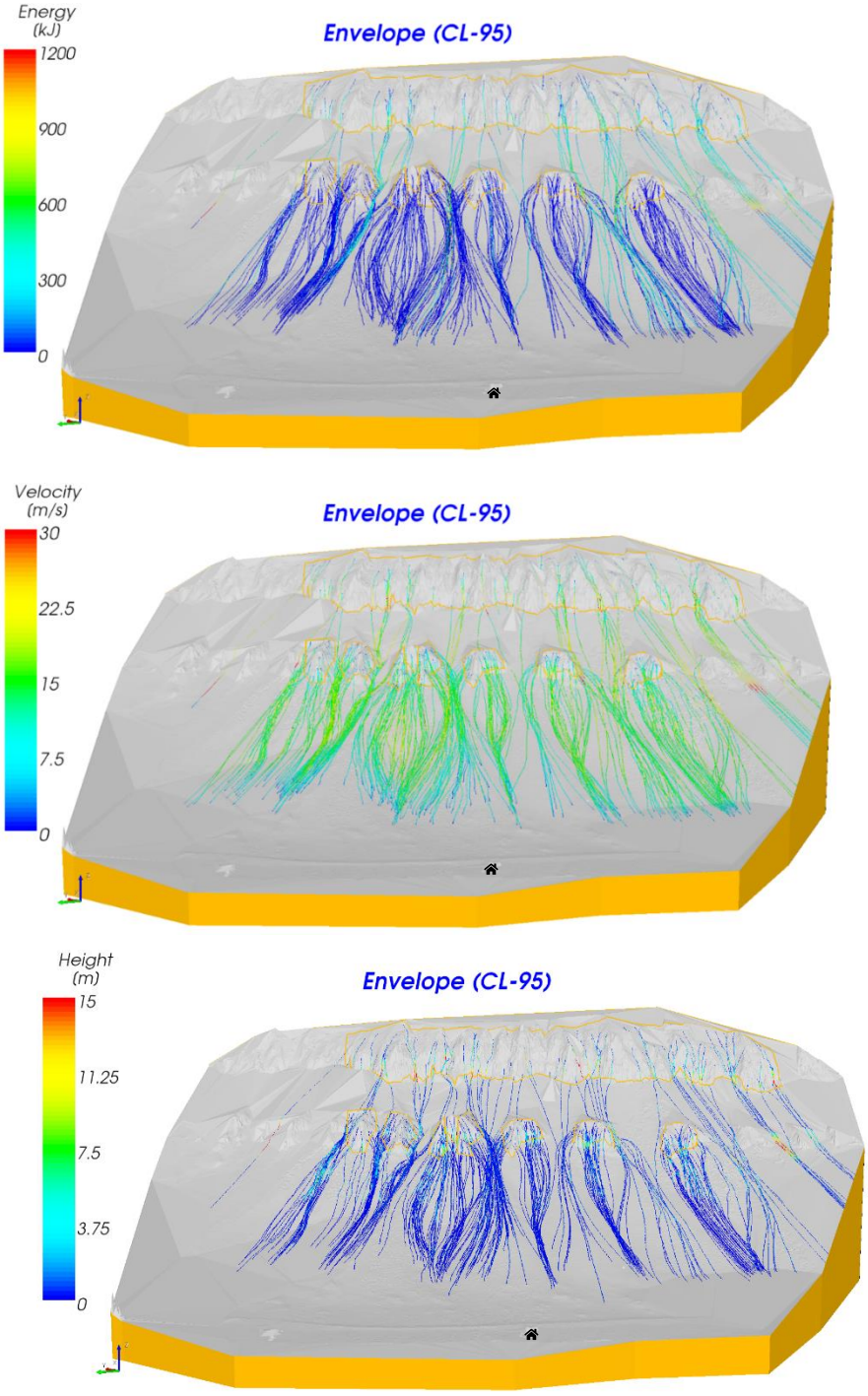

Figure 81 RocPro simulation results for regular conditions, top kinetic energy, middle rock velocity, bottom rock height

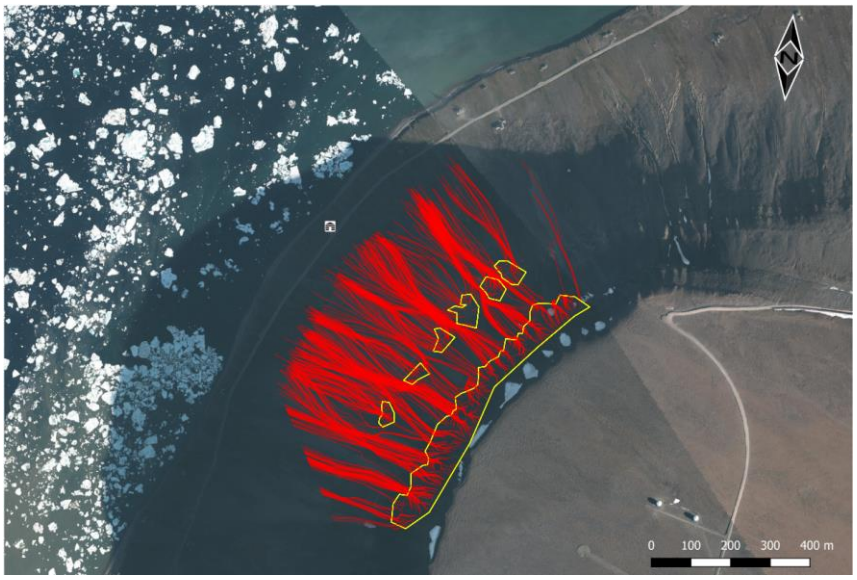

Figure 82 RocPro simulations results after 10 rounds. In yellow the release areas in red the rock trajectories

5.2. RAMMS Rockfall results and discussion

On Figure 83 the kinetic energy of the rocks is portrayed, on top for the simulation with rock 1 and in the bottom for rock 2, Figure 84 shows the velocity values while Figure 85 shows rock height. On one hand rock 1 events represent a real threat to the cabin, some of the trajectories directly hit the cabin or are really close to the vicinity, also they keep high amounts of energy, around 800 to 1000 kJ. and thus, velocity even at the final sections of their trajectories. Regarding their movement behaviour the rocks have a rolling movement at the final sections with a maximum height jump for the elements that cross the road of 1.6 to 2 m

Said that, rocks of the size of rock 1 are uncommon and at the same time RAMMS do not simulate possible rock fractures during travelling which will reduce the size, mass and dissipate more energy probably reducing the consequences. On the other hand events with rock 2 have no consequences, the rocks travel very short distances, especially those that start from the outcrops, and the stopping points are located at the top of the final section of the slope, also they reach energy values 10 times smaller than those from rock 1. Considering where the rock 2 simulations end, which is the area that presents most of the rocky debris, it can be supposed that this could be the events that take place more frequently.

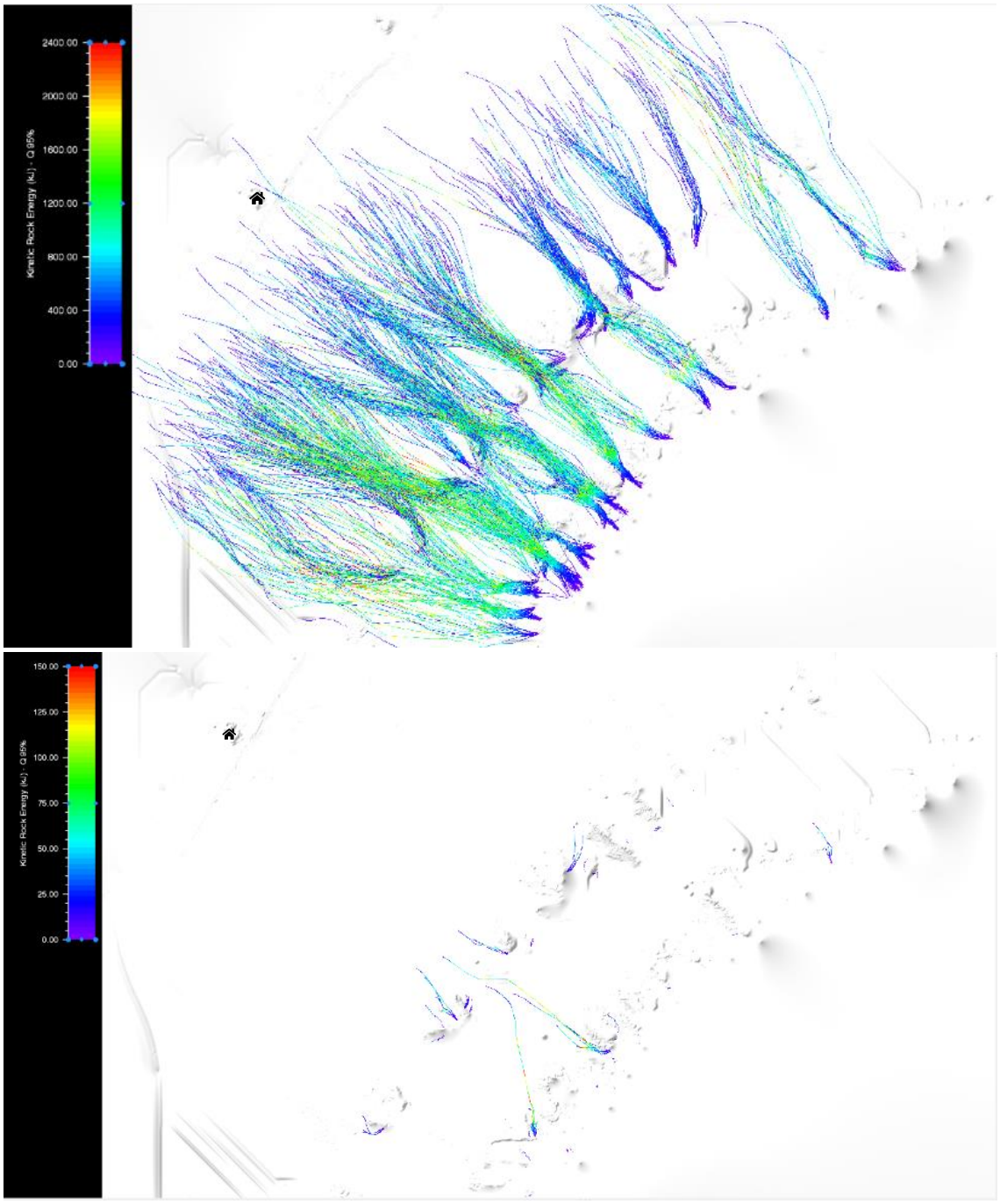

Figure 83 Rock kinetic energy for actual conditions, on top simulation with rock 1 on the bottom simulation with rock 2

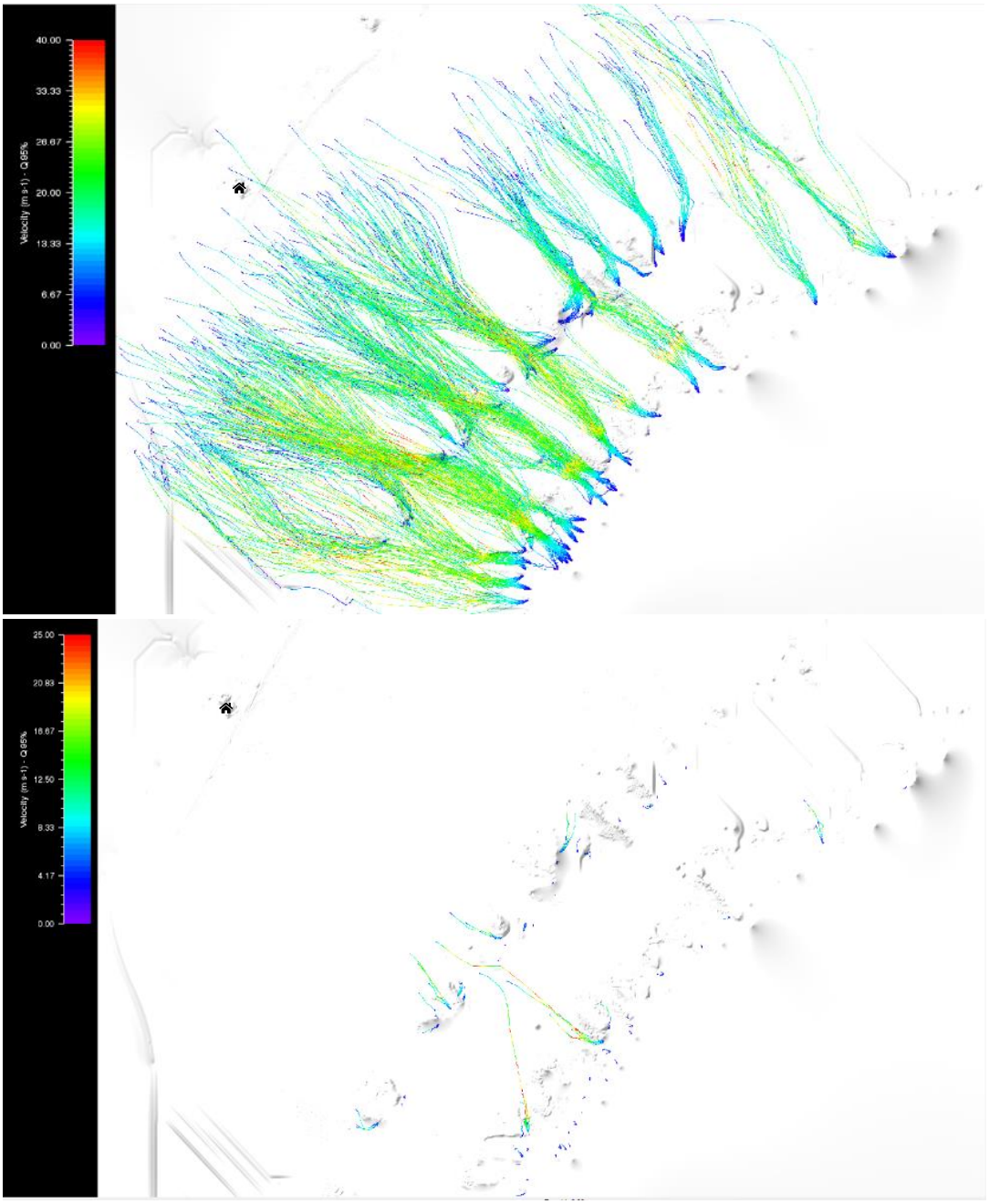

Figure 84 Rock velocity for actual conditions, on top simulation with rock 1 on the bottom simulation with rock 2

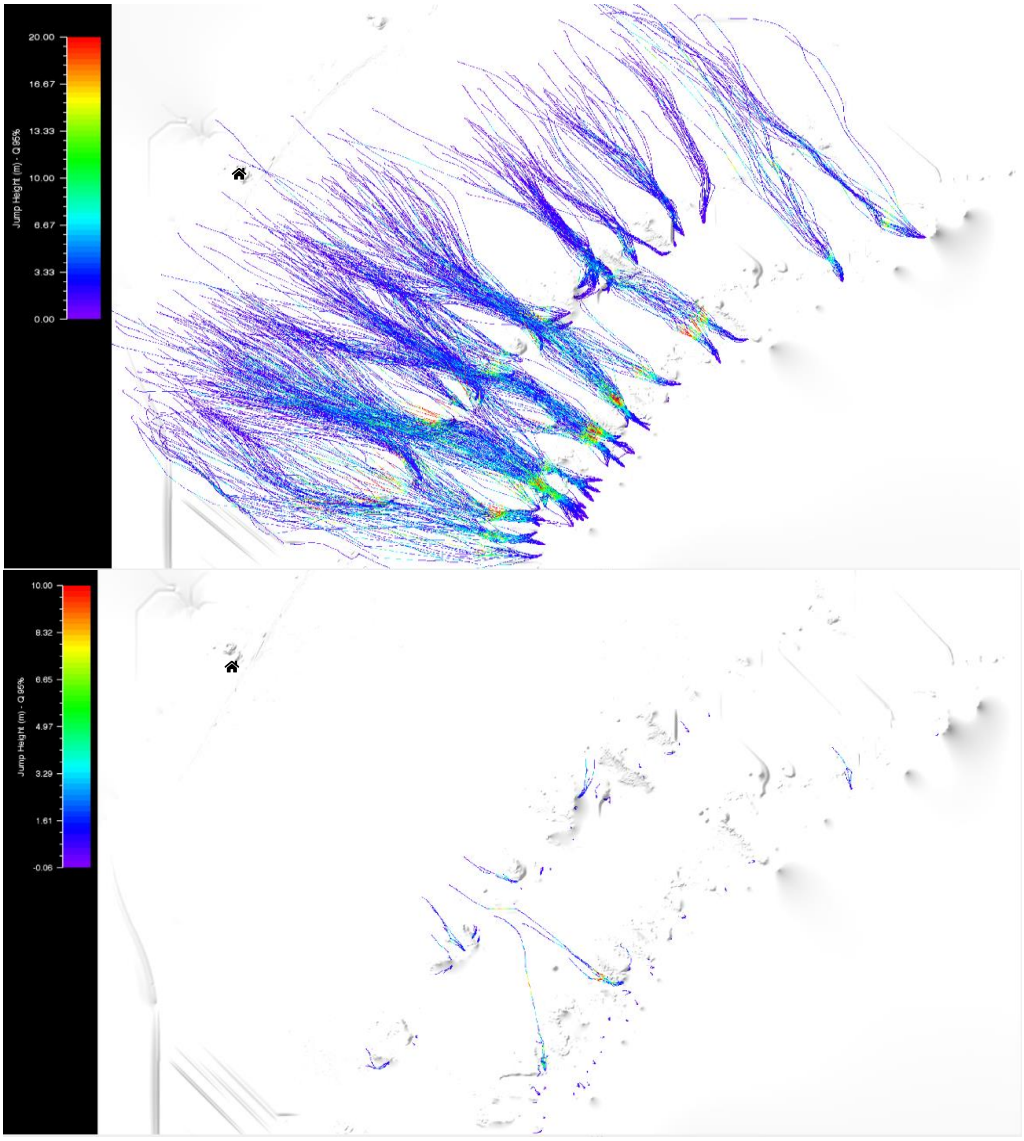

Figure 85 Rock height for actual conditions, on top simulation with rock 1 on the bottom simulation with rock 2

5.3.Comparison between RocPro and RAMMS Rockfall

Figure 86 shows the kinetic energy for a simulation with rock 1 in RAMMS and a simulation in RocPro, the main difference between programs is how they represent the objects, how the density of them are used and the mechanisms for the movement and energy simulation. For Roc pro the release areas contain the value of the density that will be used for the spheres of that area and they were incorporated according to the values obtained from samples for the corresponding areas with some variability. In the case of RAMMS the simulation was done with real rock shapes instead of spheres with the same density value for all the simulated elements.

In the case of the RAMMS simulation the cabin is under real risk of damage from a rockfall event meanwhile in RocPro is safe. At the same time the kinetic energy on RAMMS is double the one calculated in RocPro. This is using the default values for the types of soil in both programs.

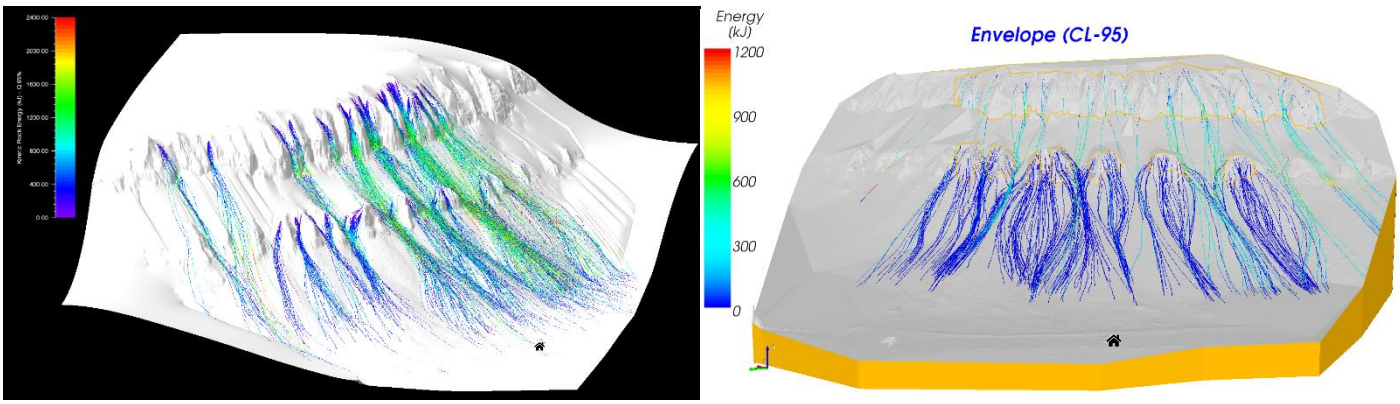

Figure 86 Kinetic energy results for RAMMS Rockfall on the left and RocPro 3D on the right

Introducing the same drag coefficient that were used for the RAMMS simulations into the soil characteristics for RocPro, it gives the outcome shown in Figure 87. The max calculated energy is still half the one for the RAMMS results but the runout of the rockfall event is now much more similar with elements reaching the vicinity of the cabin.

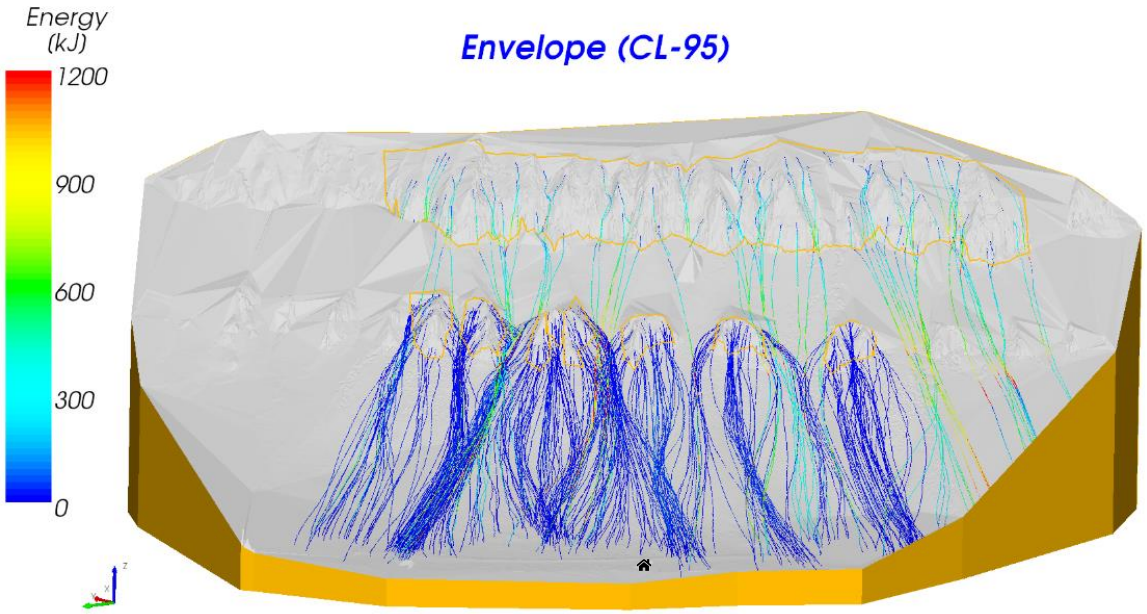

Figure 87 Kinetic energy results for RocPro 3D using soil drag coefficients from RAMMS Rockfall

The big difference in the calculated energy must be a result of the different approach that the programs have for the interaction between rocks and terrain. This could influence the apparent stopping points as with a larger energy the rocks could travel a larger distance then ending in closer and more risky areas for the cabin.

As the simulations with rock 2 in RAMMS are not risky and spheres with the same density as rock 2 are already included in the RocPro simulations a direct comparison of the results for that scenario has not been done.

6. Rockfall simulations for increased temperatures

Using the same procedure as in 4 the rockfall simulations where done in an scenario of increased temperatures. To represent that types of terrain with softer characteristics were selected, as with the increase in the amount of water present in the soil they tend to present that behaviour. Softer soils tend to present higher drag values and absorb more energy on the impact.

6.1. RocPro 3D simulation parameters

The original soil types were changed for the ones highlighted in Table 36

Table 36 Soil types and values for RocPro 3D under warmer conditions

Parameters	Sane rock	Altered rock	Compact debris	Loose debris	Loose soil	Water surface
RESTITUTION COEFFICIENTS						
Mean normal value m_R_N [-]	0.55	0.5	0.4	0.32	0.3	0
Mean tangential value m_R_T [-]	0.9	0.85	0.85	0.82	0.8	0
Standard.-Deviation s_R [-]	0.011	0.0125	0.016	0.0048	0.012	0
Limit velocity V_R(lim) [m/s]	10	10	10	10	10	0
Limit Std.-Deviation s_R(lim) [-]	0.0055	0.0075	0.012	0.0016	0.006	0
LATERAL DEVIATION						
Standard.-Deviation s_qh [°]	10	8.75	7.5	6.25	5	0
Limit velocity V_qh(lim) [m/s]	10	10	10	10	10	0
Limit Std.-Deviation s_qh(lim) [°]	5	4.375	3.75	3.125	2.5	0
REBOUNDS FLATTENING						
Standard.-Deviation s_qv [°]	1	1	1	1	1	0
Limit velocity V_qv(lim) [m/s]	10	10	10	10	10	0
Limit Std.-Deviation s_qv(lim) [°]	2	2	2	2	2	0
FRICTION COEFFICIENT: sliding (lumped mass) or rolling (rigid block)						
Mean value m_k [-]	0.45	0.5	0.55	0.6	0.6	10
Standard.-Deviation s_k [-]	0.036	0.045	0.045	0.036	0.045	0
Limit velocity V_k(lim) [m/s]	10	10	10	10	10	0
Limit Std.-Deviation s_k(lim) [-]	0.03	0.03	0.03	0.03	0.03	0
TRANSITION PARAMETERS						
Angle b_lim (acute case) [°]	2	3	4	5	6	0
Angle b_lim' (obtuse case) [°]	25	30	35	40	45	0

With the terrain areas shown in Figure 88

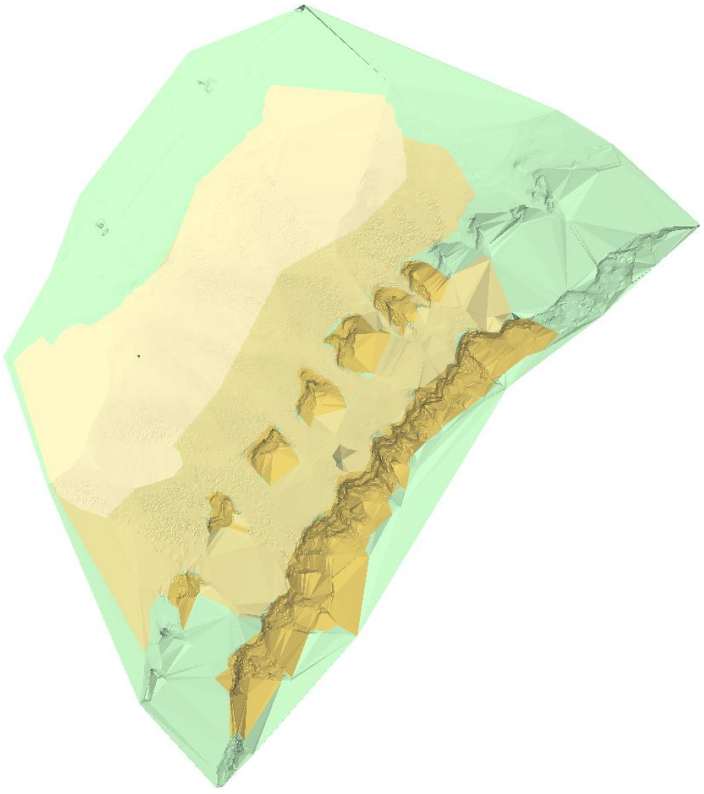

Figure 88 Soil type location in the RocPro 3D model colours represent the different soils applied

6.2. RAMMS Rockfall simulation parameters

As previously exposed the only change done was changing the soil types to represent the new conditions in which the rockfall event would take place.

The soils selected were extra hard for the release areas, medium hard for the zones between release areas (vertical wall and outcrops), medium for the terrain below the rock outcrops and medium soft for the low terrain. The polygons used to define and separate the types of soils are shown in Figure 89, light green are the release areas, orange is the terrain between the vertical section and the rock outcrops, blue is the midground and dark green represents the low ground.

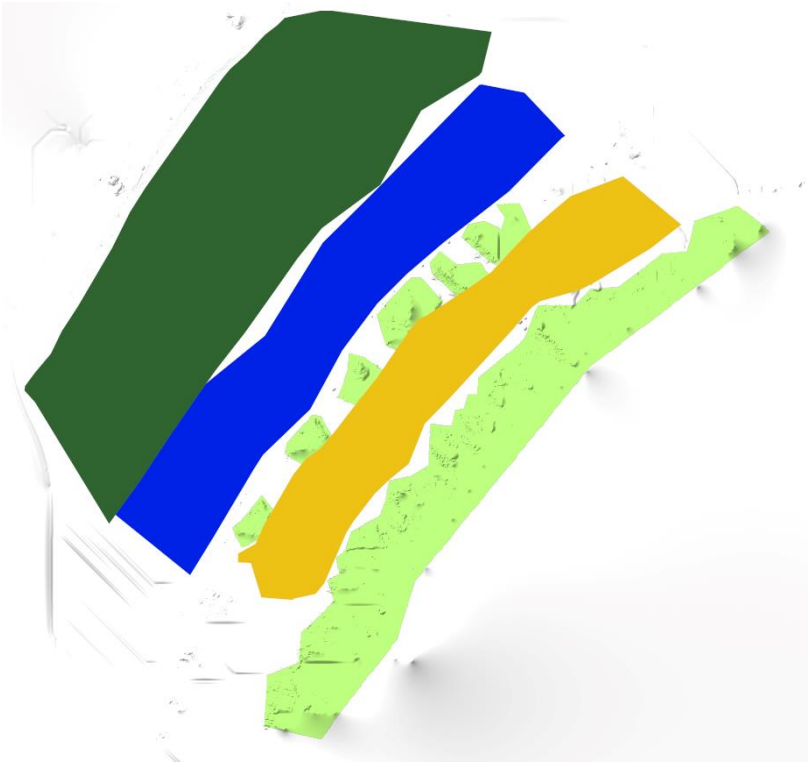

Figure 89 Polygons used to define the soil types on the terrain

The simulations were also performed with the two rocks types shown previously on Figure 80

7. Rockfall simulations results and discussion for increased temperatures case

7.1. RocPro results and discussion

In this scenario shown in Figure 90 the maximum energy is slightly lower than for the previous results, 1100 in this case 1200 for the normal conditions. In the case of the velocity the results are similar.

As in previous case the trajectories present no risk for the cabin or its surroundings. Comparing both cases, the results does not show a big difference between the regular conditions and a warmer environment. A bigger change in the results was expected as when previously compared with RAMMS, this program is highly susceptible to just a change in the drag parameter of the soil when the values were substituted.

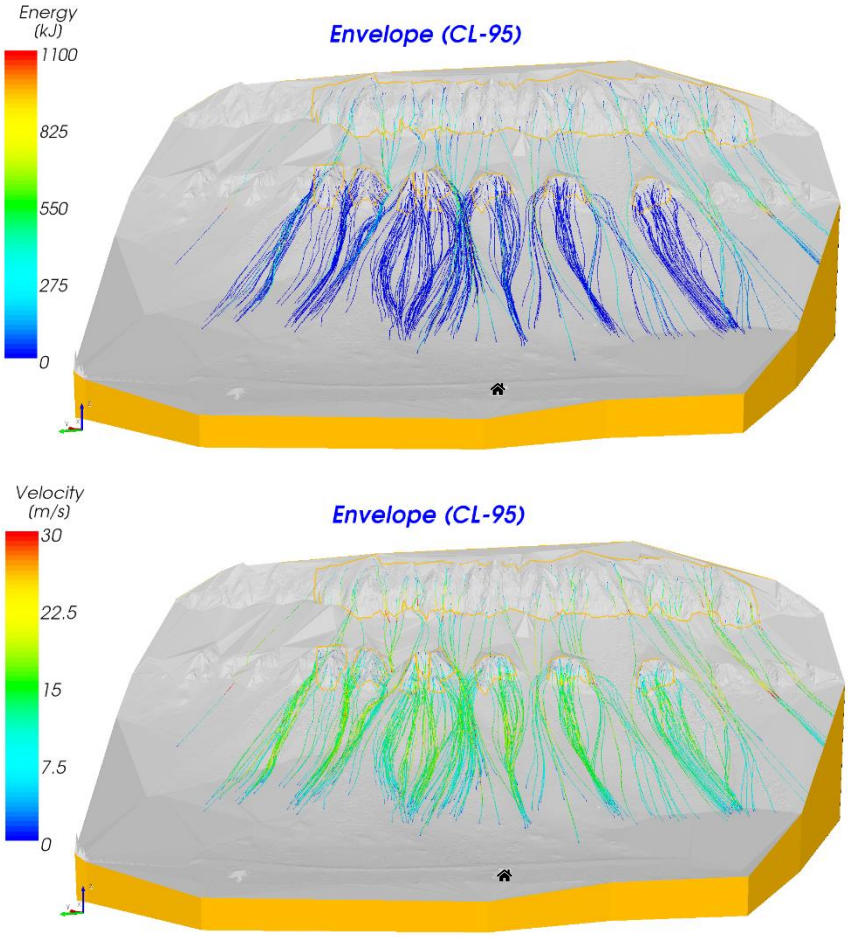

Figure 90 RocPro simulation results for warmer conditions, top kinetic energy bottom rock velocity

7.2. RAMMS Rockfall results and discussion

On a warmer environment the rock 1 scenario with soils that present softer behaviour the rocks as expected are stopped earlier than in the actual conditions which makes the future scenario safer than the actual conditions. In this case none of the trajectories land close to the cabin situation, despite this the maximum energy obtained is still 2400 kJ. this indicates that most of the energy is lost at the softest section of the slope which is located at the bottom which already has vegetable cover that could become more abundant in this scenario.

For rock 2 the situation is quite similar to the one on the present condition scenario as it was already a safe condition, regarding the energy the same applies than for the rock 1 case, the values obtained are similar.

Figure 91 and Figure 92 show the kinetic energy and velocity results respectively for a warmer environment, top for rock 1 and bottom for rock 2 in both cases

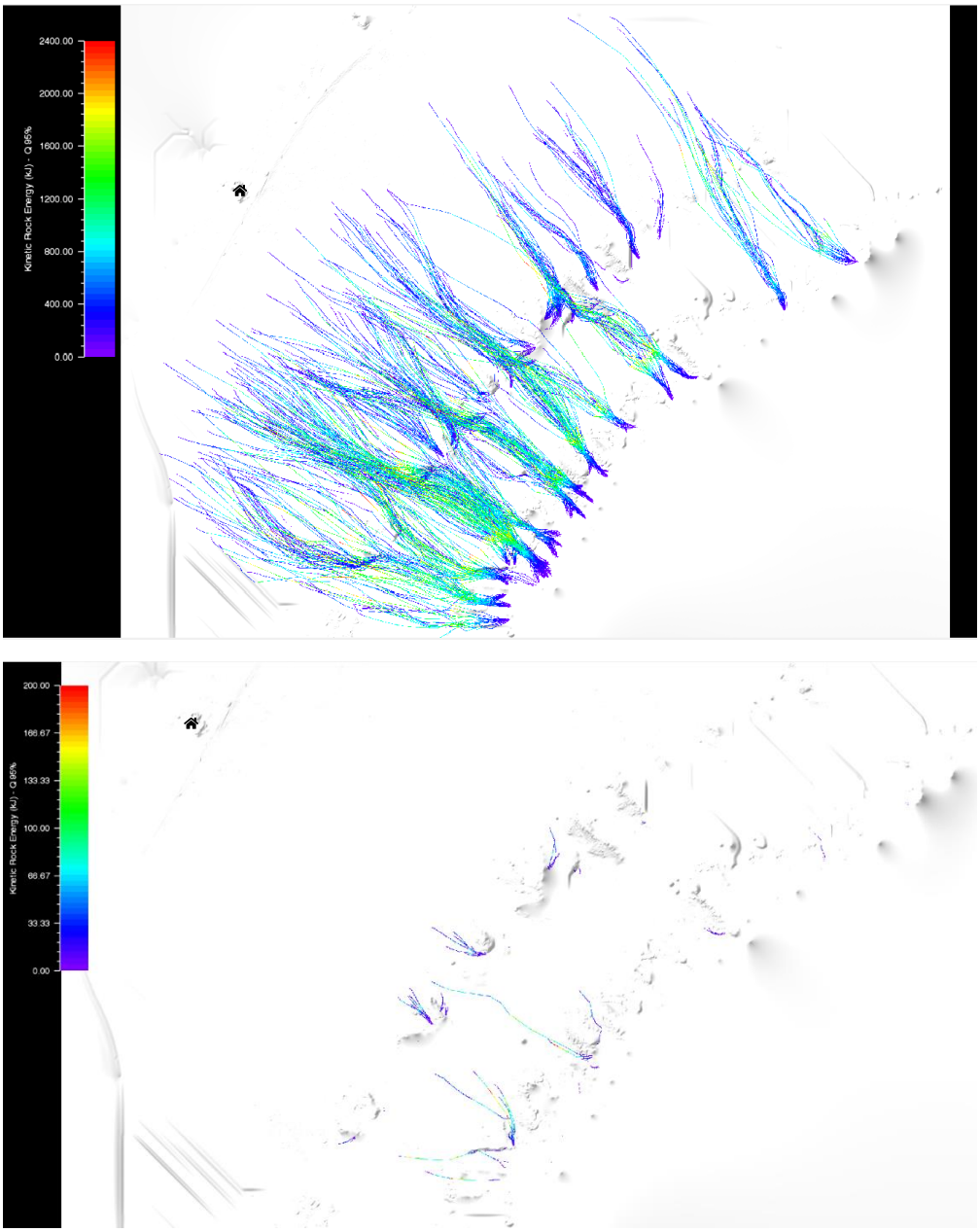

Figure 91 Rock kinetic energy for warmer conditions, on top simulation with rock 1 on the bottom simulation with rock 2

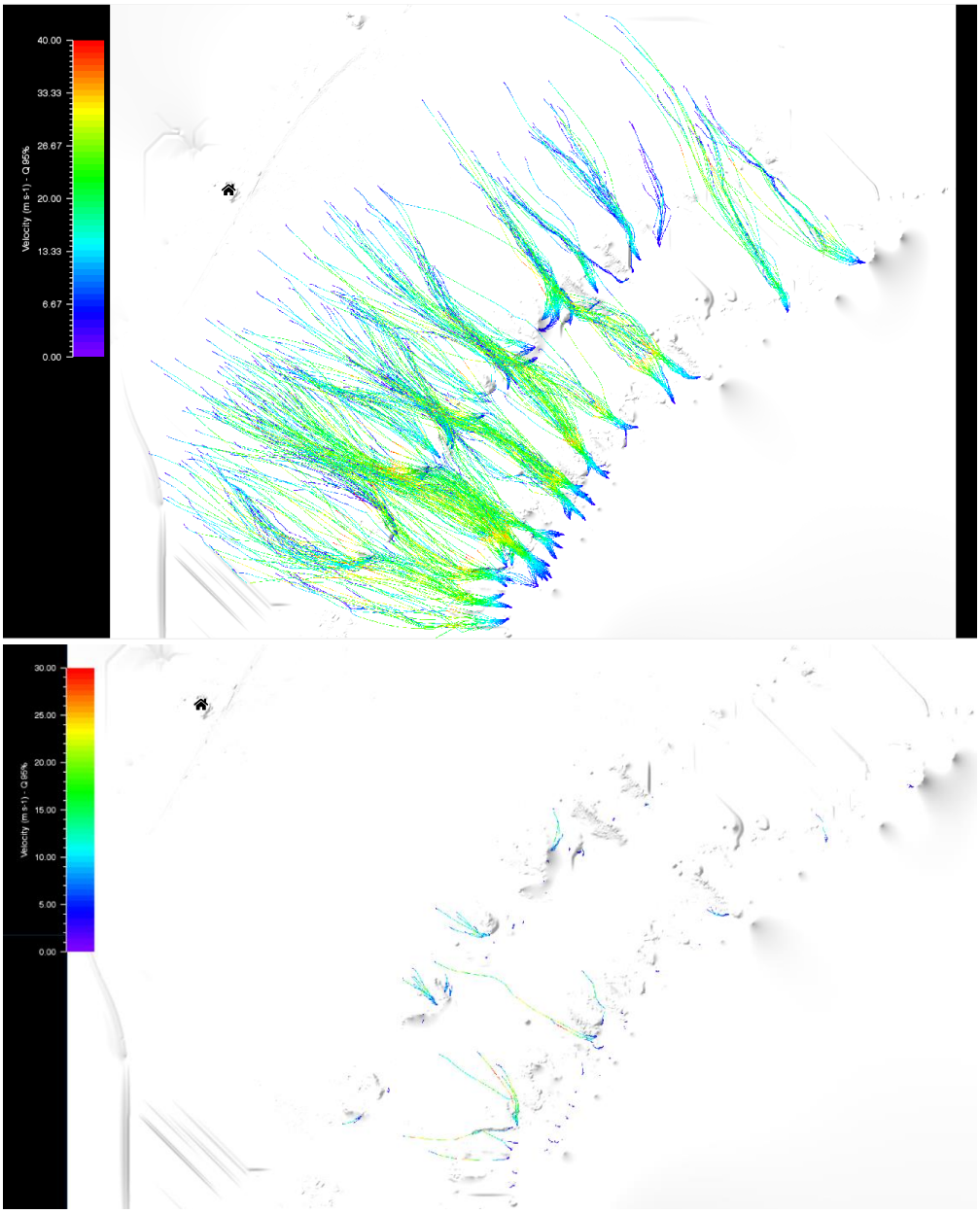

Figure 92 Rock velocity for warmer conditions, on top simulation with rock 1 on the bottom simulation with rock 2

7.3. Comparison between RocPro 3D and RAMMS Rockfall for warmer conditions

In the case of the future warmer scenario the results from RAMMS Rockfall and RocPro 3D become similar regarding the stopping points of the simulated trajectories. Despite this the same behaviour for the energy as in 5.3 is found in the warmer condition scenario.

For this case the assessment that can be obtained from both programs is similar, but is intriguing how comparing side by side the RAMMS results became affected in a greater way by the change in the soil type than RocPro and as a result both models became similar as shown in Figure 93.

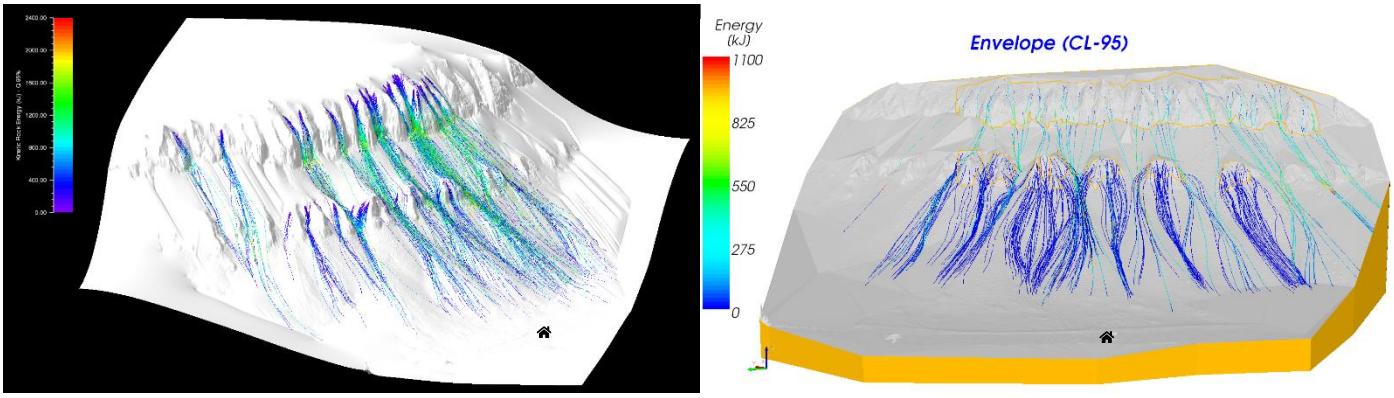

Figure 93 Kinetic energy results for RAMMS Rockfall on the left and RocPro 3D on the right for warmer conditions

8. Conclusions

From the conducted study the following conclusions can be obtained

- The outcrops studied that affect directly the Bamsebu cabin are stable under the present time conditions except the one located between 4 and 5, called 5 cent, which has a safety factor below the acceptable ones. At the same time this potentially unstable section presents the smallest rock pieces.
- Under a future scenario of warmer temperatures and higher groundwater presence all the analysed sections present safety factors below 1 in almost all the considered conditions representing a high risk of instability and consequent collapse.
- After the rockfall simulations has been found out that the mentioned cabin is located in an area susceptible of receiving an impact.
- Two types of rockfall events can be formulated, rare ones with heavy big boulders among the rock size composition, that represent a high consequence but low probability and frequent ones mainly comprised of small, light boulders which are not a threat to the cabin with high probability but low risk as their trajectories end close to the starting points at the base of the outcrops.
- The run out area of the rockfall events is dominated by the type of soil and characteristics of the rock itself. Under the present conditions the soil characteristics allows for the rare case events to represent a threat meanwhile under a future scenario the increase in softness of the soil due to a higher groundwater level and potentially more vegetable mass reduces the run out enough to reduce the risk substantially.
- With the obtained results, protection measures with a height of 2 metres and able to stand impact forces of 1100 to 1200 kJ can be taken around the cabin to reduce the risk of accidents.

References

Barton, N., Lien, R., & Lunde, J. (1974). Engineering Classification of Rock Masses for the Design of Tunnel Support. *Rock Mechanics*(6), 189-236.

Bo, L., Xinna, Y., Zihao, D., Zhihong, Z., Yingchun, L., & Qiang, Y. (2020). Shear strenght of rock fractures under dry, surface wet and saturated conditions. *Rock Mechanics and Rock Engineering*, 53: 2605-2622. doi: 10.1007/s00603-020-02061-y

Dershowitz, W. S. (1985, Jun 17). Rock joint systems. Massachusetts, USA. Retrieved from http://hdl.handle.net/1721.1/27939

Dorval, J.-G. (2020). *Confined compression test of Svalbard rocks.*

Duncan, C. W. (2018). *Rock Slope Engineering* (Fifth ed.). Boca Raton: CRC Press.

Evert, H. (2006). Shear strength of rock discontinuities. In E. Hoek, *Practical rock engineering* (pp. 1-14).

Hammah, R. E., Curran, J. H., Yacoub, T., & Corkum, B. (2004). Stability Analysis of Rock Slopes using the Finite Element Method. *EUROCK 2004 & 53 Geomechanics Colloquium.* Schubert.

Hoek, E., Carranza-Torres, C., & Corkum, B. (2002). Hoek-Brown criterion - 2002 edition. *Proceedings of the 5th North American Rock Mechanics Symposium and the 17th Tunnelling Association of Canada: NARMS TAC 2002*, *1*, pp. 267-273. Toronto.

Incorporated Research Instiurions for Seismology (IRIS). (2020, 07). *Iris Earthquake Browser (IEB).* Retrieved from Incorporated Research Institutions for Seismology: http://ds.iris.edu/ieb/index.html?format=text&nodata=404&starttime=1970-01-01&endtime=2025-01-01&orderby=time-desc&src=usgs&limit=400&maxlat=80.04&minlat=76.05&maxlon=34.51&minlon=-1.11&zm=6&mt=hyb

Kulatilake, P. H., Shreedharan, S., Sherizadeh, T., Shu, B., Xing, Y., & He, P. (2016). Laboratory Estimation of Rock Joint Stiffnessand Frictional Parameters. *Geological and Geotechnical Engineering.* doi: 10.1007/s10706-016-9984-y

Multiconsult. (2017). *Skredfarekartlegging Svalbard: Kartlegging av skredfare i hytteområder på.* Longyearbyen Lokalstyre, Longyearbyen.

Norsk Klimaservicesenter, Meteorologisk institutt. (2019). *Klimaprofil Longyearbyen.* Retrieved from https://cms.met.no/site/2/klimaservicesenteret/klimaprofiler/klimaprofil-longyearbyen/_attachment/14742?_ts=16a0bec6e90

Norwegian Polar Institute. (n.d.). Retrieved from https://geodata.npolar.no/arcgis/rest/services/Basisdata/NP_Ortofoto_Svalbard_WMTS_25833/MapServer/WMTS/1.0.0/WMTSCapabilities.xml

Norwegian Polar Institute. (2007). *Geology of Svalbard.* Tromso: Norwegian Polar Institute.

Oyanguren, P. R., & Monge, L. A. (2004). *Mecánica de rocas: fundamentos e ingeniería de taludes.* ETSI Minas.

RocPro 3D. (2019, May 1). RocPro 3D User's guide.

Rocscience. (2004). A New Era in Slope Stability Analysis: Shear Strenght Reduction Finite Element Technique. RocScience. Retrieved July 2020, from https://www.rocscience.com/documents/pdfs/uploads/7686.pdf

Rocscience. (n.d.). Phase 2 help files.

Romana, M. (1991). SMR classification. *Proceedings - Seventh International Congress on Rock Mechanics*, *2*, pp. 955-960. Aachen.

Rosenblueth, E. (1975). Point estimates for probability moments. *Proceddings of the Natural Scademy of Sciences USA, 72*(10), 3812-3814. Retrieved from https://www.pnas.org/content/pnas/72/10/3812.full.pdf

Rubensdotter, L. (2015). *Landforms and sediments: Bjorndalen-Vestpynten, Svalbard.*

SLF/WSL. (2016). *User manual V 1.6 Rockfall.*

Statens Vegvesen. (2018). *Vegbygging N200.* Vegdirektoratet. Retrieved from https://www.vegvesen.no/_attachment/2364236/binary/1269980?fast_title=H%C3%A5ndbok+N200+Vegbygging+%2810+MB%29.pdf

Viejo, D. (n.d.).

ANNEX 1

Chapter 1
Test and design of a shaking table for improvement of the sorting of coal

Contents

Table of figures

1. Introduction to sorting and concentration methods

In the mining industry different sorting and concentration methods are used depending on the type of mineral that is extracted. Regarding this master thesis only the ones used in the coal industry are going to be presented.

Sorting of coal can follow to different ways being these dry and wet, in the following sections the different methods will be explained in detail

1.1. Wet procedures

1.1.1. Trommel

A trommel screen is a type of rotary screen which consists of a cylinder, which is surface is covered of screens of different opening sizes from finer on the inlet to coarser on the outlet, to allow the material to travel along the cylinder it has a downwards slope. Figure 1 presents a trommel with a spiral design on the inside to help the movement of the material during operation.

Figure 1 Trommel (Trelleborg n.d.)

The best use case for this equipment is to separate fractions between 50 and 5 mm (Society for Mining, Metallurgy and Exploration (US) 2011).

At the moment of designing a trommel the following parameters have to be taken into account regarding the machinery

- Critical velocity: related with the centrifugal force created by the rotative motion, it is the speed at which the material starts sticks to the walls of the trommel. It is obtained through equation 1

$$V_c = \frac{42.7}{D^{0.5}} \quad (1)$$

  With D the diameter of the feeding material for the trommel

- Retention time: determines how long the material will stay in the trommel, this has a direct impact on the efficiency of the sorting but at the same time a longer travel time diminish the capacity per

hour. Increasing the slope or pitch angles (if using a trommel with an inner screw system) raises the retention time

- Slope: increasing the slope keeping the amount of ore constant, reduces the thickness of the layer thus increasing the effectives of the screening and at the same time increasing the production
- Diameter: the larger the diameter the bigger the production

For the material its moisture, granulometry and bulk density are the characteristics needed, a high water content could make the material prone to block the holes of the screen, the granulometry is needed to adjust the speed of the trommel and to know the screen sizes necessary, the bulk density is need to dimension the trommel according to the amount of material that is going to be fed.

1.1.2. Jig

It is a type of differential acceleration classification method, a Jig action is based on keeping the mineral in suspension on a fluid that is put through a pulsing movement, as a result the light materials float and the heavy sinks to the bottom. The fluid can be air, pneumatic jigs, or water, hydraulic jigs.

Instead of the fluid being pulsed the first jigs (Hancock and ROM) contained a mobile screen inside the tank that separated between both materials while moving. This system has been phased out and substituted by the pulsating fluid, Denver and Horz for water and Baum for air. Using Figure 2 the parts of a jig can be described

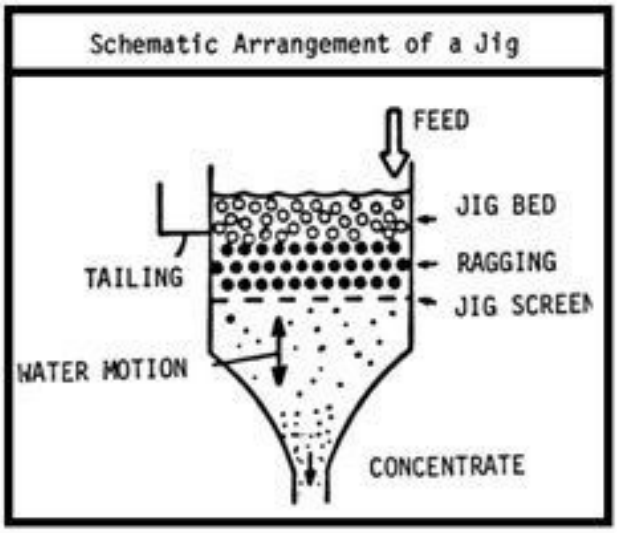

Figure 2 Schematic arrangement of a Jig (911 Metallurgist 2016)

- Jig Bed: layer formed by the raw material
- Ragging: first sorting layer composed regularly by steel balls, the density of the ragging should be between the mineral that wants to be recovered and the tailings. The size should be large enough to not block the screen below but not too big to impede the agitation during the pulsating phase
- Screen: last step to separate by size.

The ragging and the screen correspond to the English and German methods to extract the sank fraction, they can be used separately or combined. In Figure 3 different models of jigs are displayed

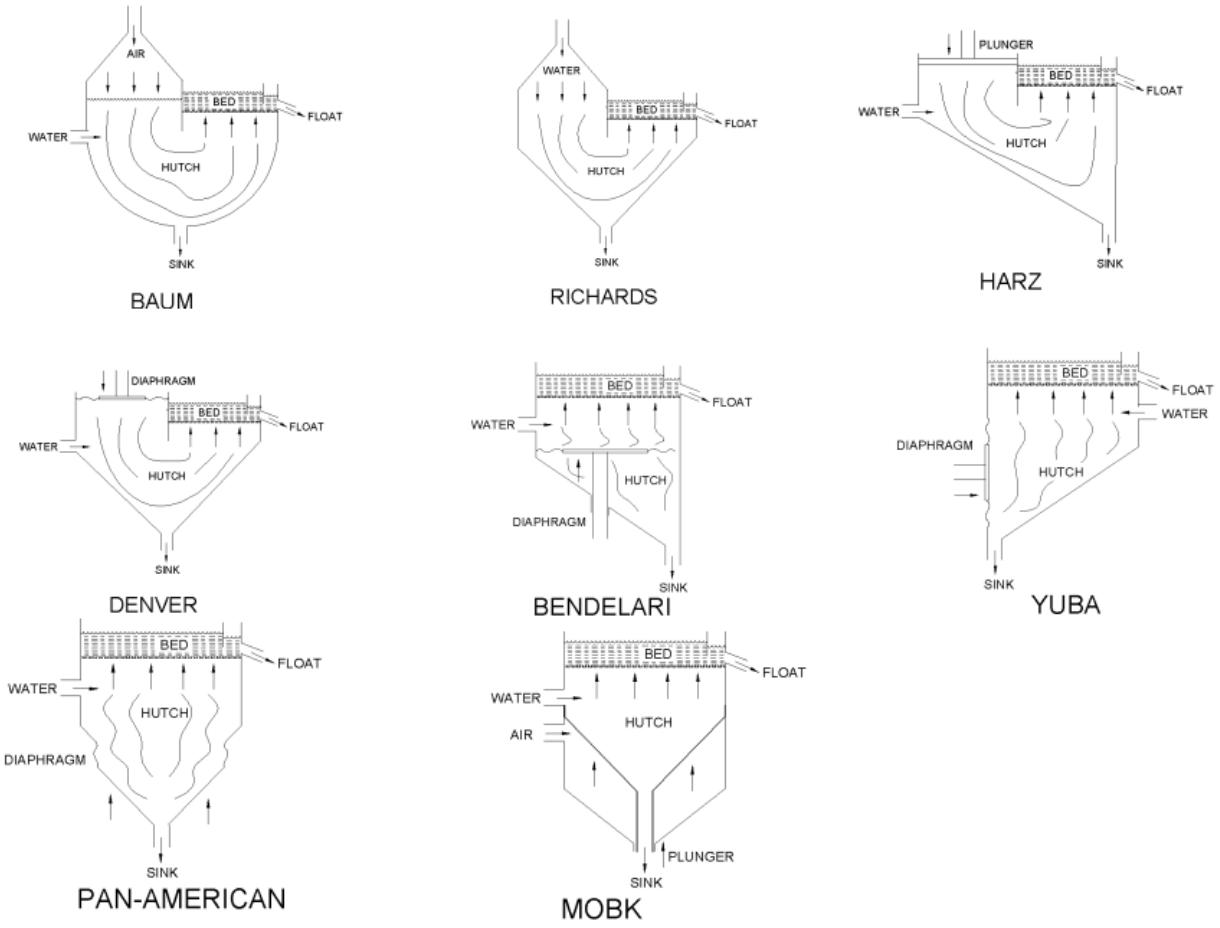

Figure 3 Models of Jig (911 Metallurgist 2016)

1.1.3. Shaking table

Also called Wilfley table, concentrating tables or shaking tables are very efficient separating concentrates coming from other steps.

They are comprised of a rectangular flat table that is tilted between 15 to 20 ^{o} horizontally. The table possess a series of riffles placed along its length. The table is moved in the longitudinal direction.

The material is fed from the top corner, see Figure 4, in the form of a slurry between 25 to 35 % in solids, the particles are transported due to the water flow down the slope. Heavy materials are trapped in the riffles and travel longitudinally to be collected at the high gravity section (Figure 4). Light materials are washed by the water flow going over the riffles and being collected at the low gravity minerals section (Figure 4)

The parameters when operating a shaking table are related to the placement and geometry of the riffles, water flow, deck slope and the amplitude and frequency of the motion, large particles need big amplitudes with low frequencies being the opposite for small particles. The effectiveness of the procedure is assessed by visual inspection

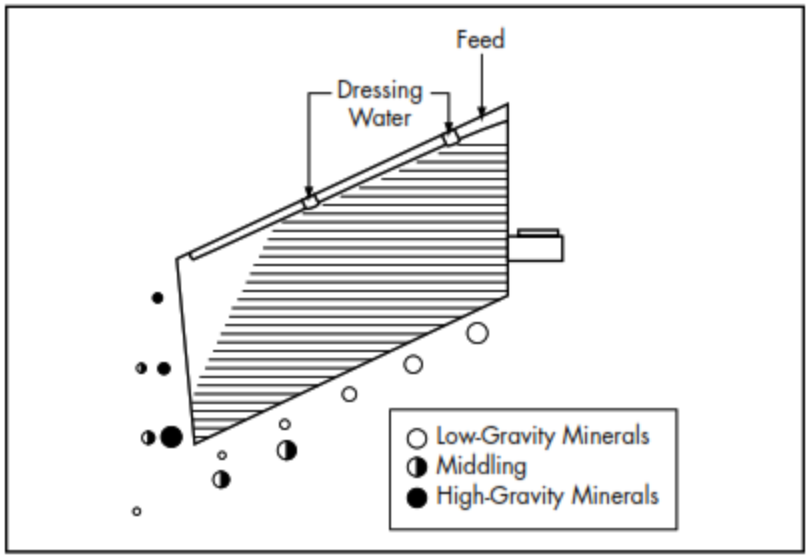

Figure 4 Scheme of a shaking table with materials classification. (Society for Mining, Metallurgy and Exploration (US) 2011)

Due to the relatively easy construction of this type of system, it has been selected to perform laboratory test to check its feasibility under arctic operations with the raw material extracted from mine 7. Due to the operational environment the fluid used to fluidize the bed will be compressed air. This variant was developed to be used in arid regions and has been used to separate materials like asbestos and vermiculite. (Society for Mining, Metallurgy and Exploration (US) 2011)

1.1.4. Heavy medium:

One of the most employed methods specially on the coal industry. It is based on suspending the raw material on a fluid with a density between the gangue and the ore.

Depending on the characteristics the mineral will be collected on the overflow or at the bottom of the tank.

This system can work by gravity or by centrifugal force. The gravity systems can be static or mobile, Wemco cone being static with the sank fraction being collected by suction and the Wemco drum being mobile and the most extended it also has higher capacities due to work with larger diameters. Centrifugal systems use cyclones to obtain a smaller cutting point, this is due to the increase in density of the medium as a result of the centrifugal force.

The mediums used at the industry are magnetite, used by SNSK at the Svea mine, and ferrosilicon. As regular dense mediums solutions used for lab tests are toxic industry uses water based solutions.

Heavy mediums present drawbacks when sorting particles finer than 100 µm even when using centrifugal equipment as a high presence of fines increases the turbidity of the dense medium.

The calculation of the effectiveness of the method before any tests, is done through the employment of the partition curve also called performance or Tromp curve which shows the probability of a particle with an specific gravity (SG) to go to the concentrate outlet. To compare between operations with different equipment the following equations have been developed

$$E_p = \frac{1}{2}(SG_{75} - SG_{25}) \quad (2)$$

$$I = \frac{E_p}{(SG_{50} - 1)} \quad (3)$$

$$SI = \frac{SG_{75}}{SG_{25}} \quad (4)$$

E_p is the probable error, SG is the specific gravity, I is the imperfection and SI being the sharpness index, 25, 50 and 75 are the specific gravities at which that percentage of material will go into the concentrate stream. In Figure 5 are shown the performance curves for a gravity heavy medium separator.

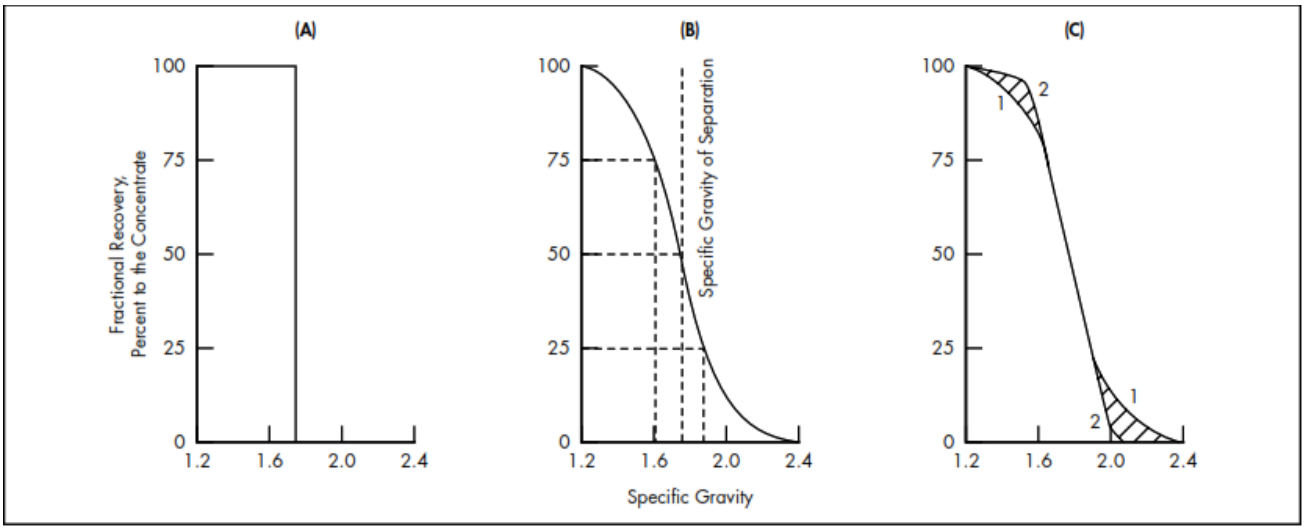

Figure 5 Performance curves of a gravity separator. Partition curves: (A) perfect separation, (B) actual separation (curve 1),and (C) same Ep as B but with superior recovery of misplaced particles (shaded area between curves 1 and 2) Aplan 2003 cited in (Society for Mining, Metallurgy and Exploration (US) 2011)

1.2. Dry procedures

1.2.1. XRD and XRF

Based on the principle of the absorption or the fluoroscopy of a beam of X rays when it crosses and interacts with the particles of the material. XRD classifies based on the density of the different materials to be sorted out meanwhile XRF classifies based on composition, as coal is almost pure carbon it is easy to detect among the gangue which will have also parts of coal in it but on a much lower quantity then adjusting the cutting law determines the concentrate and rejected fractions. Coal is lighter than the matrix that surrounds it which is how the density separation works.

On an industrial scale this procedure is done on a continuous way with multiple scanners placed on the machine that test the material on the conveyor belt and at the end of the stream a series of air jets, ejects the gangue particle from the stream during the free fall at the exit point of the machine. Shows an XRD device from the company Steinert

Figure 6 Steinert XSS T (STEINERT GmbH 2020)

1.2.2. Air dense medium fluidized bed

This process is an evolution of the traditional water based dense medium already explained. In this process the medium is a mix of dense material, magnetite powder, fine coal powder as the separating medium and the raw fed material.

The mixture is keep on suspension by an air flow instead of water. The parametres of operation are the air velocity, bed height, coal to magnetite ratio and residence time.

To work with fractions under 6 mm two modifications had been researched: vibrations on the bed developed by (ZF, MM and Zhao YM 2008) which creates microbubbles that separate effectively the finer fractions of coal. Or magnetically stabilized dense medium, on this ones the magnetite is controlled by an external magnetic field that allos the creation of air channels on the bed increasing the stability of the bed density and lowering the pressure fluctuation.

1.2.3. FGX and air table

These systems are based on the same principles as the wet shaking tables. The main difference between a FGX and Air table is the shape of the vibrating table. FGX systems have a table that narrows down towards the opposite side of the feeding port where the reject product is classified, meanwhile an air table has the same dimensions on all the sides, this difference is portrayed in Figure 7. Both of them use a flow of compressed air to fluidize and mobilize the bed of material, displacing the lighter materials to the top of the bed, meanwhile the heavier ones stay in contact with the table surface. The light materials travel following the slope of system meanwhile the riffles stops the movement down the slope of the heavy materials making them move on the direction of the shaking.

The parameters to adjust are the same that on a wet shaking table, slope angle, tilting, amplitude and frequency of the vibration and air flow.

The material obtained is separated in product, fine light particles, midligns, and reject.

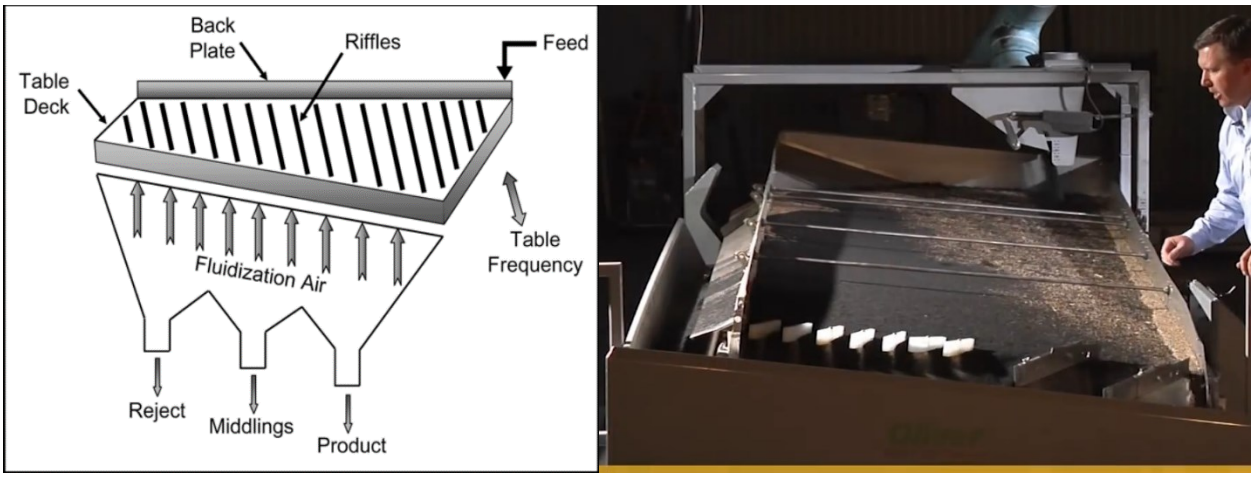

Figure 7 on the left scheme of a FGX system (R.Q.Honaker, et al. 2008), on the right an air table (Oliver Manufacturing CO Inc 2020)

1.2.4. Triboelectrostatic

Triboelectrostatic separation works by how the material particles react to electrical currents. It is only useful for small particle sizes 50µm to 1 mm.

The particles are charged by various physical processes, induction, conduction, friction and coronal effect (convection). This creates two types of machines electrostatic and electrodynamic.

All the devices consist of an electrode that provides the electric charge and a ground connection. In the case of the corona effect the electrode as a point finish with a maximum voltage of 50kV that ionizes the surroundings and charges the particle.

Electrodinamic machines has the electrode and a rolling drum connected to ground, non conductive particles stick to the drum meanwhile conductive particles separate due to the inertia force at the end of the drum. Its performance can be improved by incorporating a negative electrode that attracts the positively charged conductive particles. Extra fine conductive particles are not throwed away due to the low centrifugal force generated and are carried away by the non conductive fine particles.

Electrostatic machines had been use for a long time specially to clean exhaust gases, the particles are charged on a chamber before entering the filter were the walls are electrically charged and the particles stick to them during a free fall, see Figure 8.

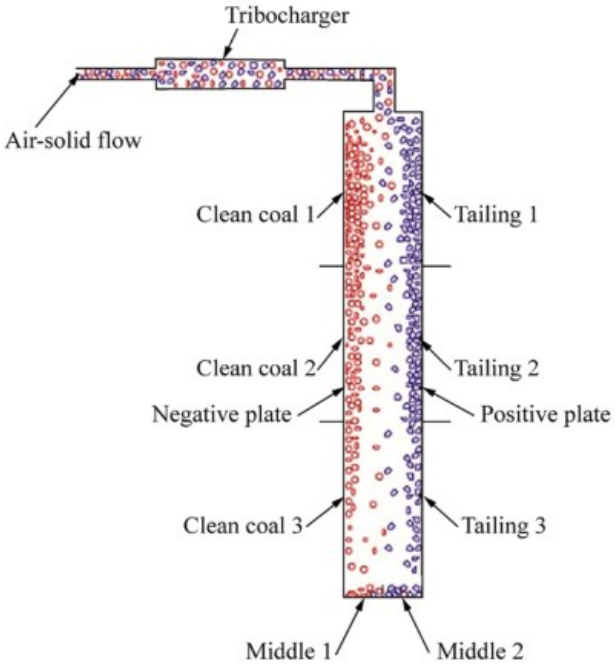

Figure 8 Scheme of an electrostatic separator (Zhang et al. 2009 cited in (Zhao, et al. 2014)

2. Methodology

Due to the nature of this master thesis project, the allocated timeframe and the arctic location of Longyearbyen, where the tests take place, which complicates shipping materials. It was decided to perform two different techniques, an XRF analysis of a coal sample from mine 7 with different percentages of gangue material and the construction of an air shaking table due to its simplicity and the available pieces from a similar motion mechanism available at NTNU.

The purpose is to find out the effectivity of these two techniques for the material extracted to obtain the required product, and check is suitability under arctic operation conditions.

2.1. XRF Analysis:

The analysis was performed with a portable Niton XL3 XRF analyser from Thermo Scientific, see Figure 9.

Figure 9 Niton XL3 XRF handheld analyzer (Thermo Scientific 2011)

4 different samples were tested with different percentages of ash richness. To prepare the test samples SNSK provided two raw samples of material one rich in gangue, no processing, and another one with a 3.4% content of gangue, cleaned. The tested samples had a total mass of 10 grams each and the percentages of ash richness were 90, 75, 50 and 30 %

The samples were prepared by weighting each fraction required for the mix, then both fractions were introduced on a glass jar and shook during 30 seconds on a circular motion to achieve good mixing while reducing upward projections of the powder.

To analyse the samples, plastic capsules were filled with the powder until the edge of the capsule equalling an amount of 7 g ±1 g as there are minor variations while filling the capsule. Each capsule was then placed on a stand provided by the manufacturer of the equipment. The XRF device was placed under the capsules, the stand allowed for safe and handsfree operation of the device improving the handling of the samples. The analysis performed was a mining profile including heavy elements.

On Table 1 the samples, weights and percentages are summarized

Table 1 XRF sample parameters

Sample	Mass (g)		Percentage %
	Ash	Coal	
A	5	5	50
B	3	7	30
C	7.5	2.5	75
D	9	1	90

2.2. Air table design:

The design of the shaking table has been divided in 4 steps with the purpose of simplify it.

2.2.1. Air flow calculations

To identify the air flow required 5 random pieces of the biggest size observed on a sample of coal from the 20 mm fraction were selected. The pieces were measured to know their dimensions and obtain their volumes, the pieces and the measurements are presented on Figure 10.

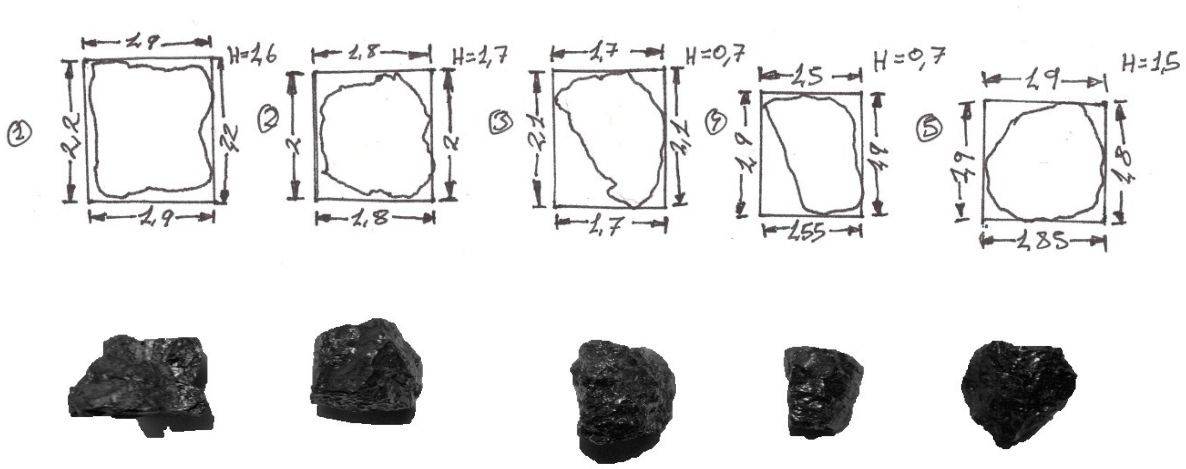

Figure 10 Sketches from the top view of the samples with dimensions measured, bottom picture photograph of each sample

With volumes identified and the density the mass of the sample pieces can be obtained. These calculations are made for all the samples but for the rest of the design the average volume will be used. For the density the average density for the coal extracted from the mine is used. The equation used is:

$$m = \rho * V \qquad 5$$

Being

ρ: density of the material

V: volume of material

The results of this calculation are presented on Table 2 below

Table 2 Mass of the coal samples

Sample	Length (m)	Wide (m)	Height (m)	Surface (m^2)	Volume (m^3)	Density (kg/m^3)	Mass (kg)
1	0.022	0.019	0.016	4.18E-04	6.69E-06	793	0.0053
2	0.02	0.018	0.017	3.60E-04	6.12E-06	793	0.0049
3	0.021	0.017	0.007	3.57E-04	2.50E-06	793	0.0020
4	0.019	0.0155	0.007	2.95E-04	2.06E-06	793	0.0016
5	0.0185	0.0187	0.015	3.46E-04	5.19E-06	793	0.0041
Average	0.0201	0.01764	0.0124	3.55E-04	4.40E-06	793	0.0035

Using the expression $F = m \times a$ *(6)*, the action of gravity on the samples can be obtained. This is the force that the airflow will have to counter in order to create the fluidized layer of air underneath the material. As before the calculations are presented on the following table

Table 3 Gravity action

Sample	Mass (kg)	Gravity (m/s^2)	Force (N)
1	0.0053	9.8	0.0519751
2	0.0049	9.8	0.047561
3	0.0020	9.8	0.0194207
4	0.0016	9.8	0.0160207
5	0.0041	9.8	0.0403277
Average	0.0035	9.8	0.0341677

To calculate the pressure that is needed to lift the pieces the previous results are used as inputs on the following equation

$$P = \frac{F}{S} \qquad 7$$

Where

P: pressure

F: force

S: surface

The Pressures obtained are on Table 4

Table 4 Pressure needed to lift the sample

Sample	Pressure
1	1.24E+02
2	1.32E+02
3	5.44E+01
4	5.44E+01
5	1.17E+02
Average	9.64E+01

The surface of the table is made from a perforated steel plate or from panels from the screen which is actually employed in mine 7, through this panels the compressed air will exit creating the fluidified layer. As the material has irregular shapes and mixed densities trying to find narrow values for equations 5 and 7. To overcome this the following assumptions have been made:

An amount of 2 kg of material on the table has been fixed.

During operation the surface of the table that is going to be covered by the material has been supposed as an 80 % of the total surface.

Working in this way the lift force needed is going to be kept constant with a value of 19.6 N using equation 8

$$W = g * m \quad (8)$$

Where W is weight, g force of gravity, m is mass.

The surface of the table where the material is going to be deposited corresponds to two panels with dimensions of 1 metre long and 0.35 m wide, they are placed one beside the other making a whole surface of 1 m long and 0.7 m wide, with a surface of 0.7 m^2. An 80 % covered equals to 0.56 m^2.

Using equation 7, the pressure needed to lift the weight generated by the load of 2 kg on the surface of 0.56 m^2. The result of this calculation is a pressure of 35 Pa.

The moment the compressed air enters the chamber of the shaking table its velocity and pressure changes due to the sudden change in the section that the fluid is travelling. This phenomenon is governed by equation 9

$$\Delta H = \frac{V_1^2}{2g} \times \left(1 - \frac{S_1}{S_2}\right)^2 \quad (9)$$

Where:

- ΔH change in pressure as a change in height
- V_1 speed of the fluid at section one
- g force of gravity
- S_1 surface of section 1
- S_2 surface of section 2

In Figure 11 the sections used for the calculation are represented. To calculate the speed of the fluid equation 10 has been used

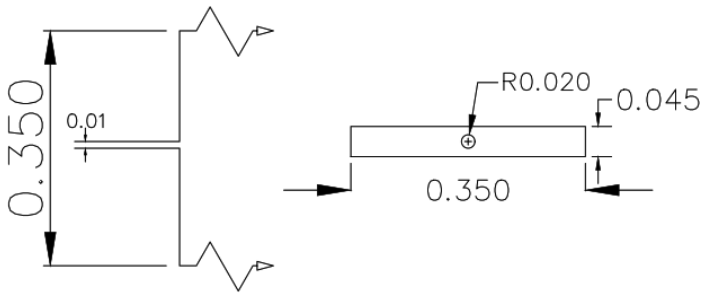

Figure 11 Top and front view of the chamber and air outlet

$$Q = V \times S \quad (10)$$

On Table 5 the values used for the different calculations and its results are presented

Table 5 Values for head loss calculations

Surface of section 1 (S_1)	0.00125 m^2
Surface of section 2 (S_2)	0.042 m^2
Flow rate (obtained from compressor specs)	0.00242 m^3/s
Speed at section 1 (V_1)	1.936 m/s

The head loss equals 0.18 m of height difference. To transform this into a pressure drop equation 11 is used.

$$H = \frac{P}{\gamma} \tag{11}$$

Where

- H height difference
- P pressure
- γ specific weight of the fluid

Because the specific weight is a function of the density of the fluid and it changes with temperature it must be calculated for the site where the equipment is going to be used. That value is obtained through equation 12 from (ISO 1975 (Revised 2007))

$$\rho(h) = \rho_0 \times \left(\frac{T}{T_0}\right)^{-1-\frac{g}{a \times R}} \tag{12}$$

Where

- $\rho(h)$ air density at altitude h
- ρ_0 density at the base of the atmospheric layer considered
- T temperature at the target altitude
- T_0 temperature at the base of the atmospheric layer considered
- g force of gravity
- a thermal gradient for the atmospheric layer (from ISO tables)
- R air constant

The inputs for the equation are:

- $\rho_0 = 1.225 \ \frac{kg}{m^3}$
- $T = 253 \ K$
- $T_0 = 288.15 \ K$
- $g = 9.8 \ \frac{m}{s^2}$
- $a = -6.5 \ \frac{K}{km}$
- $R = 287 \ \frac{m^2}{s^2 K}$

After calculating, the density of the air at mine 7 is $\rho = 1.394\ \frac{kg}{m^3}$. To obtain the specific weight equation 13 is used, with the density value calculated with expression 12

$$\gamma = \rho \times g \qquad 13$$

- $\rho = 1.394\ \frac{kg}{m^3}$
- $g = 9.8\ \frac{m}{s^2}$

The specific weight obtained is $\gamma = 13.66\ \frac{kg}{m^3}$

Going back to equation 11 the conversion to pressure gives a value of $P = 2.458\ Pa$

Adding the pressure drop to the pressure required to lift the load results in a requirement of 37.458 Pa at the table without considering other losses produced by manufacturing errors or not completely sealed gaps.

2.2.2. Sorting surface

The first approach was to make the upper surface made of the same panels that mine 7 uses on its banana screen, but after examining such panels, see Figure 12, they were found to be too thick and heavy for the intended purpose, the extra mass will require a bigger motor than the one easily available, the extra thickness will increase, by a small amount, the air requirements and the mounting system for the panels will require a little bit more complex construction of the sliding section on top of the air box to accommodate the mounting points of the panels.

Figure 12 From left to right, detail of front and underside of the screen panels, side view of the screen panel and detail of the perforated net.

Due to this concerns it was decided to switch to a simple perforated steel plate of 1 to 2 mm in thickness, and a size of 1 by 2 metres with the same pattern as the panels in Figure 12, this steel plate has been manufactured at the NTNU workshop in Trondheim.

On top of the plate a series of riffles will be installed, its function is to provide a “pocket” for stratification of the material to take place along its travel on the shaking table. These riffles, Figure 13, will be tested with different slant angles in respect to being parallel to the shaking motion of the table, regarded as angle 0.

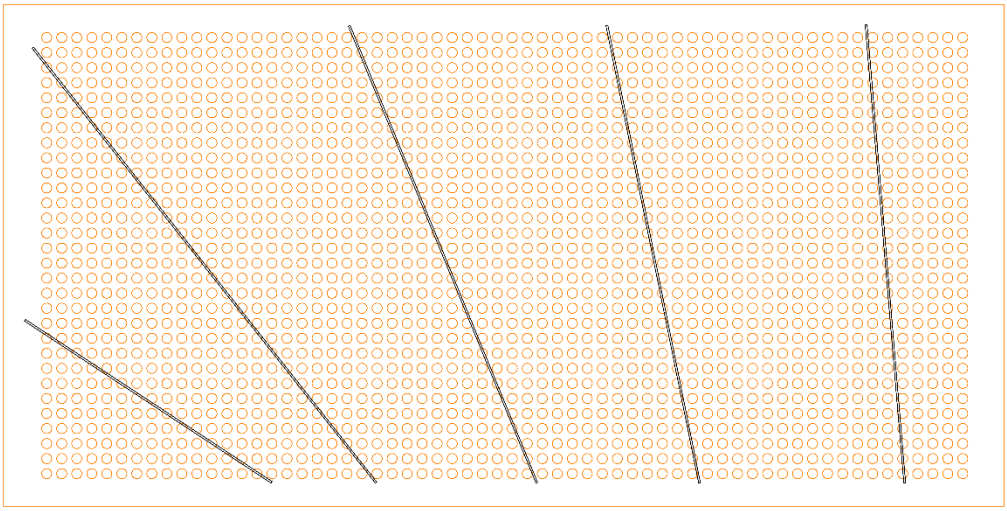

Figure 13 Proposed position for the riffles on the surface of the shaking table

The riffles will be attached by point welding them to the surface of the steel plate

The steel plate is attached mounted on bearings that provide the ability to move on top of rails with minimal friction.

The steel used is quality S-235 in JR grade. To make the exterior frame on which the rest of the machine is built upon square steel profiles of 4x4 mm have been used, the steel characteristics are the same than for the table section.

2.2.3. Air box

The air requirements calculated in section are employed using an air box. This consists of a section of folded steel plate with the same characteristics as the one used for the sorting surface. The shape can be seen in Figure 14

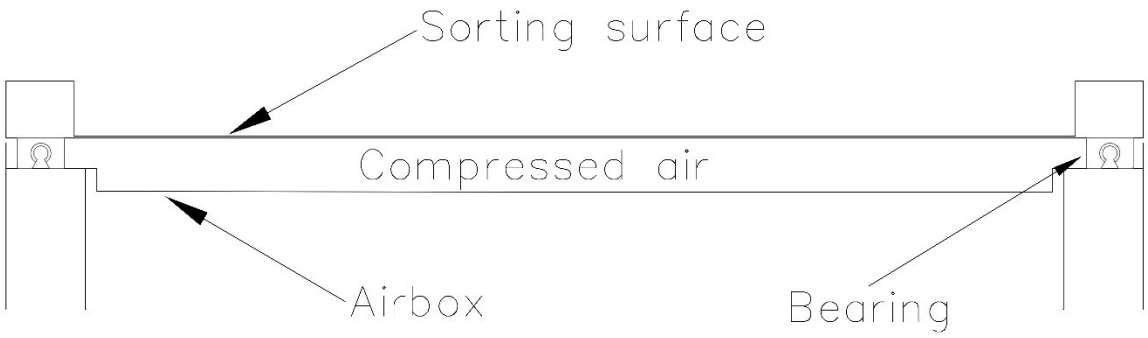

Figure 14 front view for the airbox and sorting surface

The box will be closed and the contact between the box and the sorting surface will be sealed with grease or other similar compound to reduce the air losses and the mechanical friction.

The airbox is fixed in place with the rails for the sorting surface movement on its edges to reduce as much as possible the interaction between the air flow and such rails that could create unexpected and unwanted turbulences.

2.2.4. Motor selection

The motor used in the assembly has to be able to move the mass of the upper part or the table, the air box is fixed and the table slides on top of it, at different frequencies and amplitudes.

The dead mass that the motor has to move is the combination of the amount of material to be sorted, 2 kg, the sorting surface and the frame that holds it and allows its movement on the already mentioned bearings.

The sorting surface is a perforated steel plate of 100 cm length and 200 cm wide with 0.1 cm in thickness. For easiness of calculations and to have some margin while selecting the engine the mass of the plate is calculated as it is a solid piece with no perforations. As the plate is a rectangle the volume can be obtained with equation 14

$$V = b * h * t \quad 14$$

Where b is base, h is height and t is thickness. The volume of the plate equals 3000 cm^3. To obtain the mass the volume has to be multiplied by the density of the steel used, this steel is DIN standard 1541 with a density of 7.8 g/cm^3 obtaining a mass of 15.6 kg

The frame is made of two square shaped steel tubes, of 1 m length, 2 cm square side and a thickness of 2mm, the manufacturer provides the mass of this tubes which is 2 kg/m which adds up to a total of 4 kg.

The total mass that the engine will have to move equals to 21.6 kg.

To size the engine, calculating the needed torque is required. The equation used is

$$Torque = weight * radius \quad 15$$

The eccentric displacement on the table is 20 cm, thus the radius is 10 cm or 0.1 m. The weight is a result of using eq Using *the expression* $F = m \times a$ (6), being 211.68 N. Calculating eq 15 gives a result of 21.168 N*m

3. Results

3.1. XRF Analysis

The XRF analysis were performed to check if the material has enough difference between the elements that compose it to make viable the usage of an XRF sorting device. It is necessary to point out that the way this test was carried and the form in which the material was tested doesn't represent how this technique, or XRD as extension, are used in industry production grade detectors. The main difference being the particle size, the test was done with powder. On a rock form is easier to separate between what is pure gangue, pure coal or a mixture that will require further, in powder both materials are mixed and detected easily even when not intended.

The amounts detected of each element and its error values on the analysed samples are presented Table 6 and in Figure 15.

Table 6 XRF analysis results for four different samples and the two references.

Sample	Si	Si Error	S	S Error	Al	Al Error	Ca	Ca Error	Mg	Mg Error
ash rich	190384	1264.460	6828.49	117.52	47111.1	1030.51	890.24	157.93	<LOD	1245.04
mix d 90 % ash	163443	1153.820	7881.98	123.83	36871.5	907.07	1567.44	161.97	3574.85	1529.76
mix c 75 % ash	126777	997.510	10277.7	141.28	28875.8	779.4	2713.37	179.44	1693.07	1033.83
mix a 50 % ash	77785.7	701.370	12785.67	142.89	15738.9	512.09	4359.83	199.24	<LOD	2297.04
mix b 30 % ash	45393.5	532.080	14424.44	153.9	8690.62	400.92	6573.72	230.3	3169.32	1356.68
coal rich 3.4 % ash	1904.2	141.650	17080.81	169.51	1140.36	201.13	9711.83	266.6	<LOD	3300.46

The gangue composition is mainly silicon and aluminium meanwhile the coal fraction will contain sulphur and calcium, this will be the criteria for a possible classification.

As seen on the graph as the ash fraction reduces in each sample the Si and Al diminish on an almost linear decrease as shown by the black for silicon and red line for aluminium. Regarding sulphur and calcium is not until the mixture reaches a 75 % of ash content that changes can be seen.

On Table 7 the changes of each element in percentage have been calculated in regard of the previous sample

Table 7 Percentage of change for the different elements

Sample	Si change	S change	Al change	Ca change
from ash rich to d	-14.15%	15.43%	-21.73%	76.07%
from d to c	-22.43%	30.39%	-21.69%	73.11%
from c to a	-38.64%	24.40%	-45.49%	60.68%
from a to b	-41.64%	12.82%	-44.78%	50.78%
from b to coal rich	-95.81%	18.42%	-86.88%	47.74%

Despite the reduction in each step, which represents possible different extracted material scenarios, the mixture with a 30 % of ash in its composition still presents a high quantity of gangue materials which could

make difficult the identification by the system, resulting in false positives thus raising the discarded amount of material that could need recirculation.

As a way to improve the sorting, thresholds of different elements on the analysed rock piece can be stablished not only focusing on the gangue or the coal but on the ratio between different elements narrowing down the classification and obtaining a finer fraction.

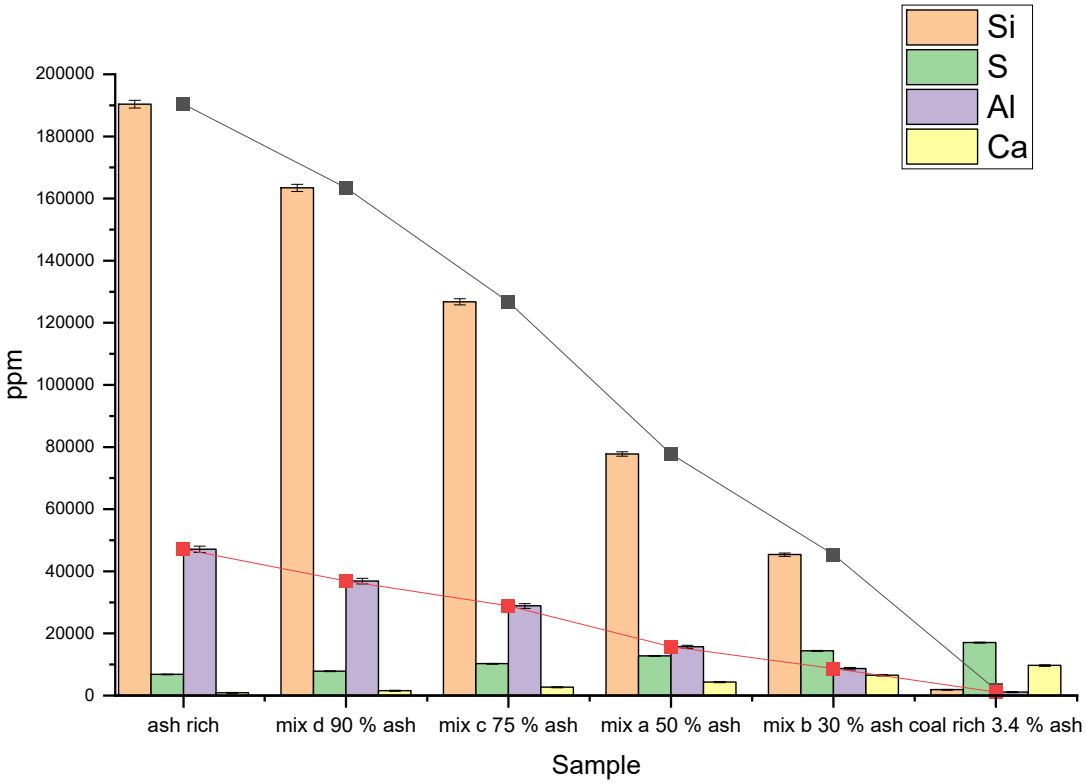

Figure 15 Contents of Si, S, Al and Ca in ppm for the analysed samples.

References

911 Metallurgist. 2016. *Gold Jig & Mineral Processing Jig.* 911 Metallurgis. 12 01. Accessed 03 2020. https://www.911metallurgist.com/blog/gold-mineral-processing-jigs.

F.Rojas, Andrés, and Juan M. Barraza. 2010. "DISTRIBUCIÓN DE MINERALES EN DOS CARBONES DEL SUR-OCCIDENTE COLOMBIANO USANDO SEPARACIÓN CICLÓNICA Y OXIDACIÓN A BAJA TEMPERATURA / MINERAL DISTRIBUTION IN TWO SOUTH-WEST COLOMBIAN COALS USING CYCLONE SEPARATION AND OXIDATION AT LOW TEMPERATURE." *DYNA* 77 (162).

ISO. 1975 (Revised 2007). *ISO 2533: Standard Atmosphere.* ISO.

Mariño, David Viejo. 2013. "Notes on minerallurgy course BSc on Mining Engineering." Madrid.

Oliver Manufacturing CO Inc. 2020. *Products: Gravity separator.* Accessed 04 2020. https://www.olivermanufacturing.com/all-products/?product_cat=gravity-separator.

R.Q.Honaker, M. Saracoglu, E. Thompson, R. Bratton, G.H. Luttrell, and V. Richardson. 2008. "Upgrading Coal Using a Pneumatic Density-Based." *International Journal of Coal Preparation and Utilization* 28 (1): 51-67.

Richards, Robert H. 1909. *A text book of Ore Dressing.* 1st. Massachusetts: McGraw-Hill Book Company.

Society for Mining, Metallurgy and Exploration (US). 2011. *SME Mining Engineering Handbook.* 3rd. Society for Mining, Metallurgy and Exploration, INC.

STEINERT GmbH. 2020. *X-RAY SORTING SYSTEMS.* STEINERT GmbH. Accessed 03 15, 2020. https://steinertglobal.com/magnets-sensor-sorting-units/sensor-sorting/x-ray-sorting-systems/.

Thermo Scientific. 2011. *Portable Material ID & Surface Analysis › Niton™ XL3t XRF Analyzer.* Accessed April 2020. https://www.thermofisher.com/order/catalog/product/10131166?SID=srch-hj-10131166#/10131166?SID=srch-hj-10131166.

Trelleborg. n.d. *Screening systems.* Trelleborg. Accessed 03 2020. https://www.trelleborg.com/engineered-products/~/media/engineered--products/solutions--and--products/screening--systems/trommel--panels/1024--trommel--panels.jpg.

ZF, Luo, Fan MM, and Tao XX, Chen QR, Chen Z Zhao YM. 2008. "Density dependent separation of dry fine coal in a vibrated fluidized bed." *Powder Technol* 187 (2): 119-123.

Zhao, Yuemin, Xuliang Yang, Zhenfu Luo, Chenlong Duan, and Shulei Song. 2014. "Progress in developments of dry coal beneficiation." *International Journal of Coal Science and Technology* 1 (1): 103-112.

ANNEX 2

Table 1. Descriptions and Ratings for the Parameters RQD, J_n, and J_r

1.	ROCK QUALITY DESIGNATION (RQD)		
A.	Very poor	0— 25	Note:
B.	Poor	25— 50	(i) Where RQD is reported or measured as ≤ 10 (including 0) a nominal value of 10 is used to evaluate Q in Eq. (1)
C.	Fair	50— 75	
D.	Good	75— 90	
E.	Excellent	90—100	(ii) RQD intervals of 5, i. e. 100, 95, 90, etc. are sufficiently accurate
2.	JOINT SET NUMBER	(J_n)	
A.	Massive, no or few joints	0.5—1.0	
B.	One joint set	2	
C.	One joint set plus random	3	
D.	Two joint sets	4	
E.	Two joint sets plus random	6	
F.	Three joint sets	9	
G.	Three joint sets plus random	12	Note:
H.	Four or more joint sets, random, heavily jointed, "sugar cube", etc.	15	(i) For intersections use $(3.0 \times J_n)$
J.	Crushed rock, earthlike	20	(ii) For portals use $(2.0 \times J_n)$
3.	JOINT ROUGHNESS NUMBER	(J_r)	
	(a) *Rock wall contact* and (b) *Rock wall contact before 10 cms shear*		
A.	Discontinuous joints	4	Note:
B.	Rough or irregular, undulating	3	(i) Add 1.0 if the mean spacing of the relevant joint set is greater than 3 m
C.	Smooth, undulating	2	
D.	Slickensided, undulating	1.5	
E.	Rough or irregular, planar	1.5	
F.	Smooth, planar	1.0	(ii) $J_r = 0.5$ can be used for planar slickensided joints having lineations, provided the lineations are favourably orientated
G.	Slickensided, planar	0.5	
	(c) *No rock wall contact when sheared*		
H.	Zone containing clay minerals thick enough to prevent rock wall contact	1.0 (nominal)	
J.	Sandy, gravelly or crushed zone thick enough to prevent rock wall contact	1.0 (nominal)	

Table 2. Descriptions and Ratings for the Parameters J_a and J_w

4.	JOINT ALTERATION NUMBER (J_a)		φ_r (approx.)	
	(a) *Rock wall contact*			
A.	Tightly healed, hard, non-softening, impermeable filling i. e. quartz or epidote	0.75	(—)	Note: (i) Values of $(\varphi)_r$ are intended as an approximate guide to the mineralogical properties of the alteration products, if present
B.	Unaltered joint walls, surface staining only	1.0	(25°—35°)	
C.	Slightly altered joint walls. Non-softening mineral coatings, sandy particles, clay-free disintegrated rock etc.	2.0	(25°—30°)	
D.	Silty-, or sandy-clay coatings, small clay-fraction (non-softening)	3.0	(20°—25°)	

Table 2. Continued

E.	Softening or low friction clay mineral coatings, i. e. kaolinite, mica. Also chlorite, talc, gypsum and graphite etc., and small quantities of swelling clays. (Discontinuous coatings, 1—2 mm or less in thickness)	4.0	(8^0—16^0)
	(b) *Rock wall contact before 10 cms shear*		
F.	Sandy particles, clay-free disintegrated rock etc.	4.0	(25^0—30^0)
G.	Strongly over-consolidated, non-softening clay mineral fillings (Continuous, <5 mm in thickness)	6.0	(16^0—24^0)
H.	Medium or low over-consolidation, softening, clay mineral fillings. (Continuous, <5 mm in thickness)	8.0	(12^0—16^0)
J.	Swelling clay fillings, i. e. montmorillonite (Continuous, <5 mm in thickness). Value of J_a depends on percent of swelling clay-size particles, and access to water etc.	8.0—12.0	(6^0—12^0)
	(c) *No rock wall contact when sheared*		
K, L, M.	Zones or bands of disintegrated or crushed rock and clay (see G, H, J for description of clay condition)	6.0, 8.0 or 8.0—12.0	(6^0—24^0)
N.	Zones or bands of silty- or sandy clay, small clay fraction (non-softening)	5.0	
O, P, R.	Thick, continuous zones or bands of clay (see G, H, J for description of clay condition)	10.0, 13.0 or 13.0—20.0	(6^0—24^0)

5.	JOINT WATER REDUCTION FACTOR	(J_w)	Approx. water pressure (kg/cm²)	
A.	Dry excavations or minor inflow, i. e. <5 l/min. locally	1.0	<1	Note:
B.	Medium inflow or pressure occasional outwash of joint fillings	0.66	1.0— 2.5	(i) Factors C to F are crude estimates. Increase J_w if drainage measures are installed
C.	Large inflow or high pressure in competent rock with unfilled joints	0.5	2.5—10.0	(ii) Special problems caused by ice formation are not considered
D.	Large inflow or high pressure, considerable outwash of joint fillings	0.33	2.5—10.0	
E.	Exceptionally high inflow or water pressure at blasting, decaying with time	0.2—0.1	>10.0	
F.	Exceptionally high inflow or water pressure continuing without noticeable decay	0.1—0.05	>10.0	

Table 3. Descriptions and Ratings for the Parameter *SRF*

6.	STRESS REDUCTION FACTOR			(*SRF*)	
	(a) *Weakness zones intersecting excavation, which may cause loosening of rock mass when tunnel is excavated*				Note: (i) Reduce these values of *SRF* by 25—50% if the relevant shear zones only influence but do not intersect the excavation
A.	Multiple occurrences of weakness zones containing clay or chemically disintegrated rock, very loose surrounding rock (any depth)			10.0	
B.	Single weakness zones containing clay, or chemically disintegrated rock (depth of excavation $\leqq 50$ m)			5.0	
C.	Single weakness zones containing clay, or chemically disintegrated rock (depth of excavation > 50 m)			2.5	
D.	Multiple shear zones in competent rock (clay free), loose surrounding rock (any depth)			7.5	
E.	Single shear zones in competent rock (clay free) (depth of excavation $\leqq 50$ m)			5.0	
F.	Single shear zones in competent rock (clay free) (depth of excavation > 50 m)			2.5	
G.	Loose open joints, heavily jointed or "sugar cube" etc. (any depth)			5.0	
	(b) *Competent rock, rock stress problems*	σ_c/σ_1	σ_t/σ_1		
H.	Low stress, near surface	> 200	> 13	2.5	(ii) For strongly anisotropic stress field (if measured): when $5 \leqq \sigma_1/\sigma_3 \leqq 10$, reduce σ_c and σ_t to $0.8\,\sigma_c$ and $0.8\,\sigma_t$; when $\sigma_1/\sigma_3 > 10$, reduce σ_c and σ_t to $0.6\,\sigma_c$ and $0.6\,\sigma_t$ where: σ_c = unconfined compression strength, σ_t = tensile strength (point load), σ_1 and σ_3 = major and minor principal stresses
J.	Medium stress	200—10	13—0.66	1.0	
K.	High stress, very tight structure (Usually favourable to stability, may be unfavourable to wall stability)	10—5	0.66—0.33	0.5—2.0	
L.	Mild rock burst (massive rock)	5—2.5	0.33—0.16	5—10	
M.	Heavy rock burst (massive rock)	< 2.5	< 0.16	10—20	
	(c) *Squeezing rock;* plastic flow of *incompetent rock under the influence of high rock pressures*				(iii) Few case records available where depth of crown below surface is less than span width. Suggest *SRF* increase from 2.5 to 5 for such cases (see H)
N.	Mild squeezing rock pressure			5—10	
O.	Heavy squeezing rock pressure			10—20	
	(d) *Swelling rock; chemical swelling activity depending on presence of water*				
P.	Mild swelling rock pressure			5—10	
R.	Heavy swelling rock pressure			10—15	

David Viejo Mariño

Rock stability models, slope stability and rockfall assessment for a section of Vestpynten-Bjorndalen (Svalbard)

NTNU
Norwegian University of Science and Technology

UNIS
The University Centre in Svalbard

DTU